

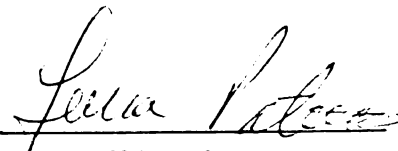


This is to certify that the  
thesis entitled  
Element Mobility and Secondary Mineral Formation  
During the Early Stages of Alteration  
in Rocks from the Tecuamburro Volcanic  
Complex, Southeast Guatemala  
presented by

Jennifer Anne Wade

has been accepted towards fulfillment  
of the requirements for

Master's degree in Geological Sciences

  
Major professor

Date 8/22/02



**LIBRARY**  
**Michigan State**  
**University**

**PLACE IN RETURN BOX** to remove this checkout from your record.  
**TO AVOID FINES** return on or before date due.  
**MAY BE RECALLED** with earlier due date if requested.

DATE DUE	DATE DUE	DATE DUE
	OCT 13 2008	
	<del>OCT 13 2008</del>	

**ELEMENT MOBILITY AND SECONDARY MINERAL FORMATION DURING THE  
EARLY STAGES OF ALTERATION IN ROCKS FROM THE TECUAMBURRO  
VOLCANIC COMPLEX, SOUTHEAST GUATEMALA**

**By**

**Jennifer Anne Wade**

**A THESIS**

**Submitted to  
Michigan State University  
in partial fulfillment of the requirements  
for the degree of**

**MASTER OF SCIENCE**

**Department of Geological Sciences**

**2002**

## **ABSTRACT**

### **ELEMENT MOBILITY AND SECONDARY MINERAL FORMATION DURING THE EARLY STAGES OF ALTERATION IN ROCKS FROM THE TECUAMBURRO VOLCANIC COMPLEX, SOUTHEAST GUATEMALA**

**By**

**Jennifer Anne Wade**

It is widely acknowledged that weathering and hydrothermal alteration can change the composition of volcanic rocks. However, the mobility of REE and other trace elements at the earliest stages of these secondary processes is not well understood. Rocks ranging in composition from basalt to dacite were sampled from three geologic units, ranging in age from 0.8 to 2.6 Ma, of the Tecuamburro volcanic complex. Most major elements, particularly Ca, consistently decrease in volumetric concentration from core to rind. Of the trace elements analyzed, only Th is immobile in all samples. Niobium is often depleted in the rind relative to the core, as is Sr. Cerium is generally immobile, while the other REE, Y, and Ba are sometimes enriched in cores and rinds, relative to fresh lavas from the region. This bulk rock REE-enrichment correlates well with the presence of secondary REE-phosphates. Literature suggests that a low pH is necessary for the mobility of the REE, and a high pH, produced by the weathering of primary minerals, provides the conditions for precipitation of the REE-phosphate. Other secondary products observed include clays, barite, hollandite, and gibbsite. This study has identified elements that are mobilized during incipient weathering, and the element enrichment and depletion trends presented should help igneous petrologists identify altered samples before they are used in petrogenetic studies.

**For Helen and Alan Wade**

**We are on slow trains across  
wide states  
All tunnels/no sights  
and water lapping on rocks during  
long geological nights**

**The big show has gone en fuego  
We've dropped  
regrets and residues  
pretenses and pastenses  
All we need to know we see under microscopes  
Proud parents of isolated isotopes.**

**D.O. Scully, 2002**

## ACKNOWLEDGEMENTS

I have had more fun working on this project than I could have ever imagined, even through the most endless of hard days. The amazing scientists (and friends) that have surrounded me in the last two years are completely responsible for making this thesis into what it is. My most enormous and heartfelt thanks go first to Lina Patino. She has been the most fantastic advisor I could have ever asked for in too many ways to list here. From her I have learned what it means to do science, and that perspective is the key to learning anything. I also thank, with all of my heart, Tom Vogel, for putting up with me, making it easy to put up with him, and for teaching me how to teach. Many thanks to Michael Velbel for luring me whole-heartedly into the world of weathered rocks, and teaching me that nothing is as simple as it looks. Thanks to Barry Cameron for his invaluable previous work, and contagious enthusiasm for everything. Thanks to Ewa Danielewicz for sharing her brilliance on the SEM, and for giving me even more reasons to love Poland. Thanks to Jason Price for his XRD expertise and patience, and to Gary Weissmann for his printer and refreshing open mind. Gigantic thanks to David Szymanski for making me laugh so hard I can't breathe and for knowing me too well, and to Brittany Graham for adventures and conversation that will be hard to match. Many thanks to Susie Biteman for keeping me sane in the nerdiry and making it much too hard to leave Michigan, and thanks to Erin Rasmusson for moving at the same time so it's not even harder, and for making me actually enjoy paleontology. Thanks to Steve Kaczmarek for enjoying the position of devil's advocate, to Nick Waterson for being the most genuine person I know, and to Joel Fett for making me mad and making me laugh all at once. Thanks to Adam Pitt for putting things in perspective and smiling when I cannot, and to Karen Tefend, Ela Viray, and the other grad students and faculty who make this department a great place to work in every day. Thanks to Acme Jam for reminding me every Tuesday that there is more to life than geology. A thousand thanks to Scott Cummings for advising me through seven years of chaos, to Matthew Wright for having more faith in me than I deserve, and to Daniel Scully for letting me teach him time and time again the difference between rocks and minerals, and for believing in everything that I do no matter how strange or stressful. Thanks to the HunneHaffs for unending encouragement and eccentricity, and most emphatically I thank my fantastic mom, without whom I would never have come this far.



## TABLE OF CONTENTS

LIST OF TABLES.....	vi
LIST OF FIGURES.....	vii
INTRODUCTION.....	1
Background.....	3
Geologic Setting.....	5
Methods	
Geochemistry.....	6
Bulk density.....	7
Scanning electron microscopy.....	8
X-ray diffraction.....	8
RESULTS	
Sample Descriptions	
Hand samples.....	19
Petrography.....	19
Whole-rock Chemical Analyses.....	45
Major elements.....	46
Trace elements.....	48
X-ray Diffraction.....	65
Scanning Electron Microscopy.....	80
DISCUSSION	
Primary mineral alteration.....	139
Clays and other secondary minerals.....	141
Development of the REE-P phase.....	142
Relative element mobility.....	144
Possible solution conditions.....	149
CONCLUSIONS.....	150
APPENDICIES	
Appendix A – Sample locations.....	160
Appendix B – XRD sample preparation techniques.....	162
Appendix C – Bulk rock chemical analyses.....	165
Appendix D – Primary and secondary mineralogies.....	176
Appendix E – Instrumental precision.....	180
Appendix F – Evaluation of instrumental precision.....	182
REFERENCES.....	188

## LIST OF TABLES

Table	page
<b>1. Rind thickness measurements for Tecuamburro hand samples.</b>	<b>26</b>
<b>2. Percent change from core to rind of volumetric concentrations of the elements analyzed (<math>C_{\text{rind}} - C_{\text{core}} / C_{\text{core}}</math>). Major element values that changed 5%-10% are shaded lightly, and &gt;10% shaded darkly. Trace elements that changed 20% or more are shaded darkly. A negative % indicates loss in the rind.</b>	<b>52</b>
<b>Appendix A. Sample locations and types.</b>	<b>161</b>
<b>Appendix C. Concentrations of major element oxides (wt%) and trace elements (ppm), as well as bulk density values (g/cm<sup>3</sup>) for each sample. Major element, Zr, Rb, and Sr analyses obtained by XRF, and all other trace elements by La-ICP-MS.</b>	<b>166</b>
<b>Appendix D. Primary and secondary mineralogy of Tecuamburro samples, as observed using optical microscopy, scanning electron microscopy, and x-ray diffraction. X = present, / = inferred.</b>	<b>177</b>
<b>Appendix E. Instrumental precision. JB-1a was treated as an unknown for XRF and ICP-MS analyses. (5 different samples were prepared as glass disks).</b>	<b>181</b>
<b>Appendix F. Evaluation of instrumental precision. For each sample, the left column is the absolute value of the concentration of the core minus the rind. The right column is the percent standard error (see Appendix E) of the analysis of the core sample.</b>	<b>183</b>

## LIST OF FIGURES

Figure	page
1. Representative REE patterns for 1995 Tecuamburro samples. Even though the lavas did not show evidence of weathering in hand sample or thin section, the REE patterns indicate that some Tecuamburro samples were exposed to different amounts of alteration. Triangles = Qtapg, squares = Qtap, and circles = Qas.	10
2. Sr isotopes versus Ce anomaly of some Tecuamburro lavas sampled in 1995. $Ce^* = \log^{-1}(Ce_N)$ where $\log Ce_N = a \cdot 58 + b$ , and $a = (\log La_N - \log Nd_N)/57 - 60$ , and $b = \log Nd_N - (a \cdot 60)$ . N indicates chondrite-normalized concentrations. Normalization factors are from Sun and McDonough (1989)). Triangles = Qtapg, squares = Qtap, and circle = Qas. If the Ce anomalies in these magmas were produced by contributions from oceanic sediments, there would be more variation in the Sr isotope values.	11
3. Weathering Index versus SiO <sub>2</sub> for Tecuamburro lavas sampled in 1995. The Weathering index (Parker, 1970) is based on the molecular proportions of MgO, CaO, Na <sub>2</sub> O, and K <sub>2</sub> O. □ = Qtap, ● = Qas, and ▲ = Qtapg. The shaded region indicates the Weathering Index values for recent lavas from Central America. Since most of the 1995 samples fall within that shaded region, based on major element chemistry, it appears that most of the samples are fresh.	12
4. Photo-micrograph of an incipiently altered andesite sampled from unit Qas in 1995. Plagioclase is the dominant phenocryst, and most are unweathered. Some slight alteration is present near glassy melt textures, and around grain boundaries.	13
5. Map of the Central American arc, produced by the subduction of the Cocos plate beneath the Caribbean plate. Red dots indicate the volcanic front, while green dots represent back arc volcanism. Tecuamburro volcano, located in southeast Guatemala, is indicated by the square.	14
6. Geologic map of the Tecuamburro volcanic complex (from Cameron, 1998). Samples were taken from units Qas, Qtap, and Qtapg.	15
7. Example hand sample from Tecuamburro, unit Qtapg. Each hand sample was divided up into a core, rind, and sometimes intermediate section for all analyses.	16

8. Backscattered-electron image of the boxwork structure remaining after the weathering of a plagioclase phenocryst. The boxwork structure itself, as well as the surrounding voids and grains display no evidence of compaction, so it is safe to assume that the weathering of these rocks has been isovolumetric. 17
  
9. Plots of  $\text{Al}_2\text{O}_3$  versus bulk density of Tecuamburro lavas. In diagram a, which plots  $\text{Al}_2\text{O}_3$  in weight percent, it appears that  $\text{Al}_2\text{O}_3$  content does not change from core to rind within sample sets. However, in diagram b, which plots the volumetric concentration of  $\text{Al}_2\text{O}_3$ , it is obvious that the concentration decreases from core to rind.  $\square = \text{Qtap}$ ,  $\bullet = \text{Qas}$ ,  $\blacktriangle = \text{Qtapg}$ . Filled symbols represent cores, open symbols represent rinds. 18
  
10. Hand sample photograph of Qtapg 002. Note the thick, white rind that is very different from the thinner, orange rind sometimes observed (e.g. figure 7). 27
  
11. Hand sample photograph of Qas 002. Beneath the external, yellow-orange rind, there is a faint red sub-rind or weathering front. Note that the matrix and phenocrysts between the external rind and the sub-rind appears fairly unaltered. 28
  
12. Hand sample photographs of Qtap 004. In the top photo, two pieces were broken apart to reveal the internal weathering front. In the hole from piece 'b' was an 'egg-shaped' concentration of clay material. The bottom photo is a closer look at the weathering front. Note the reddish matrix stain that lines the circumference of the front. 29
  
13. Hand sample photograph of Qtapg 004. This sample has two different rinds - one red, and one white, as indicated above. 30
  
14. Qtap 003 core. Larger plagioclase phenocrysts are less altered than the smaller one, which has preferentially weathered in the center, while the rim has remained fresh. The pyroxene phenocryst is starting to weather only at a fracture, near a plagioclase grain boundary. 31
  
15. Qtap 003 1 rind. A group of extensively altered plagioclase grains. Note that some surrounding plagioclase grains are less altered. 31
  
16. Qtap 003 rind. Plagioclase phenocrysts that have some sections that preferentially weathered along zones, or where glass inclusions once were. Note the tan alteration product (presumably clay) within the altered sections. 32

17. Qtap 003 rind. Highly altered pyroxene adjacent to denticularly altered plagioclase. Not the surrounding, variably weathered plagioclase phenocrysts, and nearly unweathered pyroxene (lower left).	32
18. Qtap 004 rind. Plagioclase phenocrysts with two different alteration products. The darker, red-brown 'rusty' product is associated with the cross-cutting fracture. The lighter, yellow product is either a separate product, developing along a different pathway, or it is an earlier stage of the dark product.	33
19. Qtap 004 e. The boundary between the weathering front and the rest of the rock. Note the drastically different degrees of plagioclase and pyroxene alteration.	33
20. Qtap 004 e. Within the weathering front. Note that while most of the smaller grains have been completely altered, the large plagioclase remains surprisingly clean.	34
21. Qtap 002a core. Fresh olivine surrounded by a matrix of plagioclase and pyroxene microlites.	34
22. Qtap 002b rind. Pyroxene phenocryst, near a vesicle edge, that is starting to alter along grain boundaries.	35
23. Qas 003 1 core. A slightly altered plagioclase. The pyroxenes are relatively clean, with some plagioclase and opaque inclusions. The top pyroxene is stained by alteration of an iron oxide in the matrix.	35
24. Qas 003 1 int. Most of the large plagioclase grain (lower left) has been altered, while the rim remains clean. Most plagioclase microlites are clean. Note the small, uncharacterized alteromorphs ('altmph') present in the matrix as well.	36
25. Qas 003 1 int. Plagioclase phenocryst with a clean core, very altered zone, and clean rim.	36
26. Qas 005c rind. Plagioclase phenocryst with yellow and orange staining along fractures. Small alteromorphs are to the left of the grain, adjacent to smaller plagioclases.	37
27. Qas 002 rind. Plagioclase phenocryst with glass inclusions that appear <i>not</i> to induce preferential weathering of the grain.	37
28. Qas 003 1 rind. Pyroxene phenocryst with dark red-brown staining in cleavages, and along grain boundaries. A small phenocryst in the lower left has been plucked out, leaving a small void.	38







<b>29. Qas 002 rind. Clean plagioclase phenocryst next to a highly altered pyroxene associated with opaques.</b>	<b>38</b>
<b>30. Qas 005a core. Pyroxene phenocryst near hornblende phenocryst that has been partially replaced by Fe-oxides and possibly clay.</b>	<b>39</b>
<b>31. Qtapg 002 core. Altered pyroxene and hornblende with secondary product-filled fractures. Note that the dark product in the hornblende is associated with an opaque, while the product in the pyroxene is much lighter.</b>	<b>40</b>
<b>32. Qtapg 002 core. Plagioclase phenocryst with dark red alteration, surrounded by smaller, cleaner plagioclase microlites. Note the staining of the glass in the lower left corner.</b>	<b>40</b>
<b>33. Qtapg 005 rck. Crevice that has partially filled with clay and is lined with a secondary hollandite (see SEM results, figure 68) surrounded by hornblende and plagioclase phenocrysts.</b>	<b>41</b>
<b>34. Qtapg 004 core. Clean plagioclase adjacent to a void, from which a grain was plucked.</b>	<b>41</b>
<b>35. Qtapg 004 white rind. Clay pseudomorph of a plagioclase, next to a clean, smaller plagioclase grain. Note that the rim of the larger grain remains intact, and that half of the grain has been plucked out.</b>	<b>42</b>
<b>36. Qtapg 004 white rind. Alteromorph that represents what, if anything, is left of the phenocrysts in the white rind. This alteromorph is most likely replacing a clinopyroxene.</b>	<b>43</b>
<b>37. Qtapg 004 red rind. Red and brown staining of the matrix and tan alteration along plagioclase grain boundaries.</b>	<b>44</b>
<b>38. Qtapg 004 red rind. Red and yellow staining around plucked plagioclase grains, adjacent to clean plagioclase grains.</b>	<b>44</b>
<b>39. Classification of Tecuamburro core samples. Circles represent Qas, the youngest unit, triangles represent Qtapg, the middle unit, and squares represent the oldest unit, Qtap. Asterisks represent samples from recent lavas, for comparison.</b>	<b>51</b>
<b>40. Major element volumetric concentration plots for Tecuamburro samples. ■ = Qtap, ▲ = Qtapg, and ● = Qas. Filled symbols represent cores, open symbols represent rinds. ✕, ◇, and ◇ represent intermediate and/or unique samples from Qtap, Qtapg, and Qas, respectively.</b>	<b>55</b>

<b>41. Trace element volumetric concentration plots for Tecuamburro samples. ■ = Qtap, ▲ = Qtapg, and ● = Qas. Filled symbols represent cores, open symbols represent rinds. ⌘, ◇, and ◇ represent intermediate and/or unique samples from Qtap, Qtapg, and Qas, respectively.</b>	<b>57</b>
<b>42. REE plots of samples from Qtap, in volumetric concentrations. ■ = core, □ = rind, and ⌘ = the subsurface weathering rind, or ‘egg.’</b>	<b>59</b>
<b>43. REE plot of samples from Qtapg, in volumetric concentrations. ▲ = core, ◇ = intermediate, and △ = rind.</b>	<b>61</b>
<b>44. REE plot of samples from Qas, in volumetric concentrations. ● = core, ◇ = intermediate, ○ = rind.</b>	<b>63</b>
<b>45. Classification diagram for the eight samples analyzed by XRD. Squares represent samples from unit Qtap, the circle is from unit Qas, and the triangles are from unit Qtapg. The filled symbol represents a core, and open symbols represent rinds or exfoliated corestone shells.</b>	<b>68</b>
<b>46. XRD pattern for the core of Qtapg 004. Smectite (S) is present in the Mg- and Mg-gly-scans, while feldspar (F) peaks are present in all scans. Number labels indicate d-spacing.</b>	<b>69</b>
<b>47. XRD pattern for the red rind of Qtapg 004. Smectite (S) is present in the Mg- and Mg-gly scans, while feldspar peaks (F) are present in all scans. Number labels indicate d-spacing.</b>	<b>70</b>
<b>48. XRD pattern for the white rind of Qtapg 004. Smectite (S) is present in the Mg- and Mg-gly-scans. Kaolinite (K), feldspar (F), and possibly barite (B) peaks are present in the Raw scan. In both of the K-treated samples, the broad peak is most likely a consequence of KCl-saturation. Number labels indicate d-spacing.</b>	<b>71</b>
<b>49. XRD pattern for the rind of Qtapg 002. Kaolinite (K) is present in all but the heated scan, while feldspar (F) (possibly including potassium feldspar (KF)) is present in all scans. The peak labeled ‘K’ is most likely a saturation effect from the K-saturating solution. Number labels indicate d-spacing.</b>	<b>72</b>
<b>50. XRD pattern for the rind of Qas 004. Kaolinite (K) is present, as well as feldspar (F). The peak labeled ‘Mg’ is most likely an effect of the Mg-saturating solution. Number labels indicate d-spacing.</b>	<b>73</b>
<b>51. XRD pattern for the rind of Qtap 004a. Gibbsite (G) is present in all but the heated scan, while feldspar (F) is present in all scans. Number labels indicate d-spacing.</b>	<b>74</b>

<b>52. Field photograph of the in-situ corestone 0512008, from map unit Qtap. The rind of the corestone, as well as the spheroidally exfoliated layers ('shells') surrounding the corestone were analyzed. XRD scans and SEM images follow in figures 53-56.</b>	<b>75</b>
<b>53. XRD pattern for the rind of 0512008. Kaolinite (K) is present in the raw and K-saturated samples, while feldspar (F) is present in all samples. Number labels indicate d-spacing.</b>	<b>76</b>
<b>54. XRD pattern for the rind of 0512008. Kaolinite (K) and/or halloysite (H) are present in all but the K-heated sample, while feldspar (F) is present in all samples. Number labels indicate d-spacing.</b>	<b>77</b>
<b>55. Secondary-electron image of a fracture on the surface of a plagioclase phenocryst from 0512008 core (a) contains aggregates (b) of Halloysite rods (c).</b>	<b>78</b>
<b>56. Secondary-electron image of an etch pit on the surface of a plagioclase phenocryst from the rind of corestone 0512008. Note the round halloysite balls that are in and around the pit (e.g. Robertson and Eggleton, 1991).</b>	<b>79</b>
<b>57. Denticularly altered pyroxene. Point 1 is the phenocryst, point 2 is clay filling the fracture, and point 3 is a potassium feldspar microlite. BSI from thin section Qas 004 r.</b>	<b>84</b>
<b>58. Point 1 is an apatite inclusion within a pyroxene (point 2), which also contains plagioclase inclusions (point 3). BSI from thin section Qas 003 c.</b>	<b>87</b>
<b>59. A Sr-bearing barite (point 1), associated with plagioclase (point 2). Some white (and therefore high average atomic number) minerals are Fe-Ti oxides, not sulfates (point 3). BSI from thin section Qas 003 r.</b>	<b>90</b>
<b>60. Barite (point 1) that has traveled along a fracture into a clay-filled plagioclase grain (points 2 and 3). BSI from thin section Qtapg 0011 int.</b>	<b>93</b>
<b>61. Barite (point 1) and a Ba-Nd-P-phase (point 2) associated with clay (point 3) and plagioclase (point 4). BSI from thin section Qtapg 0011 r.</b>	<b>96</b>
<b>62. A crevice lined with hollandite (points 1 and 2) as well as clay, surrounding a plagioclase grain (points 3 and 4). BSI from thin section Qtapg 0011 int.</b>	<b>100</b>
<b>63. A secondary Ba,Mn,Fe,P-phase (point 1) and a Ba,Mn,Fe,LREE,P-phase (point 2) line the surface of a crevice filled by clay material (see spectra for points 3 and 4). BSI from thin section Qtapg 005 rck.</b>	<b>104</b>

<b>64. An REE-phosphate (point 1) associated with clay (point 2) that has nearly completely replaced a plagioclase grain (point 3). BSI from thin section Qtap 003 r.</b>	<b>108</b>
<b>65. An LREE-P phase (point 1) among clay (point 2) within a fracture in a clinopyroxene (point 3). BSI from thin section Qtapg 001 r.</b>	<b>111</b>
<b>66. A Y,REE-phosphate (point 1) associated with plagioclase (point 2). BSI from thin section Qtapg 0012 c.</b>	<b>114</b>
<b>67. Two REE-P phases (points 1 and 2). They are associated with clay that appears to have developed within a plagioclase grain (see points 3 and 4). BSI from thin section Qtapg 002 r.</b>	<b>116</b>
<b>68. A secondary REE-P phase (point 1) within clay material (point 2) associated with postassium feldspar (point 3). BSI from thin section Qas 004 r.</b>	<b>120</b>
<b>69. A group of LREE-P phases (point 1) within a mineral that have been completely replaced by clay (point 2). BSI from thin section Qtapg 004 c.</b>	<b>123</b>
<b>70. A secondary LREE-P phase (point 1), filling void spaces within a potassium feldspar (point 2). BSI from thin section Qtapg 004 rr.</b>	<b>125</b>
<b>71. A secondary P-phase devoid of REE (point 1) along the grain boundary of a phenocryst replaced by clay (point 2). BSI from thin section Qtapg 004 rw.</b>	<b>127</b>
<b>72. A Y,REE-P phase (point 1) within a clay-filled zone (point 2) of a plagioclase grain (point 3). BSI from thin section Qtap 003 c.</b>	<b>129</b>
<b>73. REE-P phase (point 1) associated with clay (point 2), along zones of a plagioclase grain (point 3). BSI from thin section 0512008 crr.</b>	<b>132</b>
<b>74. En-echelon REE-P phases (point 1) and a Y,REE-phosphate (point 2) in a plagioclase grain (point 3). BSI from thin section 0512008 crc.</b>	<b>135</b>
<b>75. Secondary-electron image of an REE-phosphate on the surface of a clay-lined crevice in a plagioclase phenocryst from the rind of corestone 0512008. Image b is a magnified section of image a.</b>	<b>138</b>
<b>76. Plots of a) volumetric concentration of <math>P_2O_5</math>, b) normative % apatite, and c) Ce/Ce* anomaly, all versus the presence (or absence) of primary and secondary phosphate phases. Note that there is no correlation between <math>P_2O_5</math> or apatite and the presence of the REE-P-phase, and that any samples with <math>Ce/Ce^* &lt; 0.6</math> contain the secondary REE-P-phases.</b>	<b>153</b>

77. REE plot of the corestone 051200, from unit Qtap.  = core,  = rind and exfoliated shells.  = values for fresh lavas of the volcanic complex. Note the enrichment of the core and rind of the corestone, and relative depletion of the highly weathered, spheroidally exfoliated shells (Patino et al., in review). 154
78. Element mobility plots for Qtapg 001 (core, intermediate, and rind) and Qtapg 004 (core, red rind, and white rind). All samples normalized to the core. Note that unlike previous trace element plots, the scale is linear, not log. 155
79. Element mobility plots for Qtap 005 (core and rind) and Qtap 004 (core, sub-rind weathering front ('egg'), and rind). All samples normalized to the core. Note that unlike previous trace element plots, the scale is linear, not log. 156
80. Element mobility plots for the cores and rinds of Qas 004 and 005. All samples normalized to the core. Note that unlike previous trace element plots, the scale is linear, not log. 157
81. Element mobility model for Tecuamburro. In the zone of low pH (the regolith of exfoliated shells), most elements are mobilized into solution, while the rest are either immobile, or move into less weathered material (e.g. REE<sup>3+</sup>, Y, Ba, and sometimes Rb, Pb, and Mn). In the zone of high pH (the rind and part of the core/fresh material), the REE, Y and Ba precipitate, and Na and Ca are only slowly lost. 158
82. Ternary diagram that plots Ce, Nd, and CaO, in order to discern altered from fresh samples. The shaded field represents fresh Central American arc lavas. Samples that fall outside the shaded field are considered altered. Asterisks represent samples from Central America (other than those used in this study) that were sampled for petrogenetic studies, but were then found to be altered and excluded from the studies. Tecuamburro samples from this study are plotted as squares (Qtap), circles (Qas), and triangles (Qtapg). Filled symbols are cores, open symbols are rinds. Altered Tecuamburro samples in which the secondary REE-P-phases were found plot outside the fresh field (with the exception of Qtapg 001c, the transitional sample indicated as ) , and samples which are less altered fall within. 159



## INTRODUCTION

Rare earth elements (REE) and other trace elements are crucial to petrologic studies of not only volcanic arcs, but all igneous systems. Subduction-related magmas are enriched in large ion lithophile elements (LILE) relative to REE and high field strength elements (HFSE) (Pearce and Peate, 1995). Ratios of these elements are therefore often used to determine arc lava petrogenesis. The trace element compositions of Quaternary Central American lavas have been studied by a number of workers, in order to understand source composition and degrees of melting (e.g. Carr et al., 1990; Feigenson and Carr, 1993; Walker et al., 1995; Patino et al., 2000). These studies assumed that the original composition of the lavas was preserved throughout their post-emplacement exposure history, and the samples were carefully examined for signs of alteration, so that altered samples could be excluded from the studies.

In 1995, Michael J. Carr and Barry I. Cameron collected a number of samples from the Tecuamburro volcanic complex as part of a study of the evolution of southeastern Guatemalan lavas over time (Cameron, 1998). The samples contain little evidence of weathering, both in hand sample and in thin section, and were therefore deemed useful for such a petrologic study. The major element compositions of the Tecuamburro samples resembled those of samples previously studied along the Central American arc. However, trace element compositions were very different. In particular, the REE patterns of the Tecuamburro samples varied; some were enriched in REE relative to others, with negative Ce anomalies (figure 1).

Some REE variation is common in arc lavas (White and Patchett, 1984; Othman et al., 1989). Woodhead (1989) noted that negative Ce anomalies in subduction zone magmas could result from the contribution of Ce-depleted slab material. Hemipelagic muds and carbonate oozes comprise the sediments subducting beneath the Central American volcanic arc, and these sediments display negative Ce anomalies (Patino et al., 2000). If the negative Ce anomalies in the Tecuamburro lavas were produced by contribution from the slab sediments, Sr isotope ratios of the samples would vary. However, there is no variation in Sr isotope composition with varying REE content (figure 2). Othman et al. (1989) suggest that negative Ce anomalies are produced by the fractionation of oxidized Ce during metasomatism. The conditions in a subduction zone favor the oxidation of  $Ce^{3+}$  to  $Ce^{4+}$ . This would make the tetravalent Ce less mobile than the rest of the trivalent REE, but even this process would probably not produce the wide range of Ce anomalies displayed by Tecuamburro lavas. Therefore, another secondary process, such as weathering or hydrothermal alteration, is suspected as the cause of the unusual REE patterns.

## **Background**

Few studies have looked at element mobility during the earliest stages of post-emplacement alteration. However, a number of studies have examined the effects of weathering and alteration on trace elements in highly developed regoliths. Nesbitt (1979) notes that weathering (and possibly hydrothermal alteration) have mobilized and fractionated the REE in spheroidally weathered Australian granodiorite, enriching portions of the rocks in REE. He determined that the REE were leached and transported by acidic solutions, then precipitated as clays or adsorbed onto mineral surfaces. Nesbitt and Markovics (1997), in a later examination of a large-scale granodioritic soil profile, describe a “cycling” of elements to and from different parts of the weathering profile. They note that the REE, actinides, transition metals, and metalloids are concentrated in the zone of intermediate weathering, between soil and parent material. They also note that while the REE move generally together (with some HREE fractionation), a negative Ce anomaly is present. This is attributed to the oxidation to  $\text{Ce}^{4+}$ , causing it to behave like the less mobile elements  $\text{Ti}^{4+}$  and  $\text{Zr}^{4+}$ , rather than the  $\text{REE}^{3+}$ .

Eggleton et al. (1987) studied spheroidally weathered Australian basalts, and found that many trace elements, including the REE, are lost from weathered corestones and concentrated in the outer rinds. Brazilian carbonatites, studied by Walter et al. (1995), also show mobility and fractionation of the REE during weathering. They attribute mobility to the development of secondary minerals, such as gorceixite and poorly crystallized Fe-Mn products, which act as “traps” for the trace elements.

There is evidence that incipient weathering can modify the composition of igneous rocks. Kuschel and Smith (1992) noted that young (Late Cenozoic) volcanic rocks from New Zealand were enriched in REE (except Ce) and Y due to the development of secondary, REE-bearing phases during low temperature hydrothermal alteration. Price et al. (1991) describe REE, Y, and Ba enrichment in Tertiary Australian basalts. They also suggest that these elements are mobilized from the glassy matrix by an acidic solution during weathering, and concentrated in secondary clays or phosphates.

The average temperature in southeastern Guatemala is 23.4°C, and the average precipitation 226.08 mm (Mitchell et al., 2002). The tropical climate facilitates the weathering of basalts, but most samples collected in 1995 do not show clear evidence of weathering or hydrothermal alteration, either in major element chemistry, or in thin section (figures 3 and 4). It is important to develop techniques to recognize the effects of incipient weathering and alteration so that altered samples are not used to characterize the petrogenesis of subduction zone magmas.

## **Geologic Setting**

The Tecuamburro volcanic complex is located in southeastern Guatemala, and is part of the Central American volcanic chain (figure 5). It is one of many volcanic front stratovolcanoes along the Cocos-Caribbean convergent plate boundary. Approximately 800 m tall, the Tecuamburro stratovolcano is situated within a 20 km wide, north-trending graben, which terminates at the Jalpatagua strike-slip fault (Duffield et al., 1992). The volcanic complex consists of several craters, ranging in age, shape, and size (figure 6). For this study, rocks from units Qtap (found in the western part of the graben), Qas (found in the graben, northwest of the modern Tecuamburro volcano), and Qtapg (in the north-central part of the graben) were collected. Sample locations are listed in Appendix A.

Preliminary data from rocks sampled in 1995 showed that the lavas range from basalts to andesite. Rocks from the Qtap unit are presumed to have been erupted from two adjacent central vents, and are  $2.6 \pm 0.3$  Ma, making it one of the oldest units in the area (Duffield et al., 1992). Map unit Qas consists of flows from scoria cones built around two vents, and yield an age of  $0.800 \pm 0.061$  Ma (Duffield et al., 1992). Rocks of Qtapg are the most highly altered, and erupted from a single vent, marked by escarpments (figure 6). This unit shows extensive hydrothermal alteration, possibly enabled by fumaroles in the area (Duffield et al., 1992). Although difficult to date due to its alteration, the unit is thought to be between 0.8 and 1.2 Ma (Duffield et al., 1992).



## **Methods**

Price et al. (1991) noted that often, anomalous geochemical behavior cannot be anticipated from detailed petrographic work alone. Therefore, several analytical techniques were employed to complement petrographic data. The Tecuamburro volcanic complex was sampled by Barry Cameron, Lina Patino, and Michael Velbel in 2000. Samples were chosen from three lava flow units (Q<sub>tap</sub>, Q<sub>tapg</sub>, and Q<sub>as</sub>), and were all in the incipient stages of weathering (i.e. they each contained a thin weathering rind and a relatively fresh core).

### *Geochemistry*

Bulk-rock major element and select trace element compositions were obtained from fused glass disks by X-ray fluorescence (XRF), and other trace element compositions were obtained using laser ablation inductively coupled plasma-mass spectrography (LA-ICP-MS). Core, rind, and some intermediate sections were cut from each Tecuamburro hand sample (figure 7), then ground in a tungsten-carbide mill to yield more than 3.0 g of rock powder. Three grams of powder were mixed with 9.000 g lithium tetraborate as a low-temperature flux, and 0.500 g ammonium nitrate as an oxidizer in a platinum crucible. Samples were then melted in platinum crucibles for > 20 min while stirred with an orbital mixing stage. Samples were heated at 1000°C in an oxidizing flame, then poured into platinum disk molds. Fused disks were analyzed at Michigan State University, using a Rigaku S/MAX X-ray fluorescent spectrograph. Data for major-elements were processed using a fundamental parameter data reduction method

(Criss, 1980) with XRFWIN software (Omni Instruments). For trace elements, a Cetac, LSX-200<sup>+</sup>, laser ablation system was used, coupled to the Micromass Platform ICP Mass Spectrometer at MSU. The laser is a UV laser with a wavelength of 266 nm. Pre-ablation spot size was 250  $\mu\text{m}$ , the scan rate 150 :m/sec. Ablation spot sizes were 200  $\mu\text{m}$ , with a scan rate of 10 :m/sec and defocus 50 :m into the glass. The laser was fired at a frequency of 4 Hz. For LA-ICP-MS results, strontium was used as the internal standard (as determined by XRF on the same glass disks). Prior to calculation, the background signal was subtracted from the standards and samples. The trace element concentrations in the samples are based on a linear regression method using USGS and Japanese rock standards.

### *Bulk Density*

Bulk density measurements were made using the glass microsphere method described by Consolmagno and Britt (1998). Because the samples are in the incipient stages of weathering, and exhibit no evidence of compaction or volume change (figure 8), the alteration that these rocks have undergone is presumed to be isovolumetric (Gardner, 1980). Therefore, element concentrations are reported as volumetric concentrations. The concentration of each element (weight percent or ppm) is multiplied by the bulk density of a given sample, yielding units of  $\text{cg}/\text{cm}^3$  or  $\text{g}/\text{cm}^3$ . This is useful because the volumetric concentration considers changes in mass at constant volume, while raw concentrations do not. For example, if one were to plot the concentration of  $\text{Al}_2\text{O}_3$  in weight percent versus bulk density, it might appear that there is no loss or gain, from core to rind, of  $\text{Al}_2\text{O}_3$  (figure 9a). However, if one plots the volumetric concentration of  $\text{Al}_2\text{O}_3$

versus bulk density, it is obvious that there is a loss, or decrease in concentration, from core to rind, of Al (figure 9b). When the volumetric concentration is plotted against bulk density, a “reaction progress diagram” is created (Gardner, 1980).

### *Scanning Electron Microscopy*

Scanning electron microscopy (SEM) was used to examine textural changes in altered samples, as well as to obtain qualitative energy-dispersive spectra of primary and secondary mineral compositions. Colman (1982) and Kuschel and Smith (1992) used backscattered-electron imaging (BSI) and energy-dispersive spectra (EDS) to identify secondary products in altered volcanic rocks. A number of workers (e.g. Berner et al., 1980; Velbel, 1983, 1989, 1993; Tazaki et al., 1987; Banfield and Eggleton, 1989) have used secondary-electron imaging (SEI) to identify surface weathering textures and secondary products. Polished, carbon-coated thin sections were examined using BSI and EDS, and plagioclase phenocryst separates were examined with SEI at MSU using a JEOL JSM-6400V scanning microscope. Working conditions are described in the Results chapter.

### *X-ray Diffraction*

X-ray diffraction (XRD) is a useful tool for identifying secondary products, particularly clays (e.g. Colman, 1982; Nesbitt and Markovics, 1997; Banfield and Eggleton, 1989). XRD was used to identify the clay minerals present in selected samples. Details regarding analytical methods will be discussed later, and sample preparation techniques are found in Appendix B.

While many workers have focused on large, outcrop- or boulder-scale weathering trends, few have examined changes in chemistry and mineralogy at the scale of centimeters or microns, with resolution between core and rind sections. The use of these combined methods on separated portions of samples has produced a detailed, comprehensive study of the effects of weathering, at very small scale, on trace element mobility in the early stages of alteration.

*Formatting note*

The images in this thesis are presented in color.

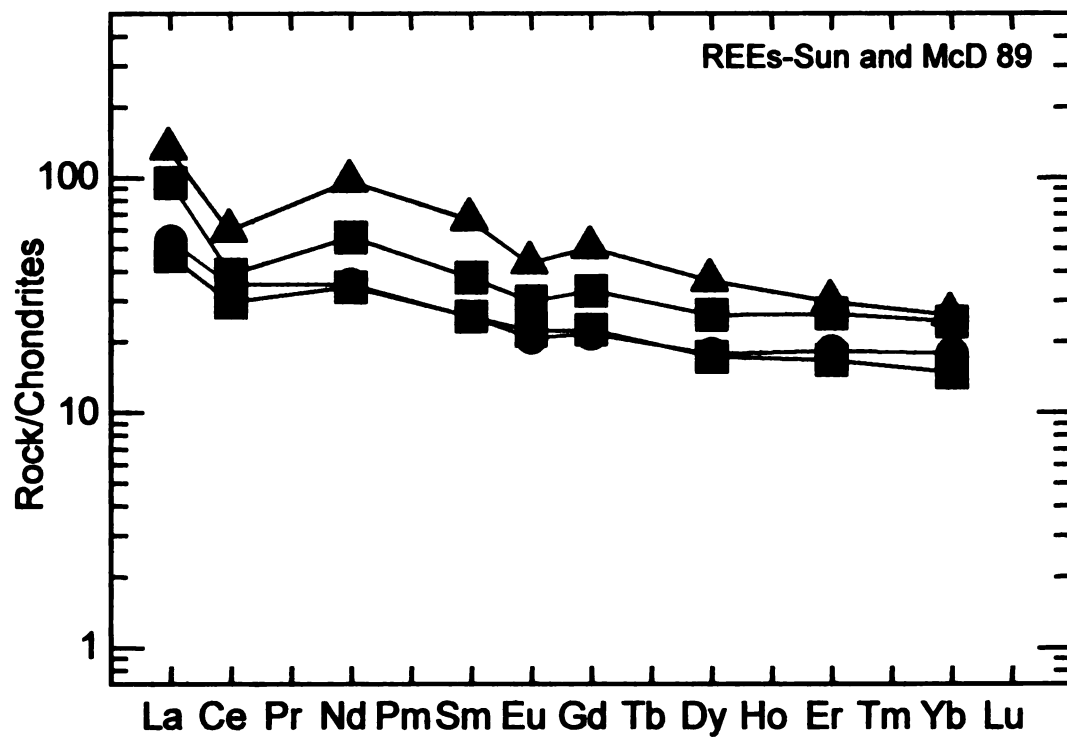


**Figure 1.** Representative REE patterns for 1995 Tecuamburro samples. Even though the lavas did not show evidence of weathering in hand sample or thin section, the REE patterns indicate that some Tecuamburro samples were exposed to different amounts of alteration. Triangles = Qtapg, squares = Qtap, and circles = Qas.

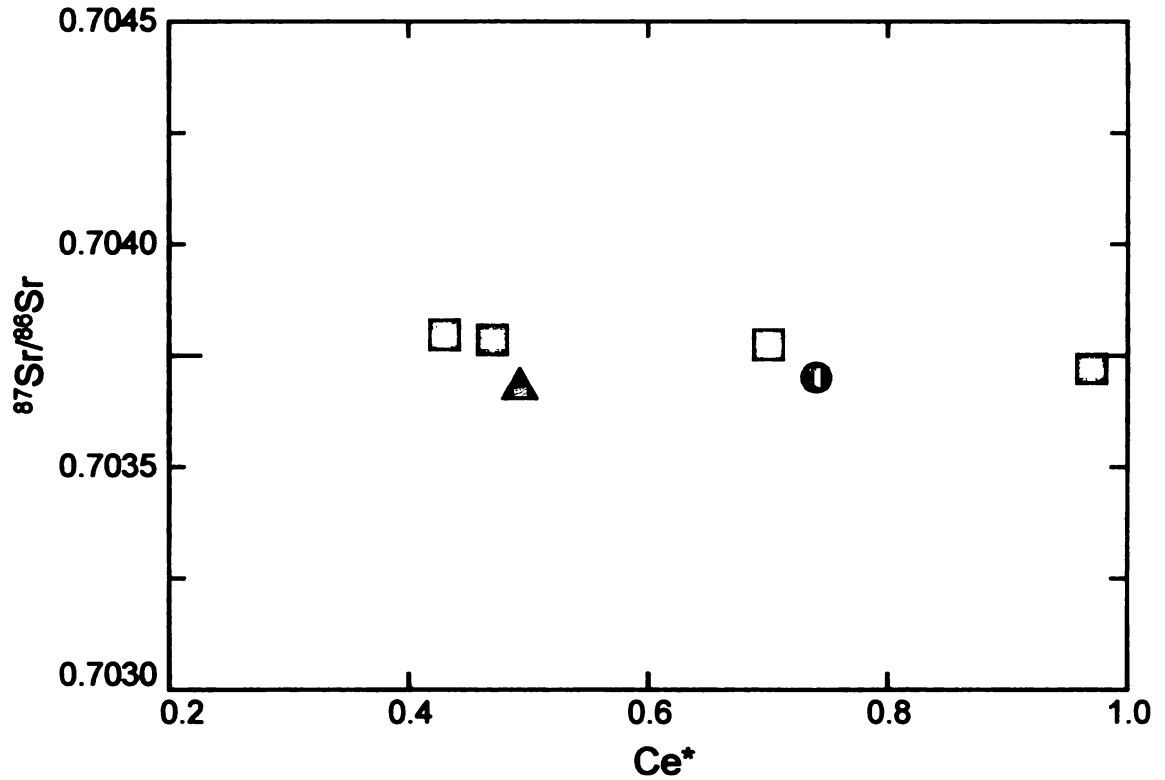


**Figure 2.** Sr isotopes versus Ce anomaly of some Tecuamburro lavas sampled in 1995.  $Ce^* = \log^{-1}(Ce_N)$  where  $\log Ce_N = a \cdot 58 + b$ , and  $a = (\log La_N - \log Nd_N)/57-60$ , and  $b = \log Nd_N - (a \cdot 60)$ . N indicates chondrite-normalized concentrations. Normalization factors are from Sun and McDonough (1989)). Triangles = Qtapg, squares = Qtap, and circle = Qas. If the Ce anomalies in these magmas were produced by contributions from oceanic sediments, there would be more variation in the Sr isotope values.

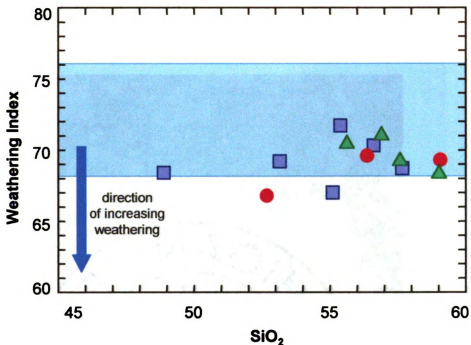


**Figure 3.** Weathering Index versus SiO<sub>2</sub> for Tecuamburro lavas sampled in 1995. The Weathering index (Parker, 1970) is based on the molecular proportions of MgO, CaO, Na<sub>2</sub>O, and K<sub>2</sub>O. ■ = Qtap, ● = Qas, and ▲ = Qtapg. The shaded region indicates the Weathering Index values for recent lavas from Central America. Since most of the 1995 samples fall within that shaded region, based on major element chemistry, it appears that most of the samples are fresh.

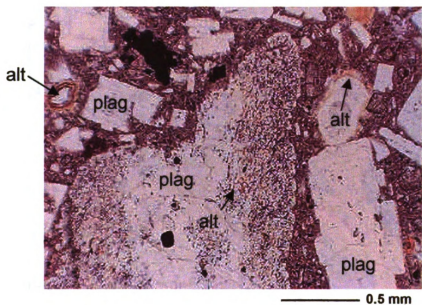


**Figure 4.** Photo-micrograph of an incipiently altered andesite sampled from unit Qas in 1995. Plagioclase is the dominant phenocryst, and most are unweathered. Some slight alteration is present near glassy melt textures, and around grain boundaries.



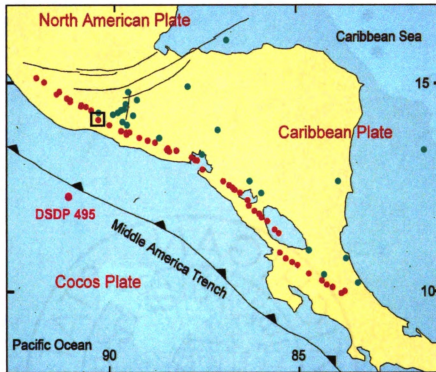


**Figure 5.** Map of the Central American arc, produced by the subduction of the Cocos plate beneath the Caribbean plate. Red dots indicate the volcanic front, while green dots represent back arc volcanism. Tecuamburro volcano, located in southeast Guatemala, is indicated by the square.

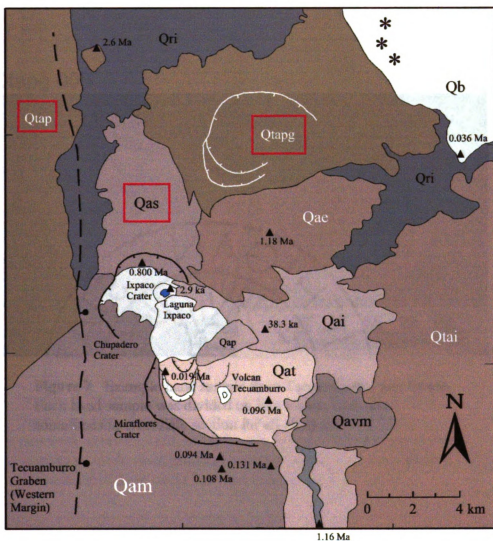


**Figure 6.** Geologic map of the Tecuamburro volcanic complex (from Cameron, 1998). Samples were taken from units Qas, Qatp, and Qap.

Qtapg 003

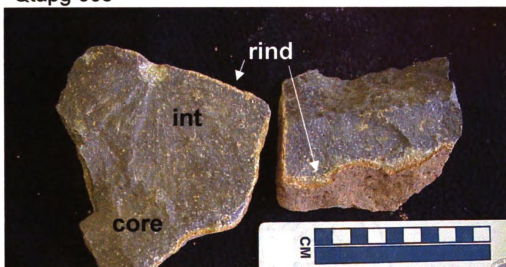


**Figure 7.** Example hand sample from Tecuamburro, unit Qtapg. Each hand sample was divided up into a core, rind, and sometimes intermediate section for all analyses.

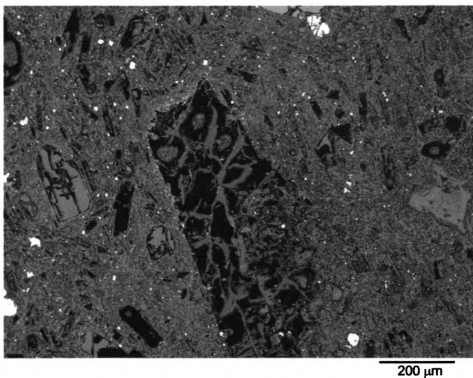


**Figure 8.** Backscattered-electron image of the boxwork structure remaining after the weathering of a plagioclase phenocryst. The boxwork structure itself, as well as the surrounding voids and grains display no evidence of compaction, so it is safe to assume that the weathering of these rocks has been isovolumetric.

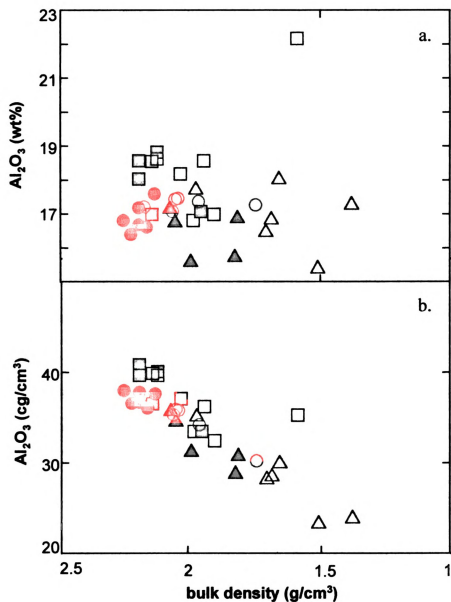


**Figure 9.** Plots of Al<sub>2</sub>O<sub>3</sub> versus bulk density of Tecuamburro lavas. In diagram a, which plots Al<sub>2</sub>O<sub>3</sub> in weight percent, it appears that Al<sub>2</sub>O<sub>3</sub> content does not change from core to rind within sample sets. However, in diagram b, which plots the volumetric concentration of Al<sub>2</sub>O<sub>3</sub>, it is obvious that the concentration decreases from core to rind. □ = Qtap, ● = Qas, ▲ = Qtapg. Filled symbols represent cores, open symbols represent rinds.

## **RESULTS**

### **Sample Descriptions**

#### *Hand Samples*

Hand samples are all fine grained, and dominated by plagioclase phenocrysts no larger than 2 mm in length. Weathering rind thicknesses range in size from 0.5 mm to 3 cm (table 1). Rinds are generally orange-brown or white in color (figures 7 and 10). However, some samples additionally have a thin, red sub-rind weathering front (figure 11). One sample, Qtap 004, contains a small, oval-shaped, internal weathering front unrelated to the surficial weathering rind (figure 12). Another unique sample is Qtapg 004. The hand sample has two separate rinds: one reddish-brown rind, and another, adjacent to the red rind, that is white and chalky (figure 13). This feature is probably due to different leaching conditions affecting the rock from different directions. The conditions were surely dependent on the orientation of the sample, and caused different parts of the sample, on a small scale, to weather differently (or at different rates).

#### *Petrography*

Qtap samples are the most fine-grained of the Tecuamburro samples. They are somewhat glassy (where sparse unweathered glass remains), and very fine grained. Qas samples are also very fine grained, but in general are less glassy. Qtapg samples have, in general, the least glass and coarser matrices. In the few samples where olivine is recognized, it exhibits the earliest stages of alteration. Plagioclase is the most commonly

weathered phenocryst in each of the three units. Several varied patterns of alteration and types of alteration products are observed in the plagioclase grains, and it could be inferred that these variations in alteration style are due to compositional differences between (and within) the grains. This is supported by EDS and microprobe data to be discussed in a later chapter, which shows varying Na/Ca ratios between and within grains.

Vesicularity does not appear to influence the amount of alteration during the earliest stages of weathering. Two Q<sub>tap</sub> samples (002a and 002b) are from the same outcrop, but while one is highly vesicular, the other is almost non-vesicular. These samples happen to also be the most mafic of the suite, and expected to be the most unstable. Only olivine phenocrysts close to vesicle edges in the rind of the vesicular sample are slightly more altered than those in the non-vesicular sample. In the rinds of all units, some phenocrysts have been plucked from the matrix, leaving a void in the shape of the grain. Many phenocrysts, especially in the rinds, have been completely weathered into alteromorphs (terminology of Delvigne, 1998), and further investigation of the composition and nature of these secondary products will be discussed in the section dealing with SEM analyses.

### *Q<sub>tap</sub>*

In general, Q<sub>tap</sub> samples are characterized by finer-grained matrices than Q<sub>as</sub> and Q<sub>tapg</sub>, with some exceptions. Little fresh glass remains in the samples. Plagioclase and pyroxene microlites are common, and usually unaltered, even in the rinds. Plagioclase phenocrysts are abundant, euhedral, and well-zoned, and range in size from 0.25 to 3 mm

in length. Euhedral clinopyroxene and some orthopyroxene phenocrysts are also present, ranging in size from 0.15 to 2 mm in length, but most grains range from 0.15 to 0.5 mm. Opaque minerals are abundant in the matrix, and phenocrysts are euhedral, and often associated with pyroxene.

Fresh matrix glass is rare, and there is dark tan staining of the glass and most plagioclase microlites. Alteration in these (as well as Qas and Qtapg) samples is concentrated in the matrix, and in plagioclase phenocrysts, and the style is varied. Some plagioclase centers are very weathered or corroded, while less commonly, some plagioclase centers are pristine, with altered edges (figures 14 and 15). In other plagioclase grains, alteration concentrates along zone boundaries, or in areas where glass inclusions were once present (figure 16). In many rinds, where alteration was most extensive, rectangular holes remain where once, presumably, plagioclase phenocrysts were. It is interpreted from this texture that the grain had been weathered to the extent that it was 'plucked' out of the matrix, either during the natural course of weathering, or during the thin-section preparation process.

Alteration products are also varied. Tan, amorphous staining is commonly associated with plagioclase, as in figure 16. Reddish brown 'rusty' colors are often observed in fractures or cleavages that cut through both plagioclase and pyroxene phenocrysts (figures 17 and 18). In more fully weathered grains, as in figure 17, the rusty product can dominate parts of grains, apparently having progressed inward from cleavages or fractures (an alteration geometry termed "centripetal replacement by Delvigne, 1998).



Two noteworthy samples which deserve a closer look are Qtap 004, and Qtap 002. In Qtap 004, a small, sub-surface weathering front exists (figure 12), measuring approximately 32 mm in length, penetrating 6 to 2 mm into the surface. This weathering front is isolated from the rest of the rock, with a sharp boundary between the end of the weathering front and the rest of the sample (figure 19). Red alteration products dominate, and the matrix is stained tan and red. Pyroxene is generally less altered than plagioclase. Despite the obviously extreme alteration this area has undergone, some plagioclase grains within the front remain perfectly unaltered (figure 20). Phenocryst size does not appear to be a factor – both large and small grains vary in the extent they are weathered.

The second set of petrographically distinct samples from the Qtap unit are 002a and 002b. These two samples are the most mafic of the entire Tecuamburro suite. They were collected from the same lava flow, but 002a is practically non-vesicular, while 002b is highly vesicular. Both have a crystal-rich matrix with mainly plagioclase microlites, and few pyroxene and olivine microlites, as well as pyroxene and olivine phenocrysts (figure 21). At this early stage of weathering, there appears to be almost no difference in the extent of alteration between the vesicular and non-vesicular samples. In both cores, almost all phenocrysts are still fresh, except for a few olivines weathering along grain boundaries. In both rinds, olivine microlites are completely altered, and pyroxenes are weathered along grain boundaries (figure 22).

### *Qas*

In the youngest unit, Qas, euhedral plagioclase and clinopyroxene (with some orthopyroxene) phenocrysts are present and in some samples, hornblende phenocrysts are

present as well. Plagioclase phenocrysts range in size from 0.3 to 5 mm and are the most weathered phases in some samples, but in others are less weathered than the pyroxene phenocrysts. Alteration patterns are just as varied in Qas as in Qtap; some plagioclase phenocrysts alter only in the centers, and others altering along edges or zones, leaving clean centers (figures 23, 24, and 25). Some plagioclases have lighter, yellow-orange stains associated with fractures (figure 26). This product is often seen associated with nearby, smaller alteromorphs of an unidentified primary mineral (figures 24 and 26).

In some plagioclase phenocrysts where glass inclusions are common, alteration is less than in similar grains from Qtap, where glass inclusions in a grain appear to preferentially weather. The rapid weathering of glass inclusions within plagioclase phenocrysts from Qtap causes the grain to weather more thoroughly than if it had no inclusions at all (recall figure 16). However, it appears in some plagioclase grains that the glass inclusions are less likely to alter in Qas than in Qtap (figure 27).

Primary, euhedral opaque minerals are usually associated with pyroxenes and 'bleed' red staining into the grains and the matrix (figure 23). Pyroxenes overall are more altered in Qas than in Qtap, especially along cleavages and fractures in which dark brown rusting, or brighter red products are observed (figures 28 and 29). Opaque microlites and small microlitic pseudomorphs dominate the matrix. Plagioclase microlites are usually unaltered, and little unaltered matrix glass remains.

Small, euhedral and unaltered hornblende phenocrysts (appx. 0.25 mm) are present in Qas 001. In Qas 005, small euhedral hornblende grains are rare. However, large (0.5 to 3 mm), partially replaced hornblende grains are present. These phenocrysts appear to

have been replaced by opaque iron oxides, which most likely occurred during decompression upon ascent of the magma (figure 30).

### *Qtapg*

In the intermediate age unit, Qtapg, there are, overall, fewer opaques present, and the few that are present are mainly associated with euhedral clinopyroxenes. Hornblende is more common in this unit. Pyroxenes (appx. 0.5 mm) are altered primarily along fractures and cleavages to a dark, red-brown product, but some phenocrysts remain fresh (figure 31).

While there is still a range in plagioclase alteration style, centers are usually more altered than the rest of the grain in Qtapg samples. Alteration products are usually dark brown-red or tan-orange, and are found in the numerous fractures that run through the samples (figure 32). In Qtapg 005, plagioclases appear to be stained, while hornblendes are clean. In a small crevice, beige secondary products (confirmed to be clay and hollandite by EDS) have grown or pooled (figure 33). These products are later discussed in the chapter regarding SEM analyses.

In Qtapg 004, the sample with two different weathering rinds (recall figure 13), plagioclase is the dominant phenocryst present, and the phenocrysts are consistently smaller (0.5 to 1 mm). In the core, plagioclases are either clean, or plucked out of the matrix (figure 34). In the white rind, all phenocrysts have been either completely altered to a beige product, or plucked out (figure 35). Throughout the groundmass, especially surrounding some of the voids where plagioclase phenocrysts once were is a red stain. Large phenocrysts (presumably clinopyroxene) have been altered to an orange, highly

birefringent, fibrous product (figure 36). In the red rind of 004, there are many fresh plagioclases remaining. However, there is abundant red staining of the matrix, particularly around plucked phenocrysts. A red-brown stain is observed along plagioclase grain boundaries, and a red-orange, amorphous product is present within some grains (figures 37 and 38). No fresh hornblende grains were observed in Qtapg 004. However, their presence in other samples from the unit may indicate that they were present, but have weathered and been replaced by clay, especially in the white rind.

Throughout the three units, plagioclase is the most consistently altered phenocryst phase. The highly crystalline matrices of the Qtapg samples are brightly stained red, while staining of the matrix in Qas and Qtap samples is generally tan or dark brown. Pseudomorphs after plagioclase phenocrysts in Qtapg are lighter in color than those in the other two units, and pyroxenes weather most readily in Qas samples.

Sample	rind thickness
<b>Qas 001 1</b>	0.5 - 1 mm
<b>Qas 002</b>	2-3 mm (red front 1.4 cm in)*
<b>Qas 003</b>	1-4 mm
<b>Qas 004</b>	1-3 mm
<b>Qas 005 a</b>	5mm (red front 1.4-3.7cm in)
<b>Qas 005 c</b>	1-3 cm (red front 7 mm-2.2 cm)
<b>Qtap 001 a</b>	1-2 mm
<b>Qtap 002 a</b>	<1 mm
<b>Qtap 002 b</b>	<1 mm - 1 mm
<b>Qtap 003 1</b>	0.5 - 1 mm
<b>Qtap 004 a</b>	4 mm (egg front 1-7 mm)**
<b>Qtap 005</b>	< 1 mm
<b>Qtapg 001 1</b>	5 mm
<b>Qtapg 002</b>	6-8 mm
<b>Qtapg 003 1</b>	2 mm (red front (only near R cut) 8 mm)
<b>Qtapg 004</b>	red: 3-4 mm, white: 2 cm***
<b>Qtapg 005 1</b>	2-4 mm
<b>Qtapg 005 2</b>	1-2 mm (ll to crevice, 4-10 mm)****

**Table 1.** Rind thickness measurements for Tecuamburro hand samples.

\* 'red front' indicates a dark red line, or weathering front, that is present beneath the exposed rind surface (see figure 11).

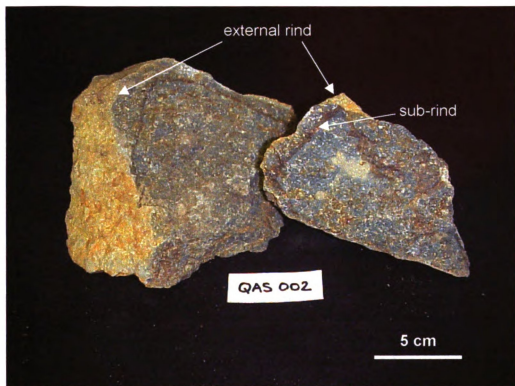
\*\* 'egg' indicates a small, isolated weathering front present in this sample (see figure 12).

\*\*\* This hand sample has two adjacent rind; one red, and one white (see figure 13).

\*\*\*\* The only part of this sample used was a small crevice, described in the Petrography and SEM Results sections.



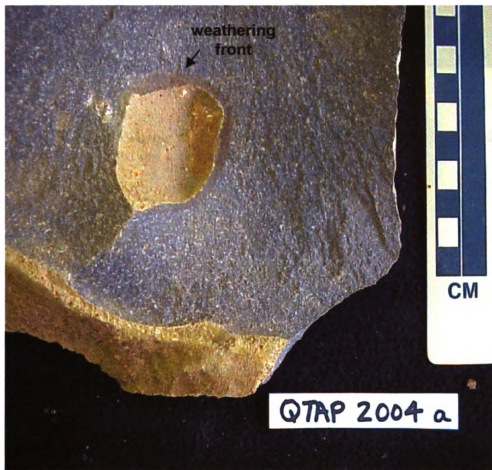
**Figure 10.** Hand sample photograph of Qtapg 002. Note the thick, white rind that is very different from the thinner, orange rind sometimes observed (e.g. figure 7).



**Figure 11.** Hand sample photograph of Qas 002. Beneath the external, yellow-orange rind, there is a faint red sub-rind or weathering front. Note that the matrix and phenocrysts between the external rind and the sub-rind appears fairly unaltered.



**Figure 12.** Hand sample photographs of Qtap 004. In the top photo, two pieces were broken apart to reveal the internal weathering front. In the hole from piece 'b' was an 'egg-shaped' concentration of clay material. The bottom photo is a closer look at the weathering front. Note the reddish matrix stain that lines the circumference of the front.





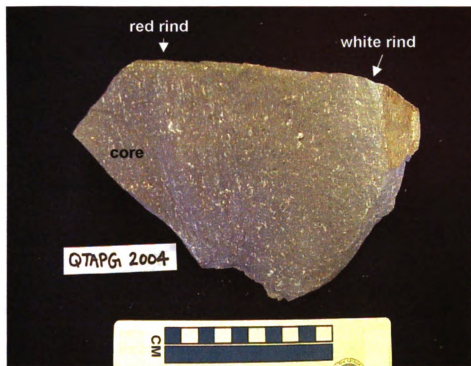


**Figure 13.** Hand sample photograph of Qtapg 004. This sample has two different rinds - one red, and one white, as indicated above.

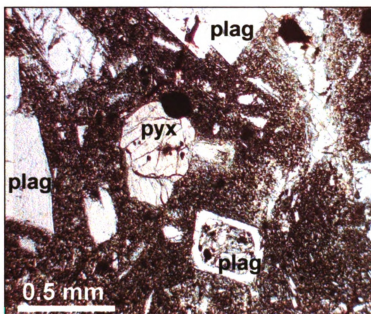


**Figure 14.** Qtap 003 core. Larger plagioclase phenocrysts are less altered than the smaller one, which has preferentially weathered in the center, while the rim has remained fresh. The pyroxene phenocryst is starting to weather only at a fracture, near a plagioclase grain boundary.

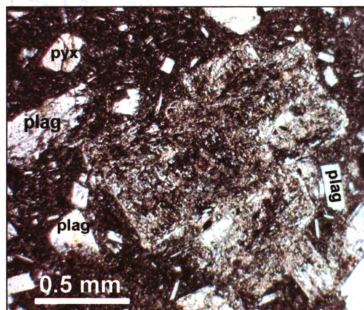


**Figure 15.** Qtap 003 1 rind. A group of extensively altered plagioclase grains. Note that some surrounding plagioclase grains are less altered.

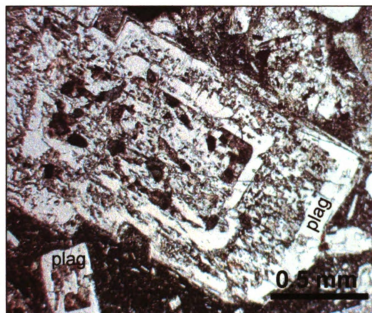


**Figure 16.** Qtap 003 rind. Plagioclase phenocrysts that have some sections that preferentially weathered along zones, or where glass inclusions once were. Note the tan alteration product (presumably clay) within the altered sections.

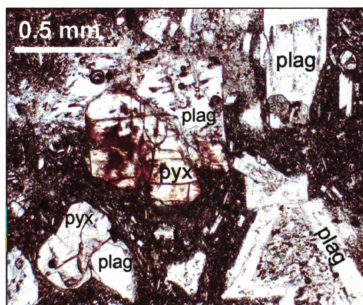


**Figure 17.** Qtap 003 rind. Highly altered pyroxene adjacent to denticularly altered plagioclase. Note the surrounding, variably weathered plagioclase phenocrysts, and nearly unweathered pyroxene (lower left).

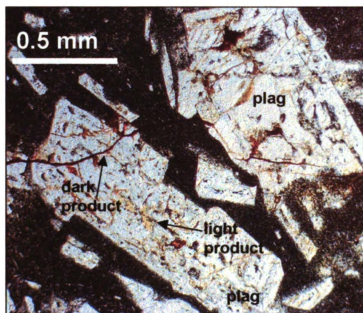


**Figure 18.** Qtap 004 rind. Plagioclase phenocrysts with two different alteration products. The darker, red-brown 'rusty' product is associated with the cross-cutting fracture. The lighter, yellow product is either a separate product, developing along a different pathway, or it is an earlier stage of the dark product.

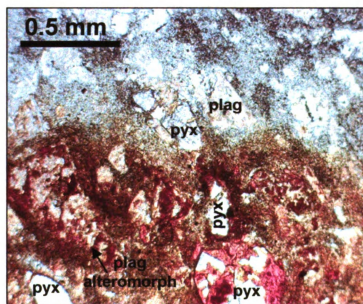


**Figure 19.** Qtap 004 e. The boundary between the weathering front and the rest of the rock. Note the drastically different degrees of plagioclase and pyroxene alteration.

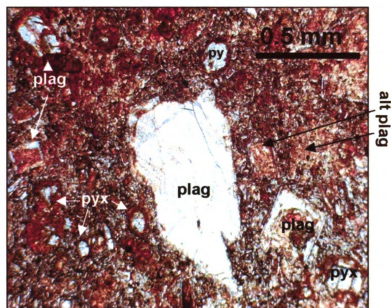


**Figure 20.** Qtap 004 e. Within the weathering front. Note that while most of the smaller grains have been completely altered, the large plagioclase remains surprisingly clean.

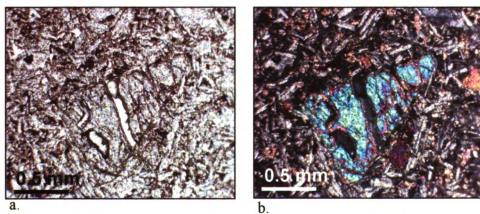


**Figure 21.** Qtap 002a core. Fresh olivine surrounded by a matrix of plagioclase and pyroxene microlites.

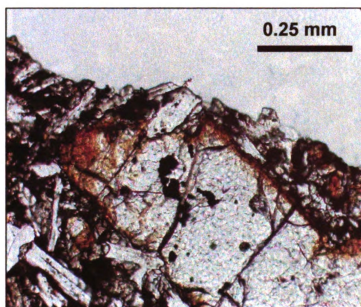


**Figure 22.** Qtap 002b rind. Pyroxene phenocryst, near a vesicle edge, that is starting to alter along grain boundaries.

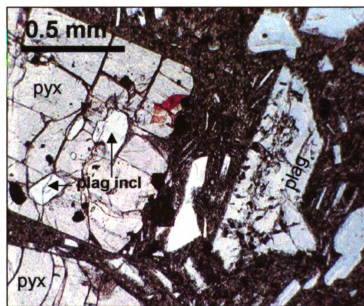


**Figure 23.** Qas 003 1 core. A slightly altered plagioclase. The pyroxenes are relatively clean, with some plagioclase and opaque inclusions. The top pyroxene is stained by alteration of an iron oxide in the matrix.



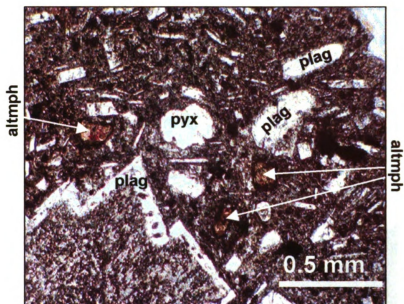


**Figure 24.** Qas 003 1 int. Most of the large plagioclase grain (lower left) has been altered, while the rim remains clean. Most plagioclase microlites are clean. Note the small, uncharacterized alteromorphs ('altmph') present in the matrix as well.

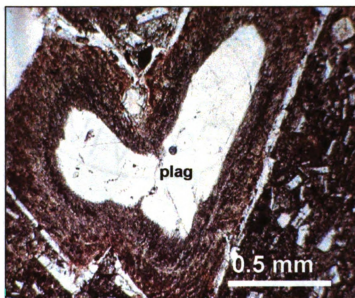


**Figure 25.** Qas 003 1 int. Plagioclase phenocryst with a clean core, very altered zone, and clean rim.

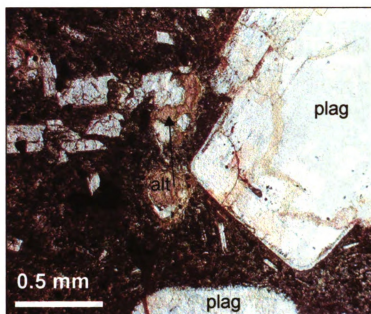


**Figure 26.** Qas 005c rind. Plagioclase phenocryst with yellow and orange staining along fractures. Small alteromorphs are to the left of the grain, adjacent to smaller plagioclases.

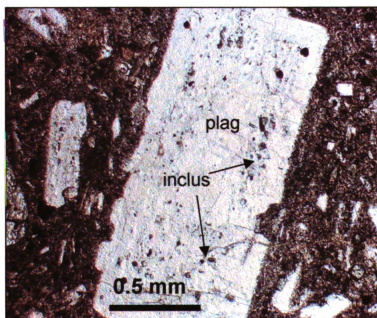


**Figure 27.** Qas 002 rind. Plagioclase phenocryst with glass inclusions that appear *not* to induce preferential weathering of the grain.



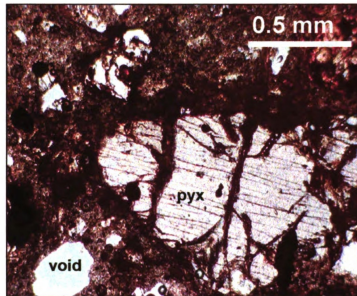


**Figure 28.** Qas 003 l rind. Pyroxene phenocryst with dark red-brown staining in cleavages, and along grain boundaries. A small phenocryst in the lower left has been plucked out, leaving a small void.

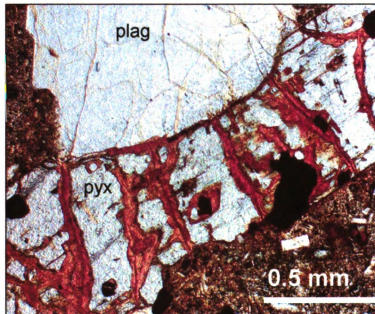


**Figure 29.** Qas 002 rind. Clean plagioclase phenocryst next to a highly altered pyroxene associated with opaques.

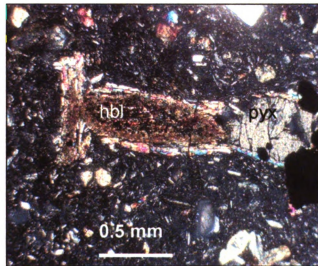
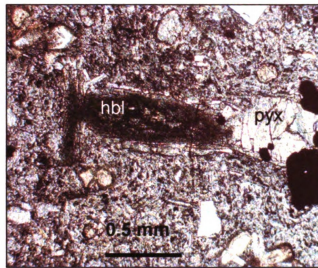


**Figure 30.** Qas 005a core. Pyroxene phenocryst near hornblende phenocryst that has been partially replaced by Fe-oxides and possibly clay.

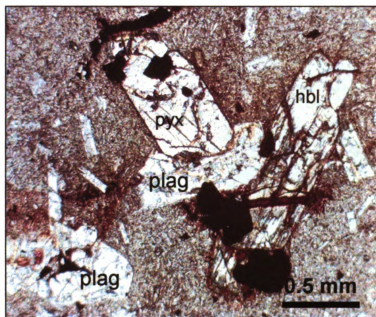


**Figure 31.** Qtapg 002 core. Altered pyroxene and hornblende with secondary product-filled fractures. Note that the dark product in the hornblende is associated with an opaque, while the product in the pyroxene is much lighter.

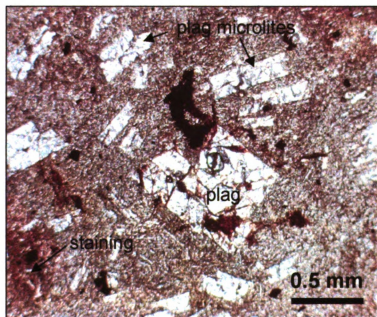


**Figure 32.** Qtapg 002 core. Plagioclase phenocryst with dark red alteration, surrounded by smaller, cleaner plagioclase microlites. Note the staining of the glass in the lower left corner.

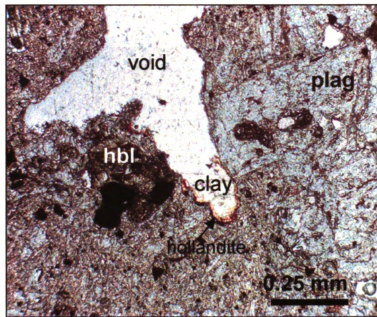


**Figure 33.** Qtapg 005 rck. Crevice that has partially filled with clay and is lined with a secondary hollandite (see SEM results, figure 68) surrounded by hornblende and plagioclase phenocrysts.

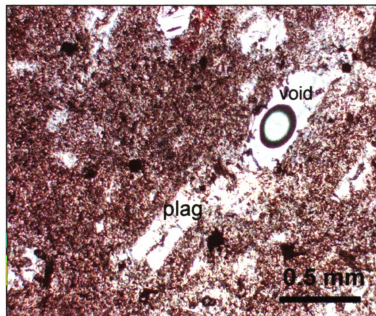


**Figure 34.** Qtapg 004 core. Clean plagioclase adjacent to a void, from which a grain was plucked.

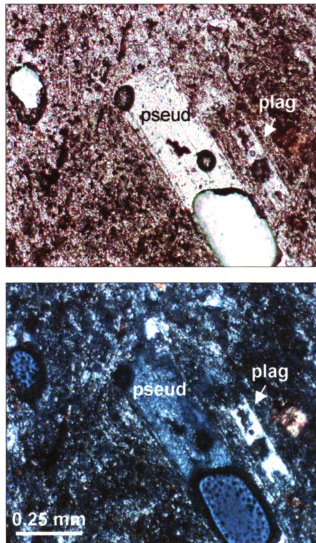


**Figure 35.** Qtapg 004 white rind. Clay pseudomorph of a plagioclase, next to a clean, smaller plagioclase grain. Note that the rim of the larger grain remains intact, and that half of the grain has been plucked out.

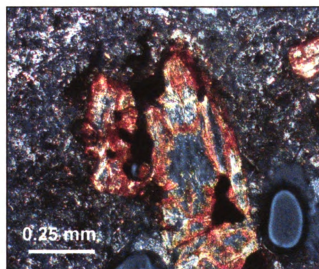
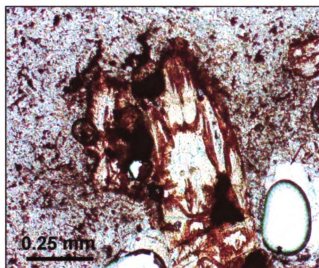


**Figure 36.** Qtapg 004 white rind. Alteromorph that represents what, if anything, is left of the phenocrysts in the white rind. This alteromorph is most likely replacing clinopyroxene.

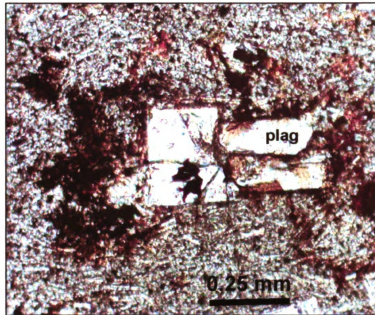


**Figure 37.** Qtapg 004 red rind. Red and brown staining of the matrix and tan alteration along plagioclase grain boundaries.

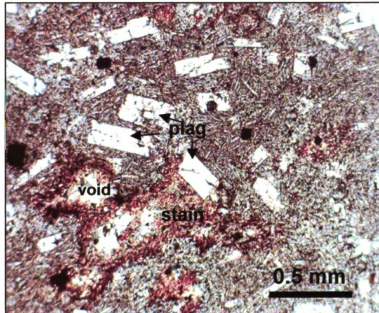


**Figure 38.** Qtapg 004 red rind. Red and yellow staining around plucked plagioclase grains, adjacent to clean plagioclase grains.



## **Whole-Rock Chemical Analyses**

Element concentrations are listed in Appendix C. Classification of the Tecuamburro core samples based on major-element chemistry is shown in figure 39. Samples from the oldest unit, Q<sub>tap</sub>, range from basalt to basaltic andesite, samples from the middle unit, Q<sub>tapg</sub>, range from andesite to dacite-trachydacite, and samples from the youngest unit, Q<sub>as</sub>, are andesites.

The alteration of Tecuamburro samples is assumed to have been isovolumetric, since none of the boxwork structures of weathered phenocrysts, or void spaces where grains once were, show any sign of compression or volume change. Therefore, the composition of the samples is discussed in terms of volumetric concentration, and data are displayed in reaction progress diagrams that plot bulk density vs. volumetric concentration (Gardner, 1980; and Eggleton et al., 1987). Volumetric concentration (a reflection of compositional changes due to weathering) is obtained by multiplying concentration by weight – either wt% or ppm - of the element by the bulk density of the sample, and the units are  $\text{cg/cm}^3$  or  $\mu\text{g/cm}^3$ .

Table 2 lists the relative change from core to rind of the volumetric concentrations for all the elements. In this table, a negative percentage indicates a lower volumetric concentration of the oxide or trace element in the weathering rind relative to the core, while a positive percentage indicates a higher volumetric concentration. For major elements, an oxide that changes in volumetric concentration from core to rind by 5-10% is considered mobile, and one that changes more than 10% is considered highly mobile. For trace elements, a change in volumetric concentration from core to rind of >20% is



considered notable. These threshold conditions were chosen because they lie well outside the possible error for the analytical methods used.

### *Major Elements*

Major-element oxide volumetric concentrations are plotted versus bulk density in figure 40. The core concentrations of  $\text{Al}_2\text{O}_3$ ,  $\text{MnO}$ ,  $\text{Fe}_2\text{O}_3$ ,  $\text{CaO}$ , and  $\text{MgO}$  are generally highest in Qtap, and lowest in Qtapg. Qtapg and Qas cores are highest in  $\text{SiO}_2$ , while Qtapg is highest in  $\text{K}_2\text{O}$  and  $\text{Na}_2\text{O}$ . These trends are not surprising, as samples from Qtapg are the most silicic, and those from Qtap the most mafic. Overall,  $\text{P}_2\text{O}_5$  is highest in Qtap cores, but two samples from Qas are enriched in  $\text{P}_2\text{O}_5$  (and  $\text{K}_2\text{O}$ ) relative to the rest of the unit (figure 40f and i). In most samples, major element volumetric concentrations either show no change, or decrease from core to rind.

In unit Qas, the rind of sample 003 is depleted relative to the core in all major elements by 12-30% (table 2). The rind of sample 004 is depleted in all major elements, except for  $\text{Fe}_2\text{O}_3$  and  $\text{K}_2\text{O}$ . Losses of  $\text{CaO}$ ,  $\text{MgO}$ ,  $\text{Na}_2\text{O}$ , and  $\text{P}_2\text{O}_5$  in the rind of 004 are significant (16-26%; table 2). The rind of 005a is depleted relative to the core in all major elements except for  $\text{Al}_2\text{O}_3$ , particularly  $\text{K}_2\text{O}$ ,  $\text{MnO}$ ,  $\text{MgO}$ ,  $\text{CaO}$ , and  $\text{P}_2\text{O}_5$  (11-18%). The rind of 005c is depleted in all major elements except  $\text{Fe}_2\text{O}_3$  and  $\text{MgO}$ , while the rind of 002 is only significantly depleted in  $\text{MnO}$  and  $\text{MgO}$  (table 2). The rind of 001 is only slightly depleted in some major elements. Calcium oxide is the only major element oxide mobile in all Qas samples, while  $\text{SiO}_2$ ,  $\text{TiO}_2$ ,  $\text{Al}_2\text{O}_3$ ,  $\text{MnO}$ ,  $\text{MgO}$ , and  $\text{Na}_2\text{O}$  are mobile in all but one sample (table 2).  $\text{Fe}_2\text{O}_3$  is the least mobile, lost only in two of the six rinds.

In Qtap, the rind of sample 004 is significantly depleted (12-50%) relative to the core in all major elements (table 2). However, this apparently large loss in the rind could be an artifact of the large bulk density difference between the two samples (core = 2.13 g/cm<sup>3</sup>, rind = 1.59 g/cm<sup>3</sup>), as it does not appear more weathered than the other samples in the unit. The rind of 001 is also depleted in all major elements relative to the core, especially CaO (18%) and Na<sub>2</sub>O (15%; table 2). The rind of 002a is slightly depleted in all major element oxides except for Fe<sub>2</sub>O<sub>3</sub> and P<sub>2</sub>O<sub>5</sub>, while 002b is only slightly depleted in some major elements. Sample 005 does not significantly change from core to rind in any major element concentrations. There is no element that is mobile in all Qtap samples, although CaO, Na<sub>2</sub>O, and K<sub>2</sub>O are mobile in all but one sample (table 2).

Among the three units, major elements are most mobile in Qtapg. SiO<sub>2</sub>, CaO, Na<sub>2</sub>O, and P<sub>2</sub>O<sub>5</sub> are mobile in every sample, and CaO has the highest percent change of all the oxides. MnO, MgO, and K<sub>2</sub>O are mobile in all but one. The red rind of 004 is depleted in most major elements by 10 to 24%, but slightly enriched in MnO (table 2). The white rind of 004 is enriched in MnO by 39% and Fe<sub>2</sub>O<sub>3</sub> by 5%, and depleted in all other major element oxides except for TiO<sub>2</sub>, Al<sub>2</sub>O<sub>3</sub>, and K<sub>2</sub>O. The rind of 001 is enriched in MnO (24%) and Fe<sub>2</sub>O<sub>3</sub> (30%), but depleted in all major elements except TiO<sub>2</sub> and Al<sub>2</sub>O<sub>3</sub>. Samples 002 and 003 decrease from core to rind (in all but Fe<sub>2</sub>O<sub>3</sub>) by 6 to 74%, although 002 is much more depleted in most oxides than 003. For instance, while the rind of 002 is depleted by 27% of K<sub>2</sub>O, the rind of 003 has only lost 6% (table 2).

In all three units, Fe<sub>2</sub>O<sub>3</sub> is the least mobile major element oxide. Oxides that were previously considered immobile, such as TiO<sub>2</sub> and Al<sub>2</sub>O<sub>3</sub>, are slightly (TiO<sub>2</sub>) to

moderately ( $\text{Al}_2\text{O}_3$ ) mobile in all three units. CaO is mobile in all samples, except one (Qtap 005).

### *Trace Elements*

Volumetric concentration values for select trace elements are plotted versus bulk density in figure 41. Rare-earth element spider diagrams for each sample are plotted in figures 42-44.

Core samples from Qtap are the most mafic, and generally lower in Rb, Ba, and Pb, and higher in Sr, than the other two units (figure 41). One core (003) is enriched in Nb, Ba, Y and REE, except for Ce, relative to all other samples in the unit, and another core sample (004) is enriched in Rb, Th, and U. More silicious core samples from Qtapg generally have higher concentrations of Rb, Ba, Pb, Th, and U, as well as lower Sr than those from the other two units. Sample 002 is enriched in Nb and Y relative to other samples in the unit, and core samples 002 and 004 are particularly enriched in Rb, Y, and U (figure 41). Core volumetric concentrations of Y, Nb, Th, and U in from Qas often overlap with samples from Qtap. The cores of Qas 005a and 005c are enriched in Rb, Sr, and Ba relative to the rest of the unit, while the core of 004 is enriched in Pb.

As discussed above, table 2 lists the relative change from core to rind of the volumetric concentrations for all elements. Within the Qtap unit, Zr, Th, and U are relatively immobile in all samples. Sample 004, as with the major elements, shows the greatest change in volumetric concentration of trace elements from core to rind.

Strontium, Y, Ba, Ce, Ho, Er, Yb, and Lu are mobile in Qtap 004 only. However, because the relative depletion is consistently around 30% and the negative Ce anomaly is

only slight (figure 42e), it is possible that a large difference in bulk density (core = 2.13 g/cm<sup>3</sup>, rind = 1.59 g/cm<sup>3</sup>) is responsible for the apparent depletions in the rind, not element mobility alone.

The rind of Qtap 003 is enriched in LREE and MREE except Ce (figure 42d). Trace elements in the two most mafic samples of the Tecuamburro suite, 002a and 002b, behave only slightly differently (figure 42b and c). The rind of 002a (a non-vesicular sample) is depleted in Rb by 28%, while the rind of 002b (a vesicular sample) is enriched in Pb by 26%. The rinds of 001 and 005 are depleted in Nb by 59% and 36%, respectively (table 2).

As is the case with major elements, trace elements are most mobile in Qtapg. Elements in sample 005 are the least mobile in the Qtapg suite; the rind is depleted only in Nb by 30%. Zirconium and Th are immobile in all Qtapg samples (table 2). The rind of sample 001 is depleted in Rb, Sr, Nb, and U by 20 to 43%, but enriched in Y (39%), Ba (26%; table 2), and the REE (29-65%) (figure 43a). The rinds of 002 and 003 are depleted in Sr, Nb, Ba, and the REE by 21-76% (figure 43b and c), and the rind of 002 is additionally depleted in Rb, Y, Pb, and U by 31-58% (table 2).

The red and white rinds of Qtapg 004 behave very differently. The red rind is slightly depleted in Rb, Sr, and Lu relative to the core (by 20-23%), but enriched in La, Ce, Pr, Nd, and Sm (26-52%) (figure 43d). The white rind is also depleted in Sr, in addition to Y, Nb, Ba, Pb (table 2), and all the REE by 22-80% (figure 43d).

In Qas, Pb, Th, and U are relatively immobile. Nb is mobile in all but one sample (Qas 001; table 2). The rind of 001 is depleted only in Pr, by 21%, while the rind of 002 is depleted only in Nb, by 35%. The rind of 005c is depleted in both Nb (29%) and Rb

(31%), while the rind of 005a is depleted in Rb, Y, Nb, Gd, Dy, Ho, and Lu by 20–41% (table 2).

The rind of Qas 003 is depleted in Sr, Y, Zr, Nb by 20–55% (table 2), and the REE by 25–33% (figure 44c). However, as in the case of Qtap 004, this nearly parallel depletion in volumetric concentration of the REE and minor Ce anomaly may be enhanced by the large difference in bulk density (core = 2.2 g/cm<sup>3</sup>, rind = 1.75 g/cm<sup>3</sup>). The rind of Qas 004 is depleted in Sr (20%) and Nb (43%), but enriched in Rb (22%), Ba (27%; table 2), and the LREE (except Ce) by 26–80% (figure 44d).

Throughout the suite of Tecuamburro rocks from the three units, only Th is immobile in all samples. Zirconium is only mobile in one sample (Qas 003), and U in two (Qtapg 001 and 002). Niobium, if mobile in a given sample, is consistently depleted in the rind. Other elements, such as Rb, Y, and Ba, vary in mobility – in some instances they are enriched, and in other instances depleted in the rind, relative to the core. Rare earth elements are also varied in behavior, although in most cases (except Qtapg 004) the core and rind pairs have very similar patterns, even if one is enriched in REE over the other. In Qas 005a and Qtap 004, the rinds are only slightly depleted in REE, and the Ce anomaly is smaller than in other samples (figures 44e and 42e). In the rinds of Qtap 003, Qas 004, and the red rind of Qtapg 004, LREE are enriched, and a negative Ce anomaly is observed in the rind and the cores (figures 42d, 44d, and 43d). The white rind of Qtapg 004, however, is strongly depleted in REE relative to the core (figure 43d). In Qtapg 002 and 003, the rinds are depleted in REE, and the Ce anomaly is observed also in the cores (figure 443b).

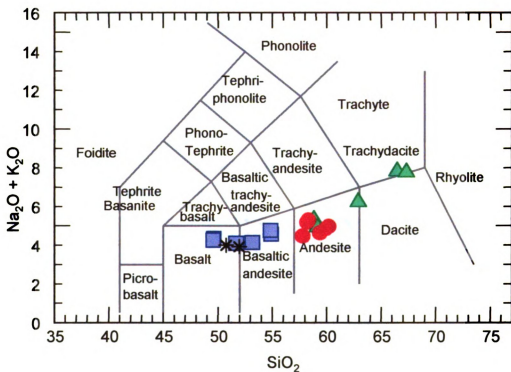


**Figure 39.** Classification of Tecuamburro core samples. Circles represent Qas, the youngest unit, triangles represent Qtapg, the middle unit, and squares represent the oldest unit, Qtap. Asterisks represent samples from recent lavas, for comparison.

# Unit QTAPG

sample	001	002	003	004r	004w	005
SiO <sub>2</sub>	-13%	-34%	-15%	-18%	-10%	-7%
TiO <sub>2</sub>	4%	-8%	-8%	-15%	2%	1%
Al <sub>2</sub> O <sub>3</sub>	-3%	-24%	-18%	-19%	-1%	-2%
Fe <sub>2</sub> O <sub>3</sub>	30%	-1%	-2%	-17%	5%	-1%
MnO	24%	-54%	-17%	10%	39%	3%
MgO	-6%	-37%	-23%	-13%	-14%	-2%
CaO	-47%	-74%	-35%	-19%	-49%	-13%
Na <sub>2</sub> O	-27%	-55%	-31%	-18%	-33%	-8%
K <sub>2</sub> O	-14%	-27%	-6%	-21%	-4%	-9%
P <sub>2</sub> O <sub>5</sub>	-9%	-66%	-23%	-24%	-77%	10%
Rb	-33%	-31%	-5%	-20%	7%	-4%
Sr	-42%	-76%	-37%	-23%	-48%	-12%
Y	39%	-58%	-13%	-14%	-83%	7%
Zr	3%	-10%	-9%	-16%	0%	1%
Nb	-43%	-65%	-39%	-15%	-22%	-30%
Ba	26%	-63%	-29%	14%	-36%	6%
La	65%	-39%	-19%	41%	-78%	0%
Ce	34%	-65%	-33%	26%	-60%	-2%
Pr	65%	-50%	-21%	52%	-77%	-1%
Nd	65%	-52%	-21%	48%	-77%	-1%
Sm	56%	-57%	-22%	27%	-77%	0%
Eu	41%	-61%	-23%	17%	-80%	0%
Gd	41%	-58%	-20%	11%	-79%	0%
Tb	40%	-56%	-21%	5%	-78%	2%
Dy	40%	-54%	-21%	-3%	-79%	3%
Ho	37%	-55%	-22%	-10%	-79%	2%
Er	32%	-53%	-21%	-13%	-79%	3%
Yb	29%	-53%	-25%	-15%	-77%	9%
Lu	31%	-51%	-25%	-20%	-77%	7%
Pb	-18%	-57%	7%	11%	-35%	-2%
Th	18%	-14%	-8%	-10%	1%	3%
U	-20%	-46%	-14%	-11%	-18%	-2%

**Table 2.**

Percent change from core to rind of volumetric concentration of the elements analyzed (Crind-Ccore)/Ccore. Major element values that changed 5%-10% are shaded lightly, and >10% shaded darkly. Trace elements that changed 20% or more are shaded darkly. A negative % indicates loss in the rind. 004r is the red rind of 004; 004w the white rind.

# Unit QTAP

sample	001	002a	002b	003	004	005
SiO <sub>2</sub>	-11%	-7%	-3%	-9%	-31%	-1%
TiO <sub>2</sub>	-9%	-5%	-1%	-4%	-13%	-1%
Al <sub>2</sub> O <sub>3</sub>	-11%	-8%	-3%	-7%	-12%	-1%
Fe <sub>2</sub> O <sub>3</sub>	-8%	-4%	0%	-6%	-14%	0%
MnO	-11%	-7%	-3%	-2%	-50%	6%
MgO	-11%	-8%	1%	-4%	-35%	-2%
CaO	-18%	-8%	-6%	-13%	-39%	-3%
Na <sub>2</sub> O	-15%	-12%	-5%	-10%	-33%	-1%
K <sub>2</sub> O	-7%	-7%	-5%	-6%	-34%	-1%
P <sub>2</sub> O <sub>5</sub>	-11%	-4%	-6%	-7%	-21%	-1%
Rb	-8%	-28%	-9%	-1%	-33%	-4%
Sr	-18%	-10%	-5%	-11%	-39%	-1%
Y	-2%	-6%	-7%	1%	-30%	-1%
Zr	-10%	-6%	-3%	-8%	-15%	-1%
Nb	-59%	-8%	-7%	6%	-47%	-36%
Ba	14%	-3%	6%	8%	-21%	3%
La	-1%	-8%	-7%	69%	-30%	-3%
Ce	-13%	-6%	-7%	-3%	-31%	3%
Pr	-4%	-3%	-6%	98%	-33%	-3%
Nd	-7%	-4%	-6%	96%	-34%	-2%
Sm	-8%	-3%	-6%	89%	-34%	-3%
Eu	-8%	-5%	-3%	70%	-34%	-3%
Gd	-7%	-5%	-7%	53%	-32%	-2%
Tb	-6%	-6%	-7%	38%	-30%	-3%
Dy	-6%	-6%	-9%	23%	-26%	1%
Ho	-4%	-5%	-8%	10%	-26%	0%
Er	-8%	-5%	-6%	1%	-26%	-4%
Yb	-11%	-2%	-10%	0%	-30%	-2%
Lu	-9%	-2%	-5%	-6%	-30%	-1%
Pb	-8%	-1%	26%	-8%	-23%	-1%
Th	-8%	-8%	-1%	-4%	-12%	2%
U	-10%	-2%	-12%	-6%	-1%	3%

Table 2 continued.



# Unit QAS

sample	001	002	003	004	005a	005c
SiO <sub>2</sub>	-9%	-1%	-20%	-7%	-9%	-10%
TiO <sub>2</sub>	-6%	2%	-12%	-6%	-5%	-6%
Al <sub>2</sub> O <sub>3</sub>	-5%	2%	-20%	-7%	-2%	-5%
Fe <sub>2</sub> O <sub>3</sub>	0%	0%	-12%	-4%	-7%	-4%
MnO	3%	-16%	-14%	-8%	-14%	-9%
MgO	-5%	-11%	-23%	-19%	-16%	-4%
CaO	-7%	-5%	-30%	-26%	-12%	-7%
Na <sub>2</sub> O	-4%	-5%	-28%	-18%	-5%	-13%
K <sub>2</sub> O	-4%	-3%	-16%	0%	-18%	-23%
P <sub>2</sub> O <sub>5</sub>	-4%	-1%	-28%	-16%	-11%	-6%
Rb	11%	-9%	-5%	22%	-41%	-31%
Sr	-4%	-4%	-28%	-20%	-10%	-10%
Y	-11%	-3%	-28%	-10%	-26%	-18%
Zr	9%	-4%	-20%	-6%	-10%	-9%
Nb	-1%	-35%	-55%	-43%	-23%	-29%
Ba	9%	6%	2%	27%	9%	-3%
La	-19%	2%	-31%	85%	-9%	-15%
Ce	-12%	-3%	-33%	-16%	-13%	-17%
Pr	-21%	1%	-33%	67%	-11%	-17%
Nd	-18%	-1%	-31%	60%	-13%	-17%
Sm	-19%	-1%	-30%	40%	-15%	-14%
Eu	-12%	-6%	-23%	31%	-8%	-11%
Gd	-19%	-4%	-30%	26%	-20%	-13%
Tb	-18%	1%	-30%	15%	-19%	-9%
Dy	-10%	3%	-26%	0%	-21%	-14%
Ho	-10%	0%	-25%	-7%	-22%	-14%
Er	-11%	1%	-29%	-13%	-19%	-17%
Yb	-13%	-1%	-27%	-6%	-16%	-19%
Lu	-13%	-3%	-27%	-8%	-22%	-14%
Pb	4%	14%	-16%	1%	-2%	-7%
Th	-1%	-10%	-17%	-4%	-1%	-7%
U	-1%	-7%	-17%	5%	-6%	-15%

Table 2 continued.

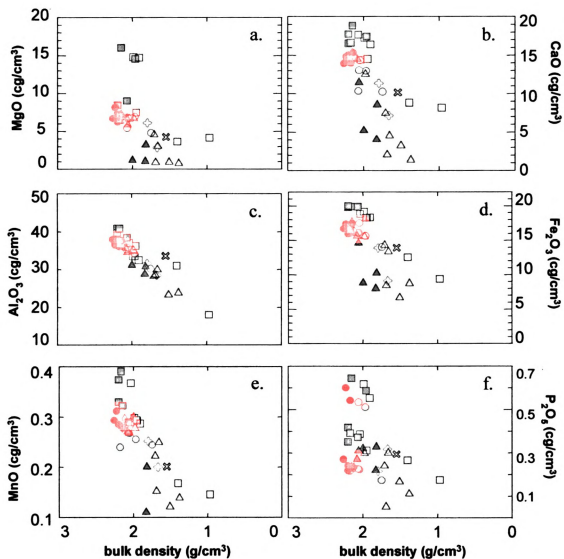


**Figure 40.** Major element volumetric concentration plots for Tecuamburro samples.  $\blacksquare$  = Qtap,  $\blacktriangle$  = Qtapg, and  $\bullet$  = Qas. Filled symbols represent cores, open symbols represent rinds.  $\times$ ,  $\diamond$ , and  $\diamond$  represent intermediate and/or unique samples from Qtap, Qtapg, and Qas, respectively.

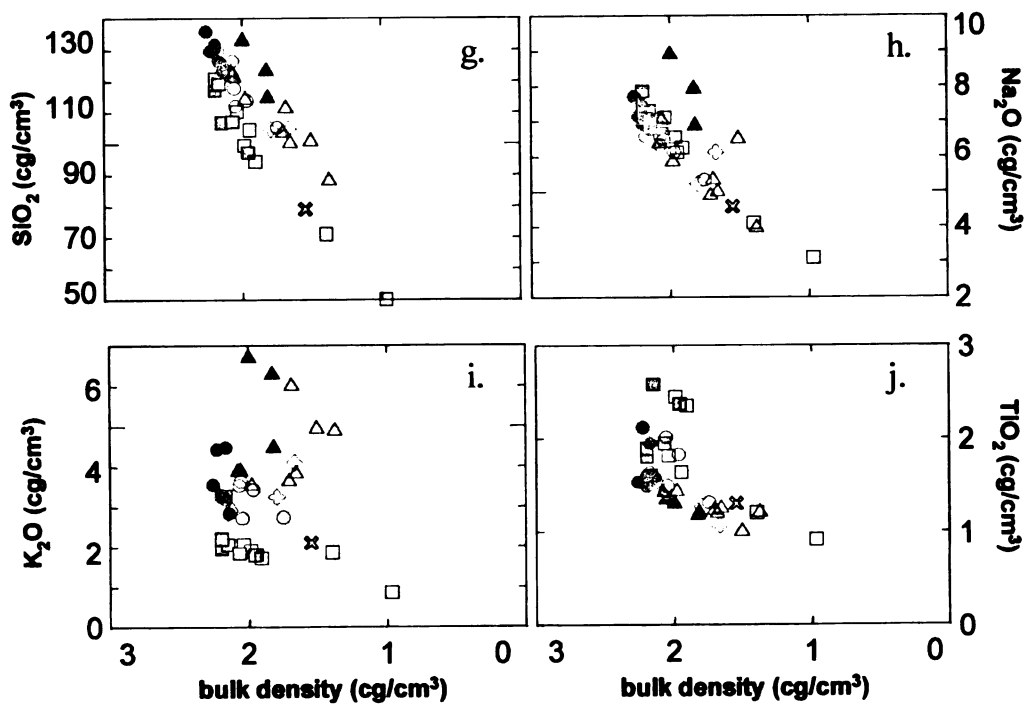
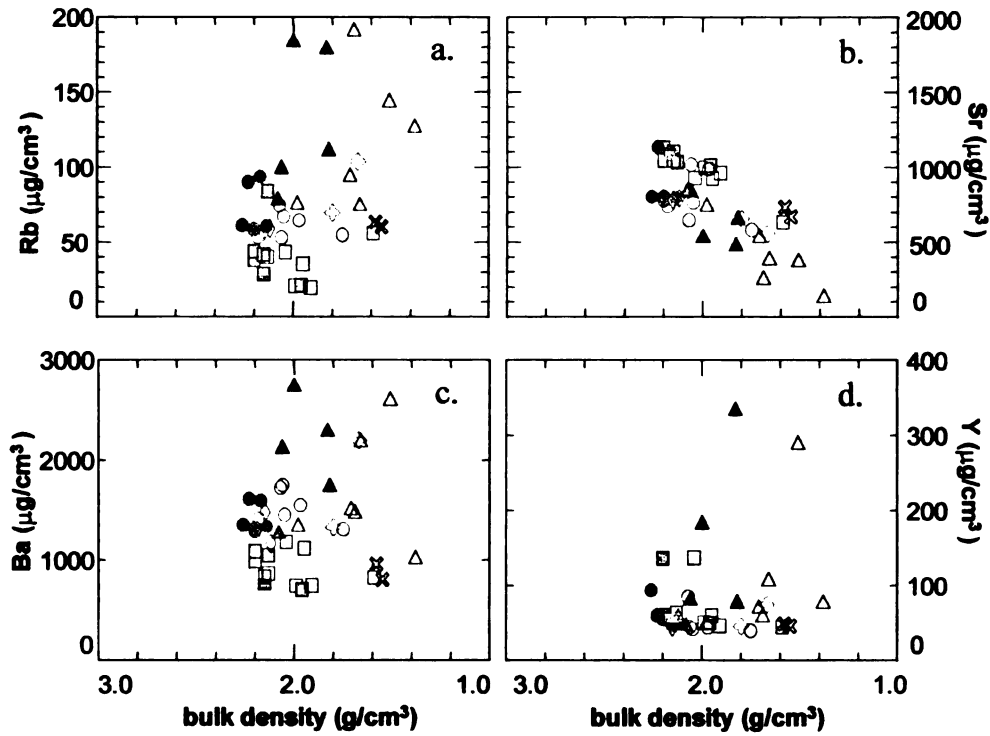
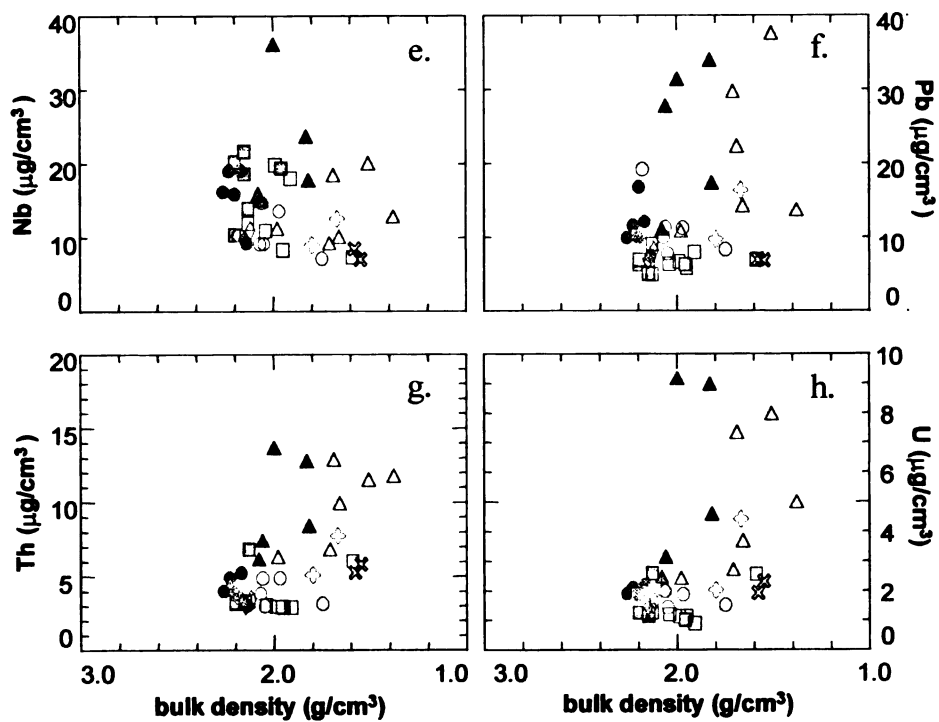


Figure 40 continued.



**Figure 41.** Trace element volumetric concentration plots for Tecuamburro samples. ■ = Qtap, ▲ = Qtapg, and ● = Qas. Filled symbols represent cores, open symbols represent rinds. x, ◇, and ◇ represent intermediate and/or unique samples from Qtap, Qtapg, and Qas, respectively.



**Figure 41 continued.**

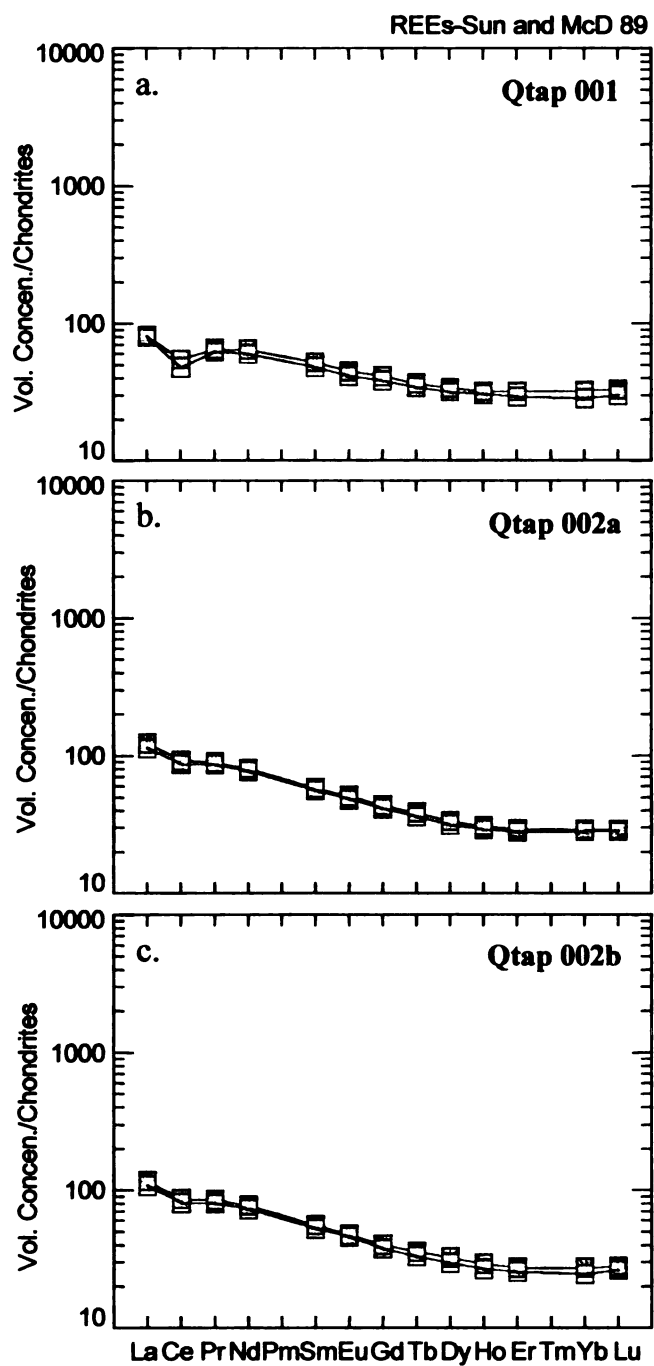


**Figure 42.** REE plots of samples from Qtap, in volumetric concentrations.  $\blacksquare$  = core,  $\square$  = rind, and  $\times$  = the subsurface weathering rind, or 'egg.'

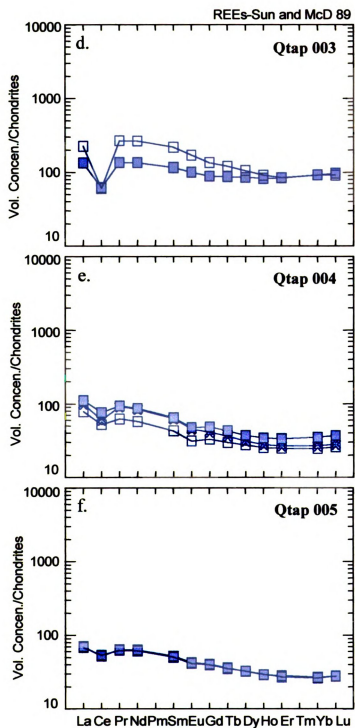


**Figure 42 continued.**

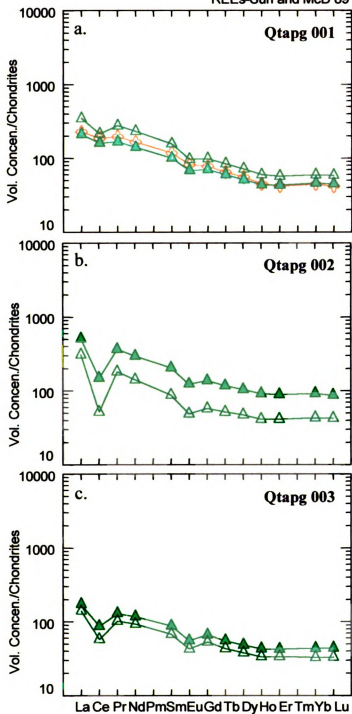


**Figure 43.** REE plot of samples from Qtapg, in volumetric concentrations.  $\blacktriangle$  = core,  $\diamond$  = intermediate, and  $\triangle$  = rind.



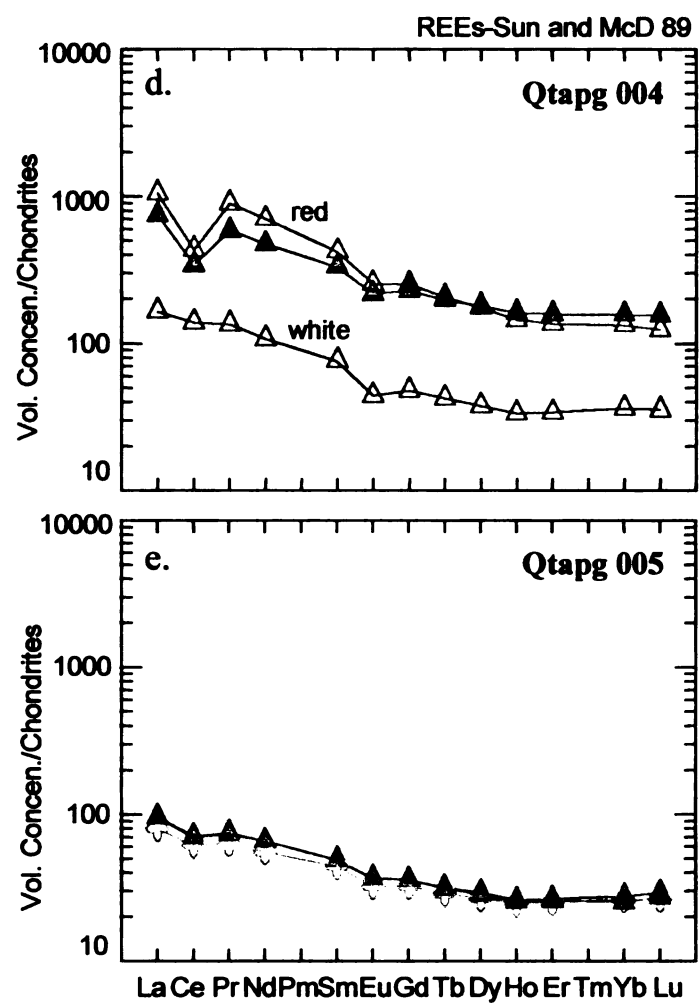


**Figure 43 continued.**

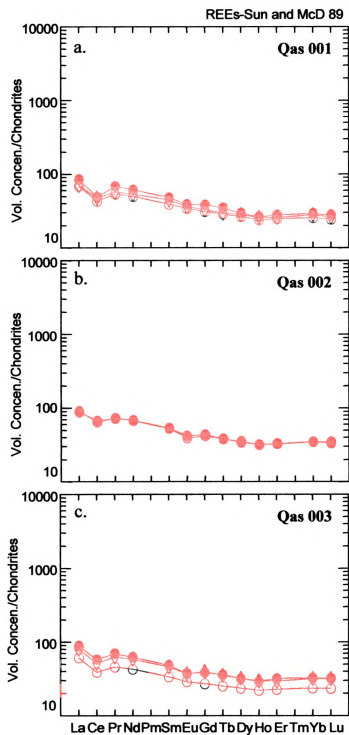


**Figure 44.** REE plot of samples from Qas, in volumetric concentrations. ● = core, ◇ = intermediate, ○ = rind.

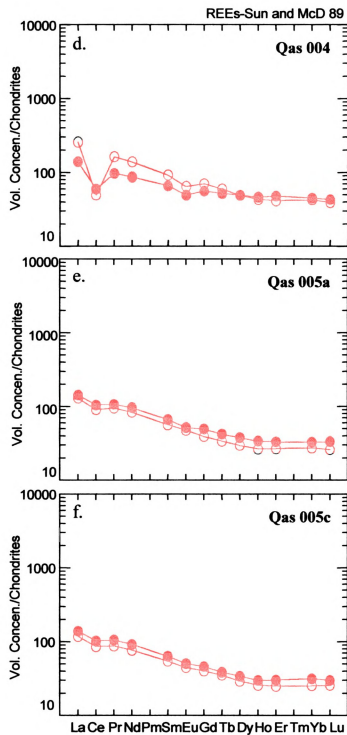


**Figure 44 continued.**

## **X-ray Diffraction**

X-ray diffraction (XRD) sample preparation methods are discussed in Appendix B. Eight samples (Qtapg 004c, Qtapg 004rr, Qtapg 004rw, Qtapg 002r, Qas 004r, Qtap 004ar, and two corestone samples from unit Qtap, 0512008r, and 051200 8a) were analyzed using a Rigaku Geigerflex X-ray diffractometer. These samples were chosen from the suite because they represent a range in composition (figure 45) and are variably weathered. Diffractograms were collected with Cu-K $\alpha$  radiation at 35 kV, 25 mA in the 3-30° 2 $\theta$  range. Counts were recorded at 0.05° 2 $\theta$  intervals for 5 seconds. The divergence slit was 0.5°, the receiving slit 0.3 mm, and the anti-scatter slit 2.0°. Diffraction peaks were interpreted using Brindley and Brown (1980).

Feldspar peaks are present in all diffractograms. Kaolinite and/or halloysite are common. Smectite is present in three of the most felsic of the eight samples. Gibbsite and possibly barite peaks are present in select samples.

Both the core (c) and red rind (r) of Qtapg 004 contain smectite and feldspar (figures 46 and 47). The white rind of Qtapg 004 (rw) contains smectite and possibly barite (figure 48). Feldspar peaks in 004rw are either obscured by surrounding broad peaks, or very small because most of the feldspar has been weathered out of the sample. The Qtapg 004 set of samples is the only set containing smectite. This common weathering product of amphibole (Velbel, 1989), as expected, occurs in samples containing hornblende.

The rind of Qtapg 002r is similar in chemical composition to the white rind of Qtapg 004. However, it does not contain smectite, but kaolinite (figure 49). It is possible

that in the Qtapg 004 and 002 samples, primary minerals are weathering at different rates, resulting in different secondary products. For instance, in all three Qtapg 004 samples, petrographically most plagioclase phenocrysts appear to have been completely replaced by a white clay mineral (presumably the smectite detected here). In the rind of Qtapg 002, a darker, tan-brown product (kaolinite) pervades many grains and fractures, but phenocrysts remain more intact. Alternatively, Qtapg 004 may be at a later stage of alteration than Qtapg 002.

The Qas sample (004 rind) contains some kaolinite, and feldspar (figure 50). The rind of Qtap 004 is the only sample that contains gibbsite (figure 51). The rind and exfoliated ‘shells’ of 0512008 (the corestone collected near Qtap 003) are shown in figure 52. In the rind, only kaolinite and feldspar peaks are present (figure 53). In an exfoliated shell of the corestone, stronger kaolinite and possible halloysite peaks are present (figure 54). In this heavily weathered sample, some feldspar is still present.

Secondary-electron images of plagioclase phenocrysts from the 0512008 samples confirm the XRD results. A fracture in the surface of a plagioclase from the core of the corestone (0512008c) contains material with morphology suggestive of kaolinite or halloysite rods (figure 55; e.g. Jeong, 1998). The surface of a plagioclase from the rind of the corestone (0512008rc) has an etch pit, with rolled halloysite balls within and around it (figure 56; e.g. Robertson and Eggleton, 1991). Halloysite formation is described as a “spiral development” that can result in, among other things, irregularly-shaped halloysite polygons. The plagioclase phenocryst was likely weathered to kaolinite, and kaolinite to its hydrated daughter, halloysite. The process of halloysite

formation removes material from the surface of the plagioclase grain, leaving only the pit behind.

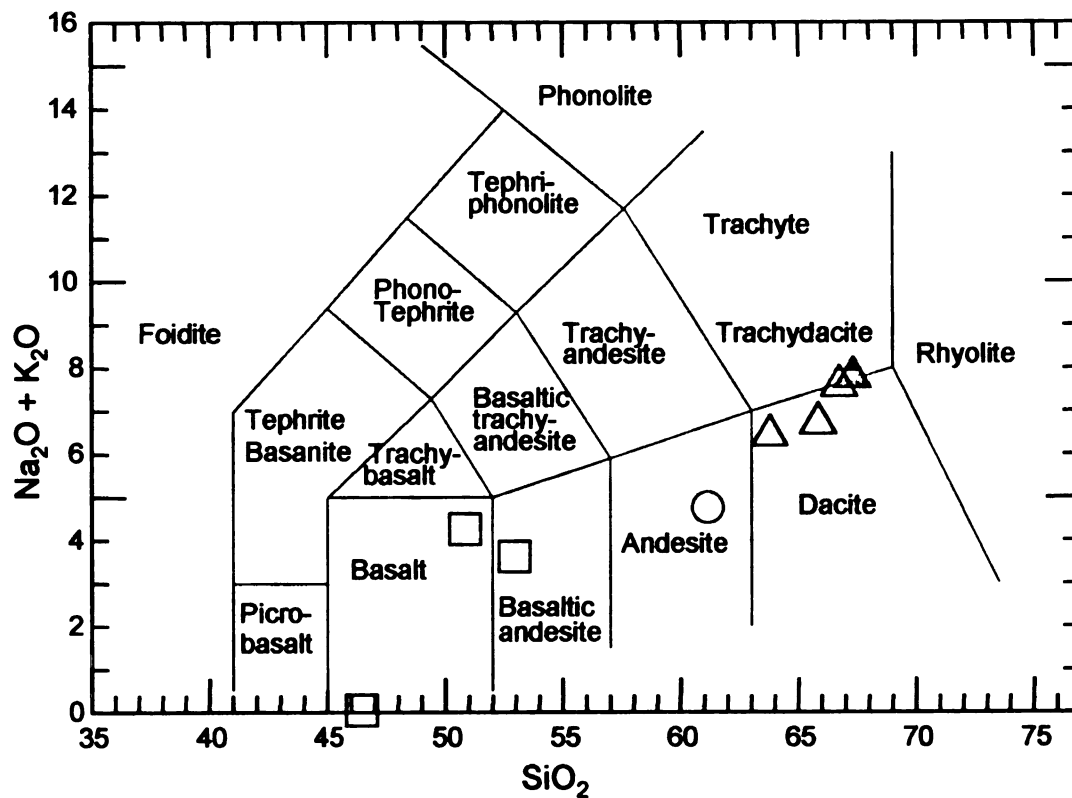


**Figure 45.** Classification diagram for the eight samples analyzed by XRD. Squares represent samples from unit Qtap, the circle is from unit Qas, and the triangles are from unit Qtapg. The filled symbol represents a core, and open symbols represent rinds or exfoliated corestone shells.

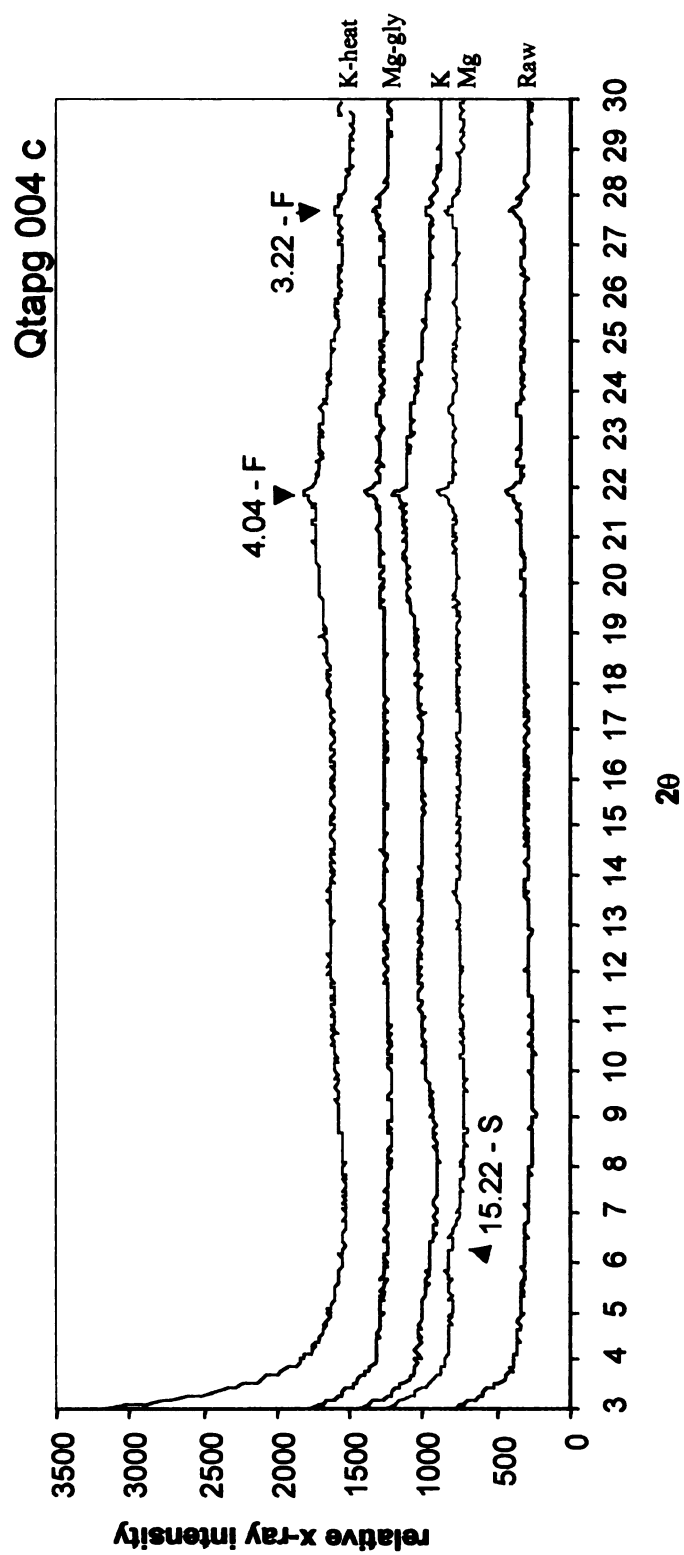


**Figure 46.** XRD pattern for the core of Qtapg 004. Smectite (S) is present in the Mg- and Mg-gly-scans, while feldspar (F) peaks are present in all scans. Number labels indicate d-spacing.



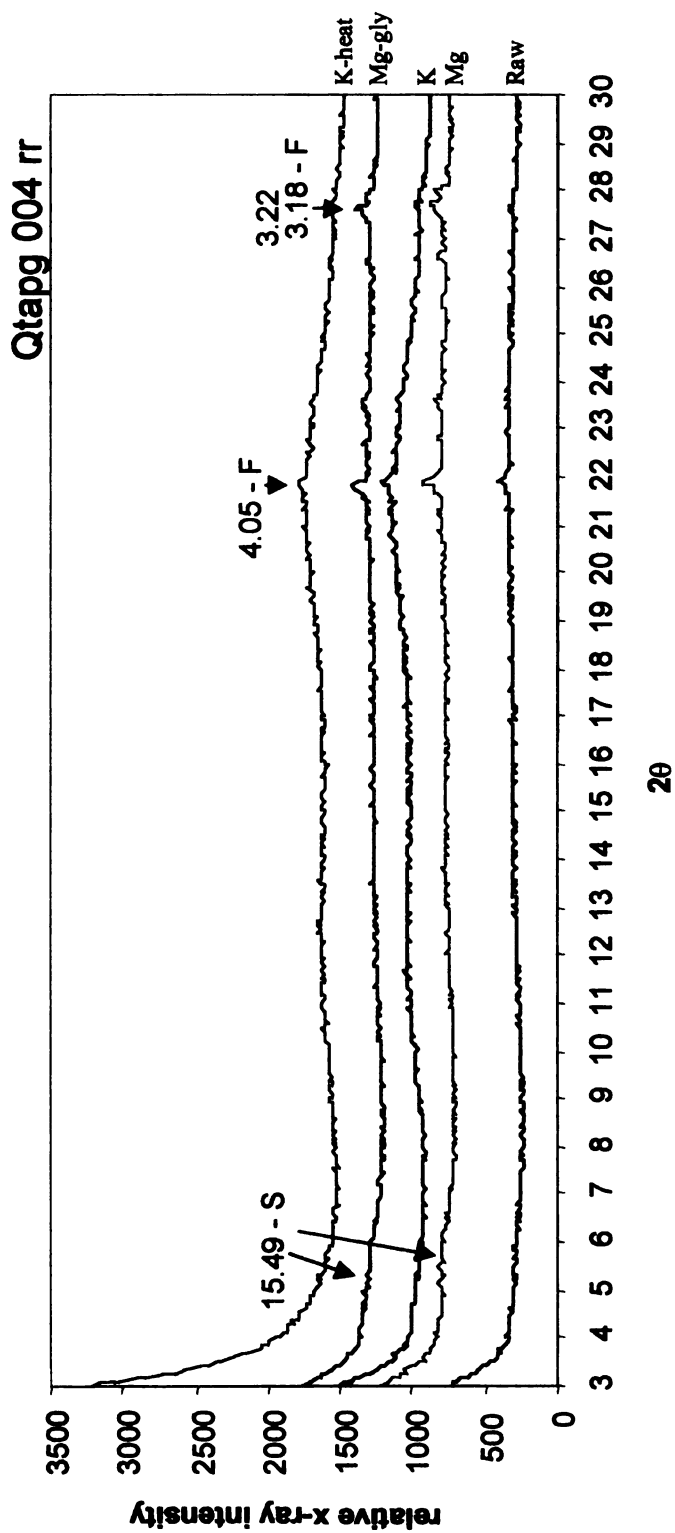
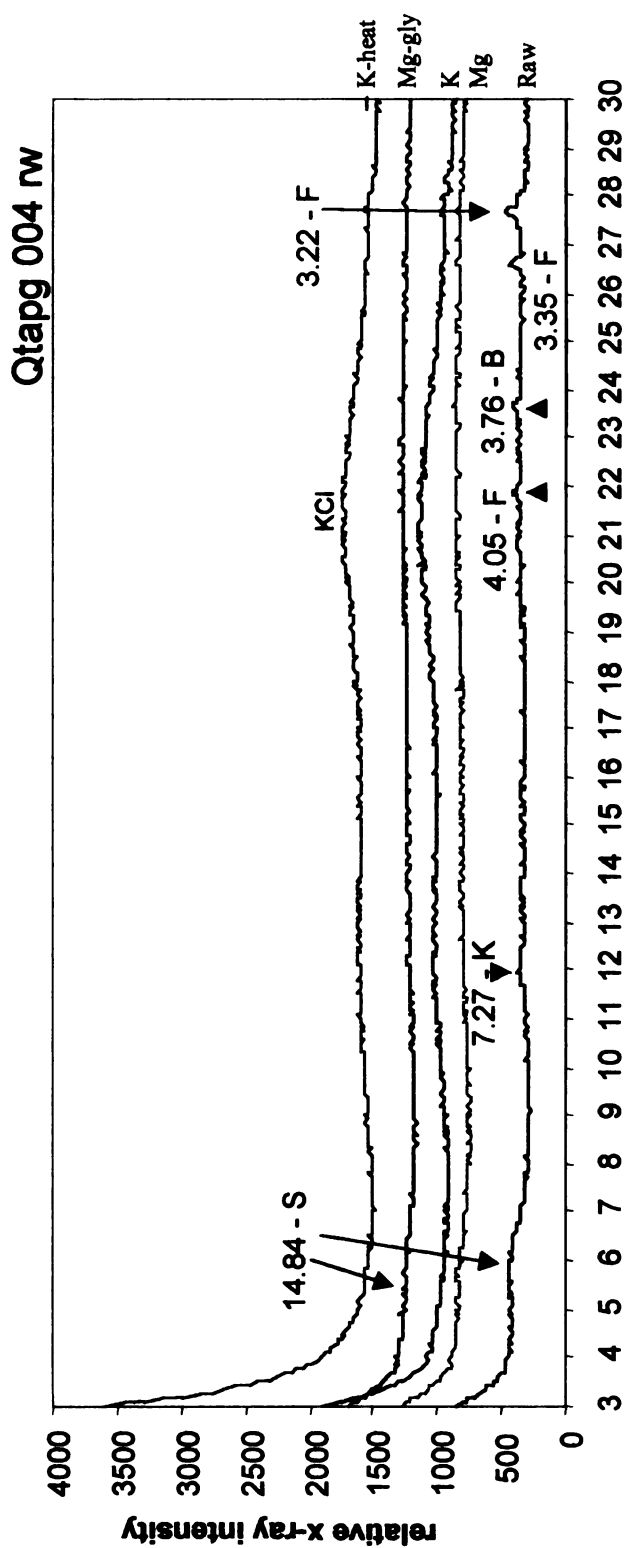
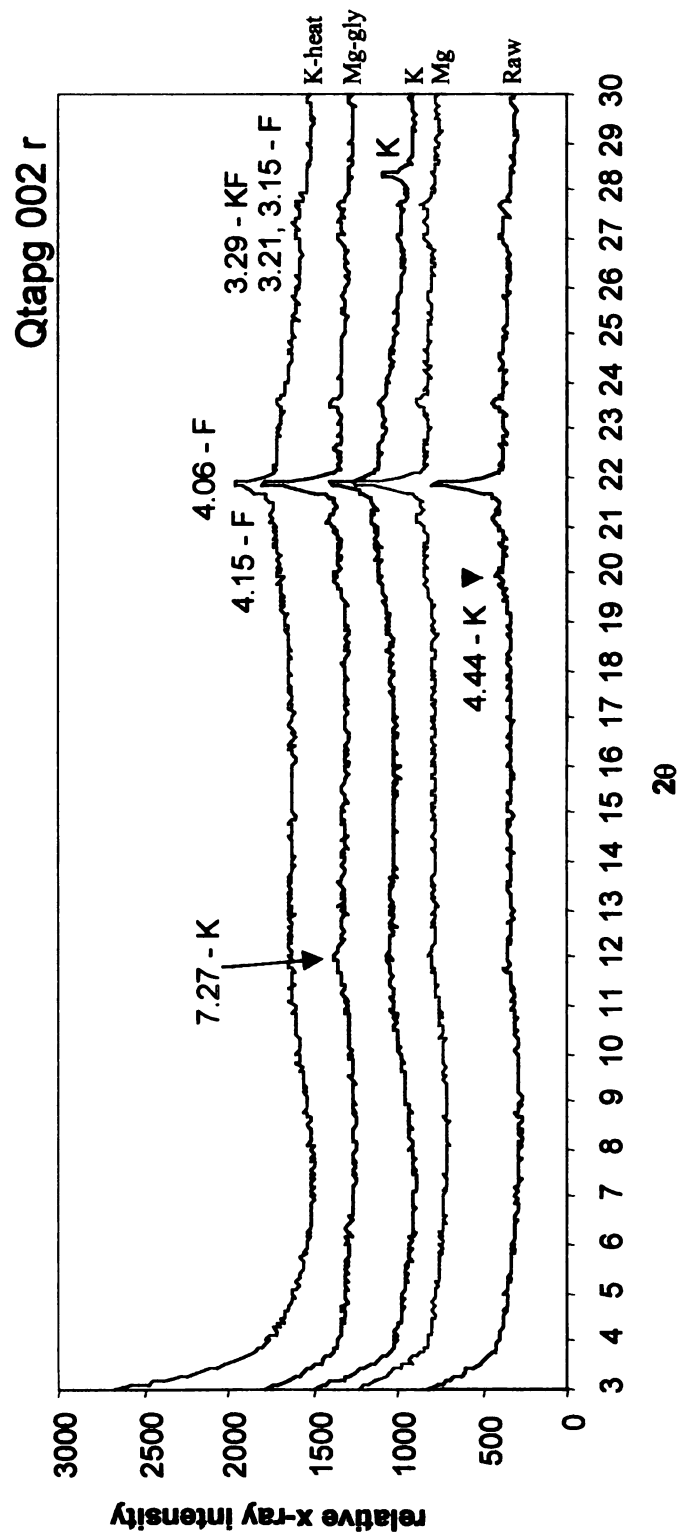


**Figure 47.** XRD pattern for the red rind of Qtapg 004. Smectite (S) is present in the Mg- and Mg-gly scans, while feldspar peaks (F) are present in all scans. Number labels indicate d-spacing.

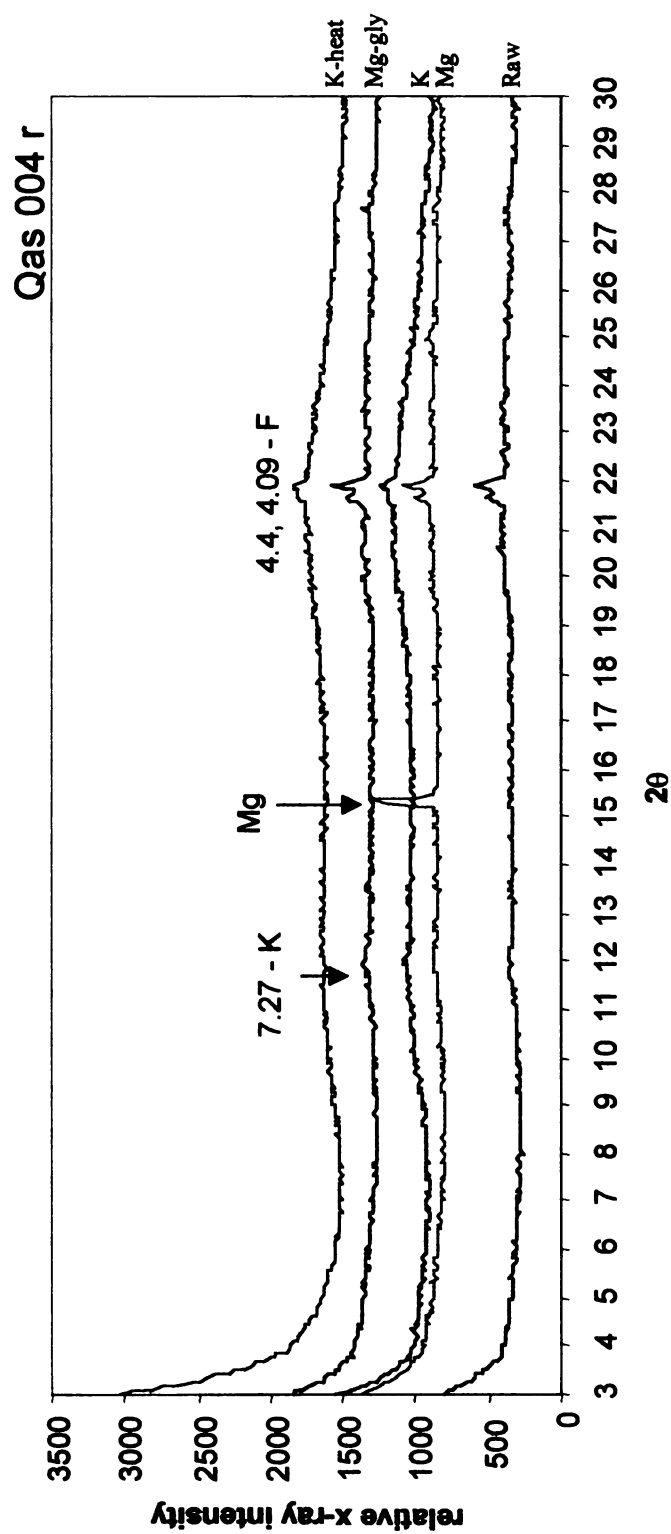


20

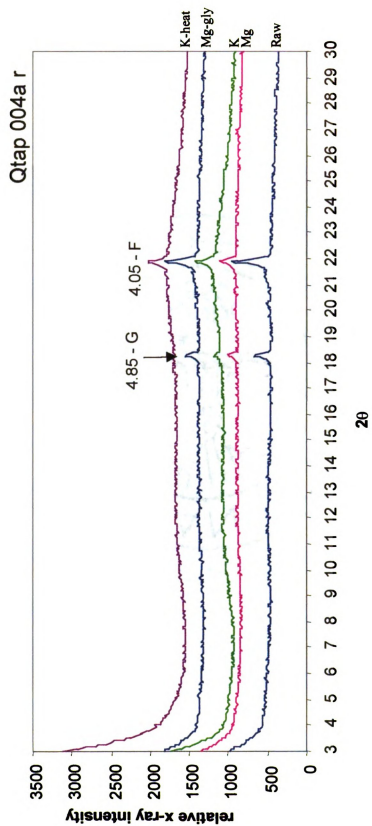
**Figure 48.** XRD pattern for the white rind of Qtapg 004. Smectite (S) is present in the Mg- and Mg-gly-scans. Kaolinite (K), feldspar (F), and possibly barite (B) peaks are present in the Raw scan. In both of the K-treated samples, the broad peak is most likely a consequence of KCl-saturation. Number labels indicate d-spacing.



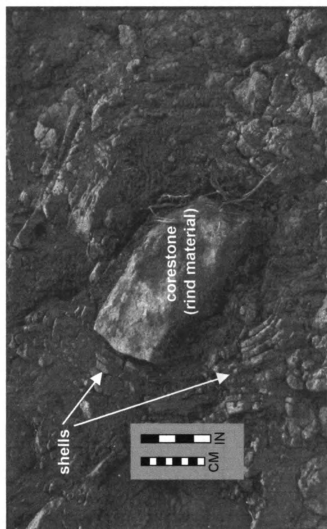
**Figure 49.** XRD pattern for the rind of Qtapg 002. Kaolinite (K) is present in all but the heated scan, while feldspar (F) (possibly including potassium feldspar (KF)) is present in all scans. The peak labeled 'K' is most likely a saturation effect from the K-saturating solution. Number labels indicate d-spacing.



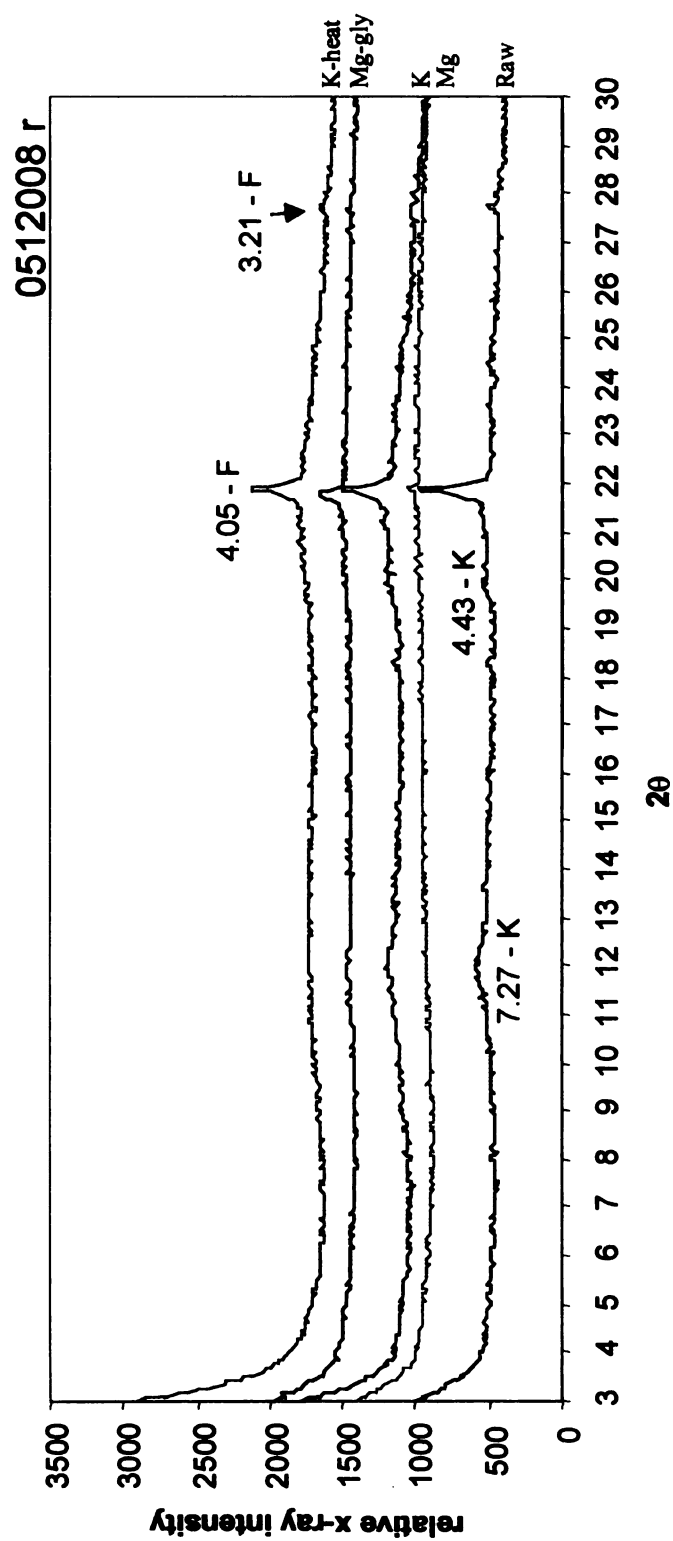
**Figure 50.** XRD pattern for the rind of Qas 004. Kaolinite (K) is present, as well as feldspar (F). The peak labeled 'Mg' is most likely an effect of the Mg-saturating solution. Number labels indicate d-spacing.



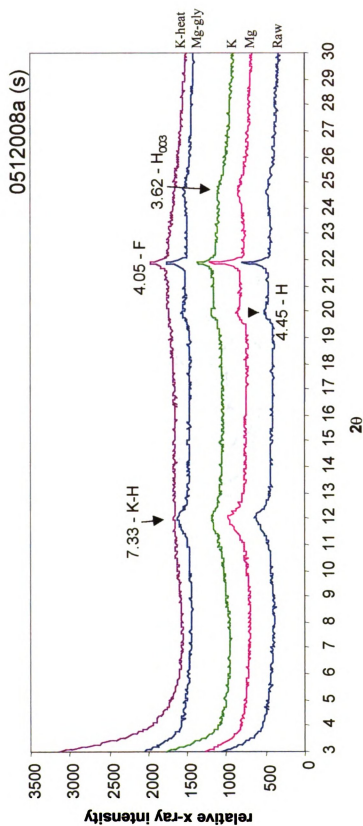
**Figure 51.** XRD pattern for the rind of Qtap 004a. Gibbsite (G) is present in all but the heated scan, while feldspar (F) is present in all scans. Number labels indicate d-spacing.



**Figure 52.** Field photograph of the in-situ corestone 0512008, from map unit Q1ap. The rind of the corestone, as well as the spheroidally exfoliated layers ('shells') surrounding the corestone were analyzed. XRD scans and SEM images follow in figures 53-56.

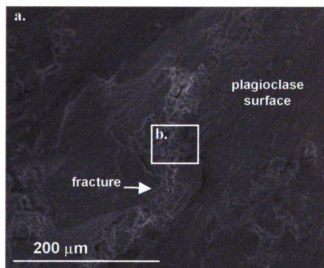


**Figure 53.** XRD pattern for the rind of 0512008. Kaolinite (K) is present in the raw and K-saturated samples, while feldspar (F) is present in all samples. Number labels indicate d-spacing.

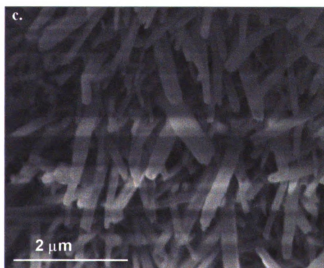
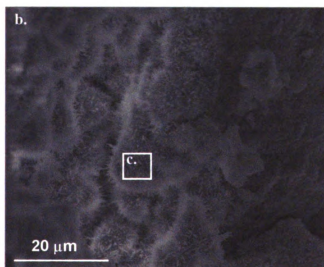


**Figure 54.** XRD pattern for the rind of 0512008. Kaolinite (K) and/or halloysite (H) are present in all but the K-heated sample, while feldspar (F) is present in all samples. Number labels indicate d-spacing.





**Figure 55.**  
Secondary-electron image of a fracture on the surface of a plagioclase phenocryst from 0512008 core (a) contains aggregates (b) of Halloysite rods (c).



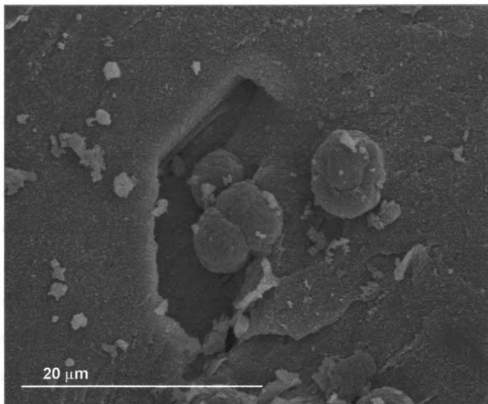


**Figure 56.** Secondary-electron image of an etch pit on the surface of a plagioclase phenocryst from the rind of corestone 0512008. Note the round halloysite balls that are in and around the pit (e.g. Robertson and Eggleton, 1991).

## **Scanning Electron Microscopy – Energy Dispersive Spectra (SEM-EDS)**

Twenty-one polished, carbon-coated thin sections were examined at MSU on a JEOL JSM-6400V scanning microscope at 20 kV, at a working distance of 16 mm and condenser lens setting at approximately 14, depending on the operating conditions. Backscattered-electron imaging (BSI) and energy-dispersive spectra (EDS) were used to analyze and identify primary minerals and their secondary products. Images and spectra are found at the end of this chapter.

In most core and rind samples, from all units, weathering and/or hydrothermal alteration features are observed. For example, in the rind of Qas 004, secondary clays fill a sawtooth-edged fracture in a pyroxene (figure 57). While clays are a common secondary product in almost all samples analyzed, other secondary products can be grouped into three categories: 1) barium-bearing sulfates such as barite ( $\text{Ba}(\text{SO}_4)$ ), 2) hollandite ( $\text{BaMn}_5\text{Si}_2\text{O}_{16} \cdot 3\text{H}_2\text{O}$ ), and 3) at least 3 different REE-P bearing phases.

Six samples from Qtap, the oldest unit, were analyzed, nine samples from Qtapg, and six samples from Qas, the youngest unit. The cores of Qas 001a and 003, and the intermediate sample of 003 contain clean apatite inclusions in Fe-Ti oxides and pyroxene phenocrysts (figure 58). No apatite was found in the rind of Qas 003, and most phenocrysts have weathered to boxwork structures. However, a Sr-bearing barite is present, associated with small plagioclase phenocrysts (figure 59). The presence of this sometimes hydrothermal mineral implies that this sample may have been exposed to some amount of hydrothermal fluid, and not merely meteoric water (Hanor, 2000). Barite is also abundant in intermediate and rind samples from unit Qtapg (figures 60 and

61). The intermediate zone of Qtapg 001, as well as the white and red rinds of Qtapg 004 contain hollandite (e.g. figure 62). Sample 005 rck contains a 2.5 mm wide crevice described previously in the Petrography section (figure 33, *Petrography*). EDS data show that the material filling the majority of the crevice is clay, while an approximately 10 $\mu$ m-thick layer of a P-Ba-Mn-phase lines the crevice surface. This could be evidence stagnant fluid collection in the crevice that altered the surfaces of the crevice over time (figure 63).

Even though apatite is absent from most of the analyzed samples, different secondary REE-P phases are present in a number of samples. They are associated with either plagioclase, potassium feldspar, or pyroxene phenocrysts. Clay is often, but not always, the immediate host of the REE-P-phase within the primary phenocrysts. The spectra described below have a range of P-Al and P-Si ratios. These ratios are most likely artifacts of excitation by the X-ray of surrounding Al and Si in clays or phenocrysts. However, until microprobe data is available, it remains unclear how much Al and Si are present in the secondary REE-P-phase.

In the core of Qas 004, the rind of Qtap 003, and the core of 0512008, a corestone collected near Qtap 003, LREE-phosphates are present (figure 64). They each contain La and Nd, as well as other REE which vary among samples. The REE-phases in Qas 004 c are associated with plagioclase, while the phase in Qtap 003 r is associated with clay within a highly weathered plagioclase. The LREE-phosphate in the rind of Qtapg 001 is notable because this phase, hosted by clay within a clinopyroxene, contains sulfur and potassium in addition to La, Pr, and Nd (figure 65).

In the core of Qtapg 0012, and both the core and rind of 0512008, HREE-phosphates are present (figure 66). All are associated with plagioclase, although the phase from 0512008r is also associated with clay within the weathered phenocryst.

In the rind of Qtapg 002, at least two REE-phases are present, associated with voids and clay left from a weathered plagioclase (figure 67). One REE-phase contains mainly LREE, while the other contains La, Nd, Dy, Er, and Yb. In the rind of Qas 004, an REE-phosphate is present among clay within a potassium feldspar (figure 68).

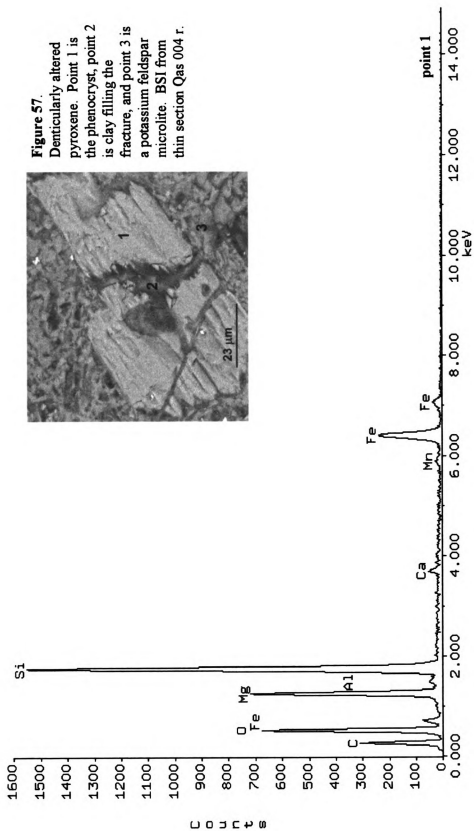
LREE-phases are present in both the core and red rind of Qtapg 004. The phase in the core is sometimes associated with an Fe-clay pseudomorph (figure 69). The phase in the red rind is sometimes associated with a potassium feldspar, and is the one of the only REE-phases observed in these samples to contain K (figure 70). It is interesting to note that in the white rind of Qtapg 004, the secondary P-phase is devoid of REE, and associated with Fe-clay (figure 76). In both the core and rind of Qtap 003, REE-phases with high concentration of HREE are associated with clay, and plagioclase phenocrysts (figure 72).

Two samples have REE-phases with possibly high Al and Si concentrations relative to P, but again, these phases are very small and spectra may be influenced by the excitation of surrounding Al and Si. In the rind of 0512008 (crr), the REE-phase is rich in Al and Si, but they do not exceed P (figure 73). The phase is associated with clay within a highly weathered plagioclase. In the intermediate zone of 0512008, an REE-phase is present with possibly high concentrations of Al and Si relative to P (figure 74).

To summarize, REE-P phases were found in the core and rind of Qas 004, the core and rind of Qtapg 001, the rind of Qtapg 002, the core and rind of Qtap 003 and the

core, intermediate, and rind of its related corestone, 0512008. The core and red rind of Qtapg 004 contain REE-P phases, while the white rind does not. Barite was found in the rind of Qas 003, and the intermediate zone and rind of Qtapg 001. Hollandite was found in the intermediate zone of Qtapg 001, and in the red and white rinds of Qtapg 004.

Weathering textures and clay minerals observed within phenocrysts in both petrographic and electron microscopes, as well as the presence of barite and REE-P phases suggests that these samples may have undergone weathering and alteration at a range of temperatures and conditions.



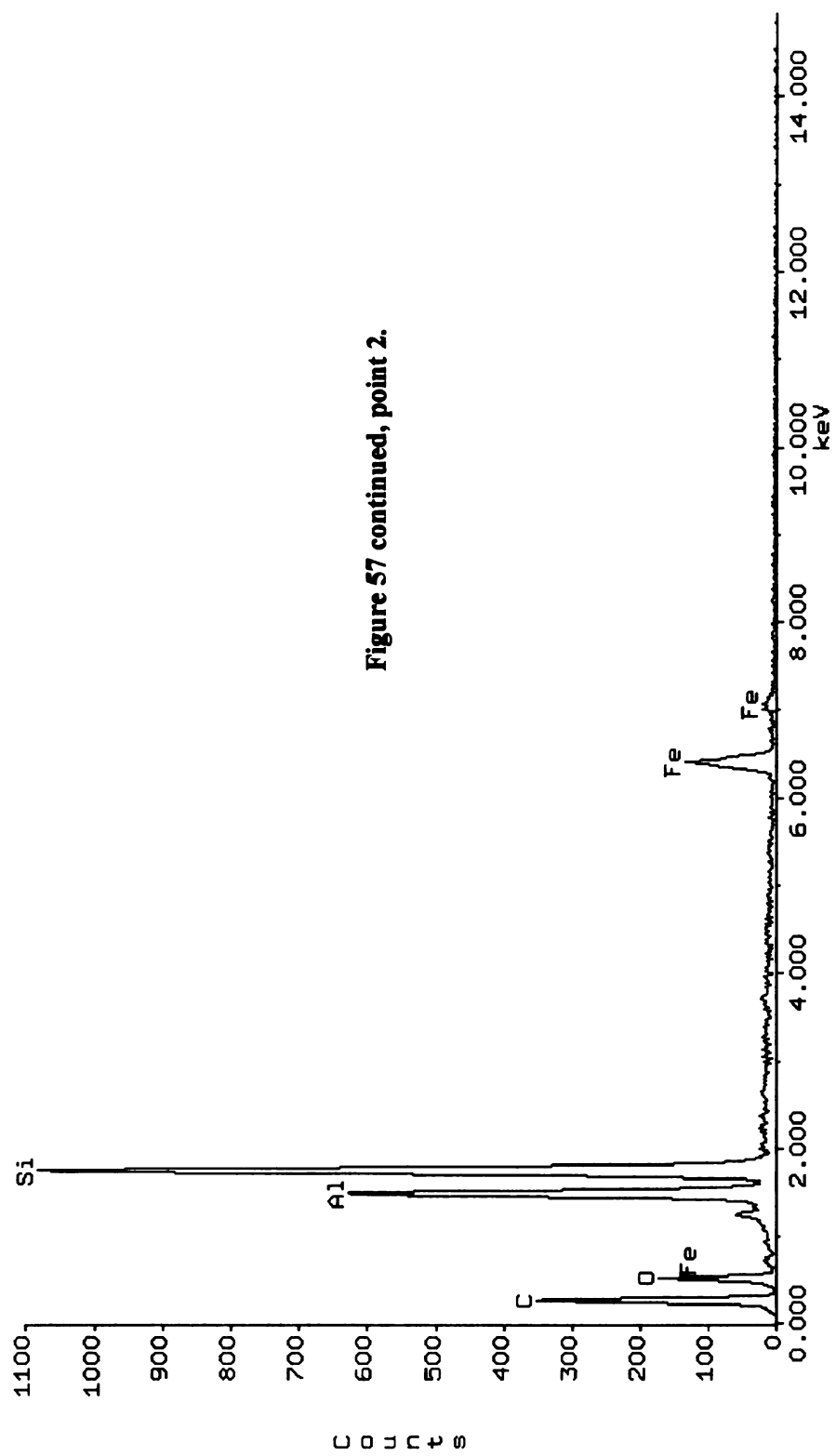


Figure 57 continued, point 2.



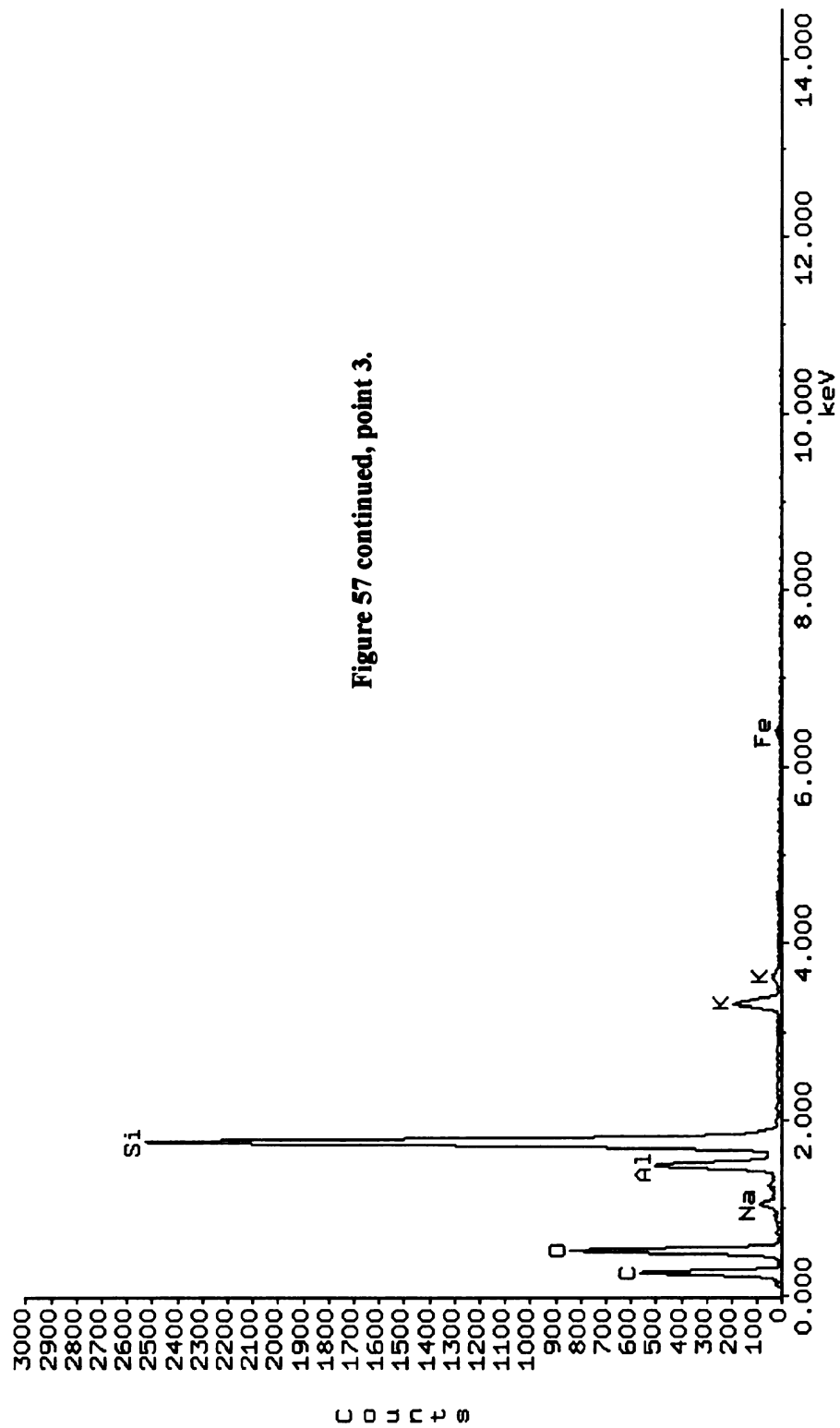
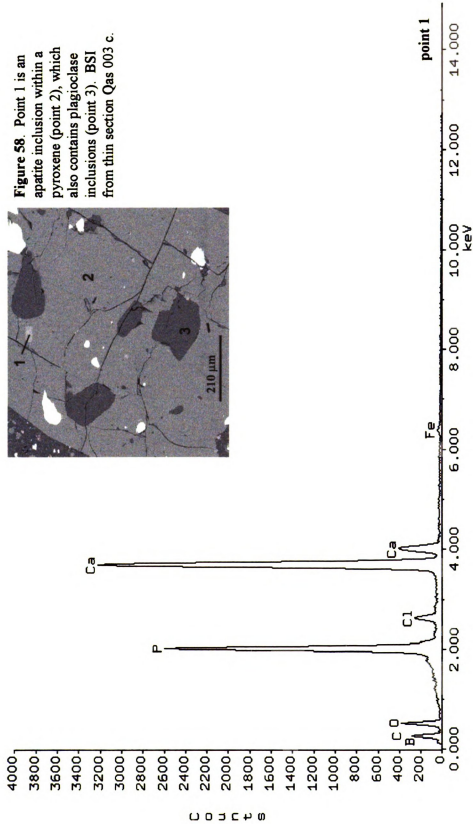


Figure 57 continued, point 3.



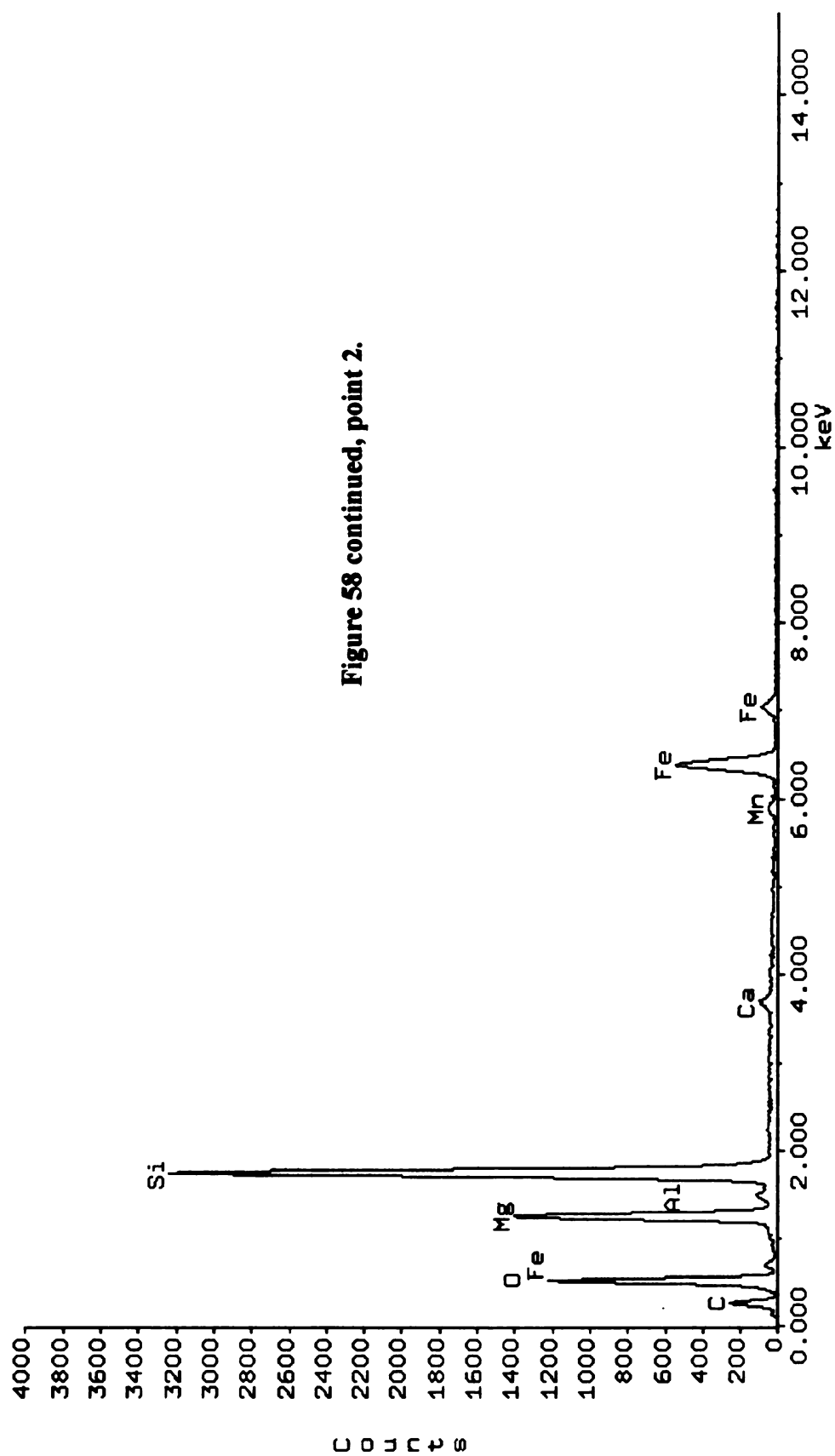
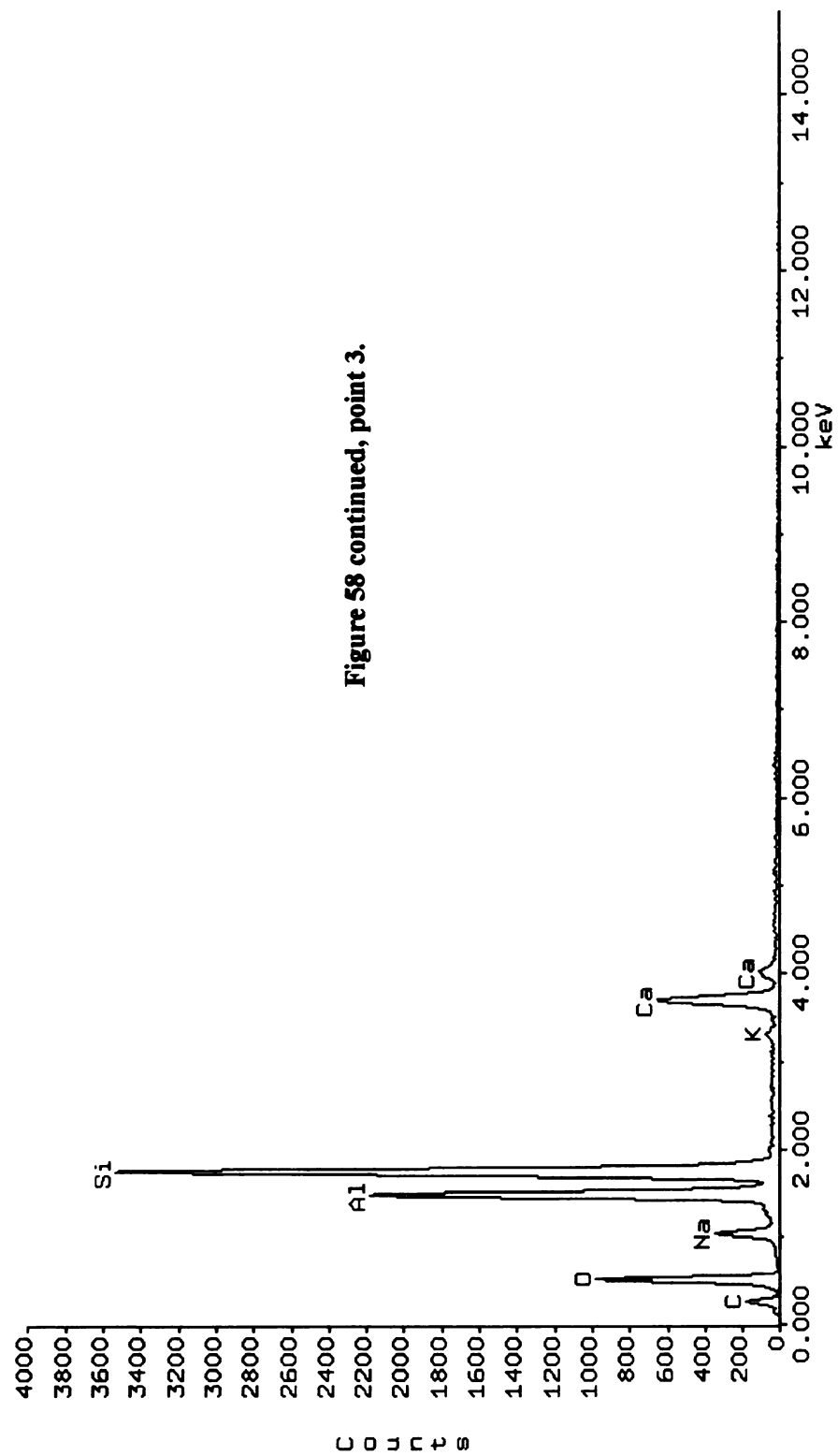


Figure 58 continued, point 2.



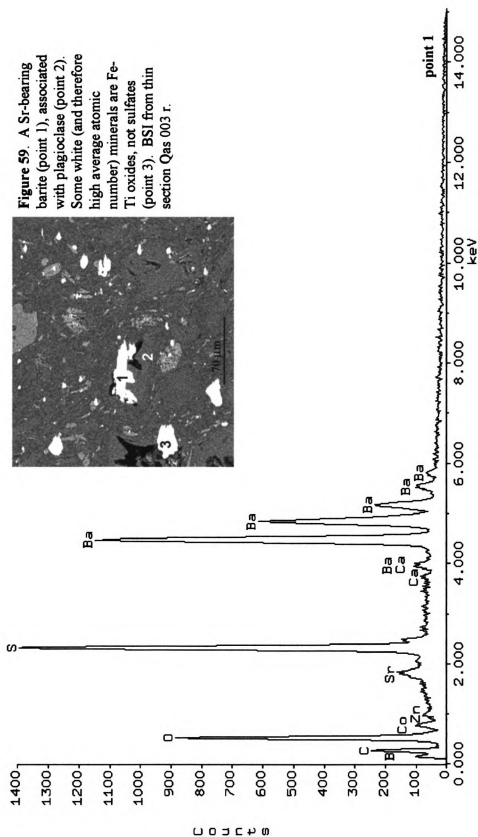


Figure 59. A Sr-bearing barite (point 1), associated with plagioclase (point 2). Some white (and therefore high average atomic number) minerals are Fe-Ti oxides, not sulfates (point 3). BSEI from thin section Qas 003 r.

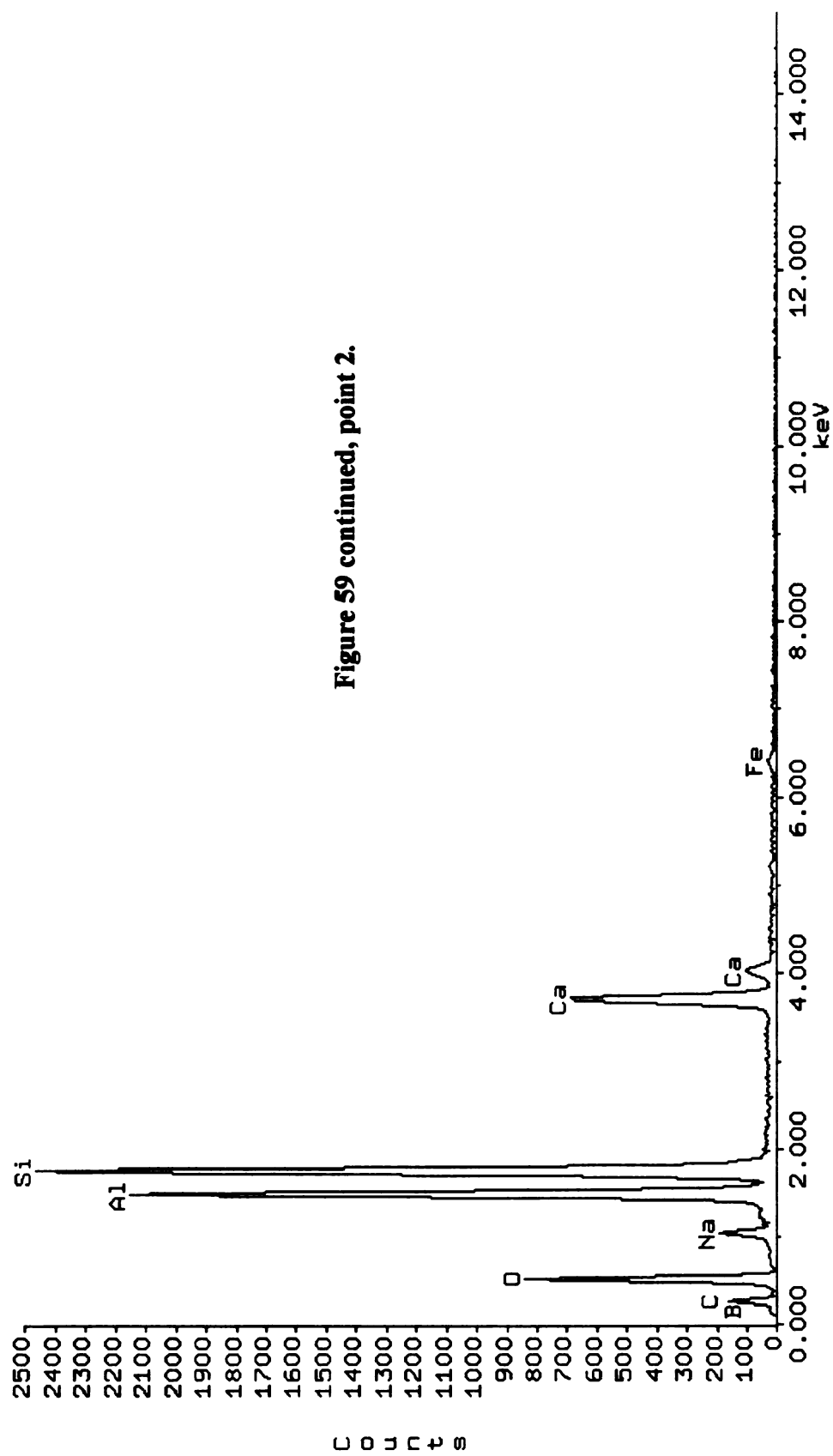
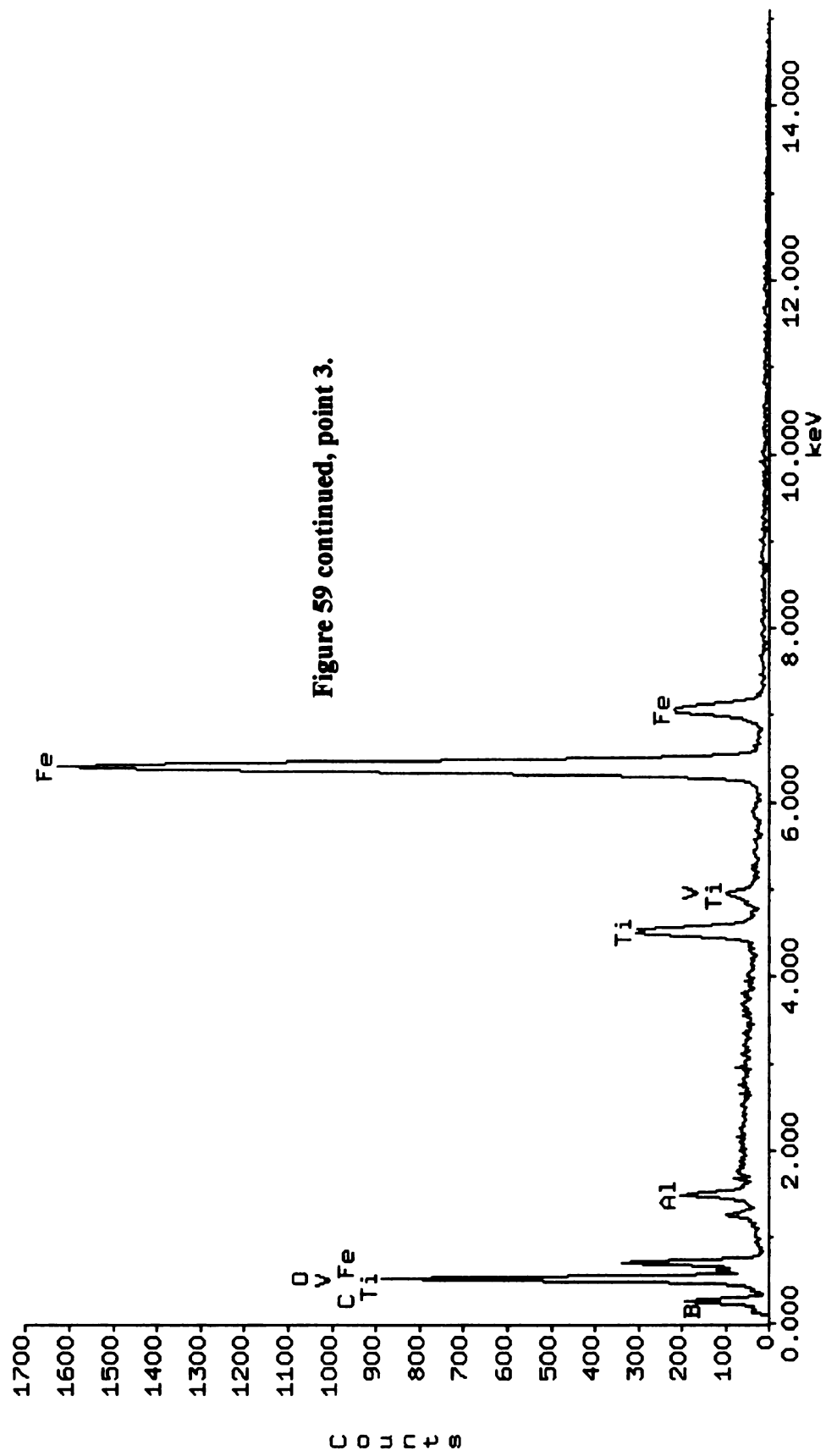
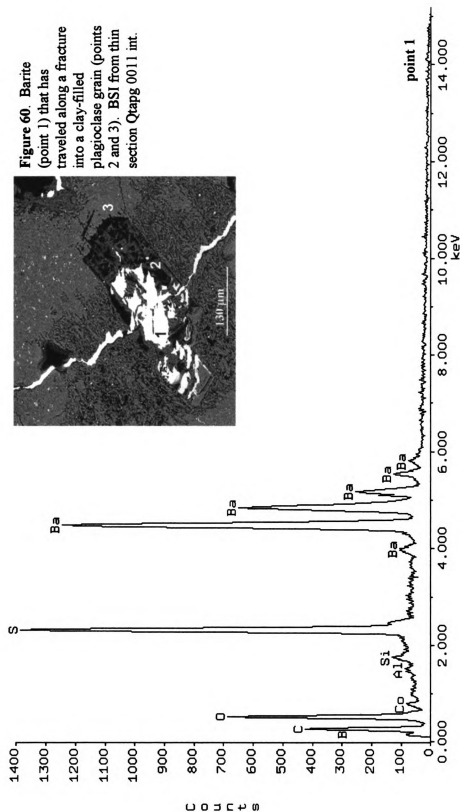


Figure 59 continued, point 2.





**Figure 60.** Barite (point 1) that has traveled along a fracture into a clay-filled plagioclase grain (points 2 and 3). BSI from thin section Qapag 0011 int.



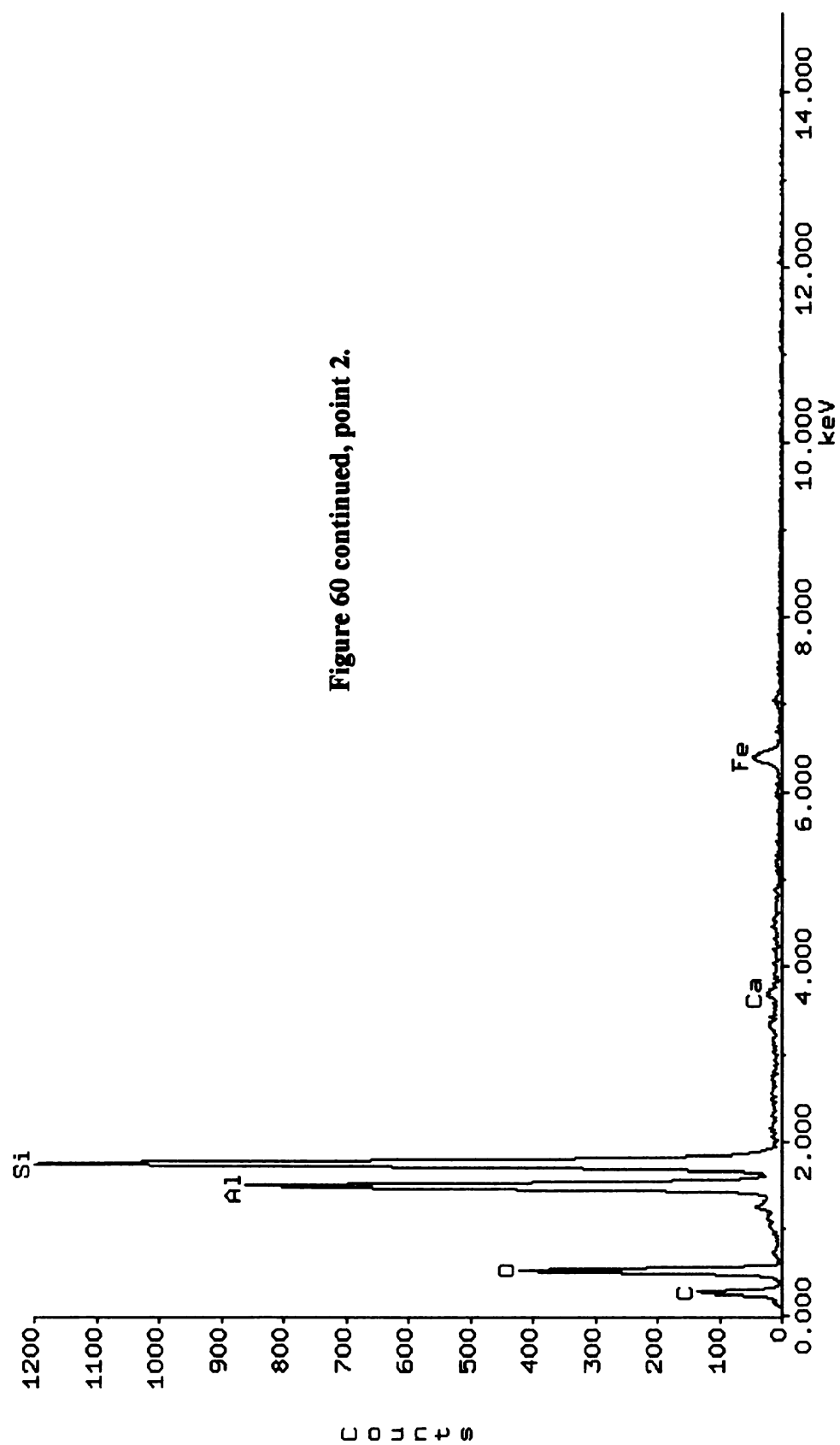


Figure 60 continued, point 2.

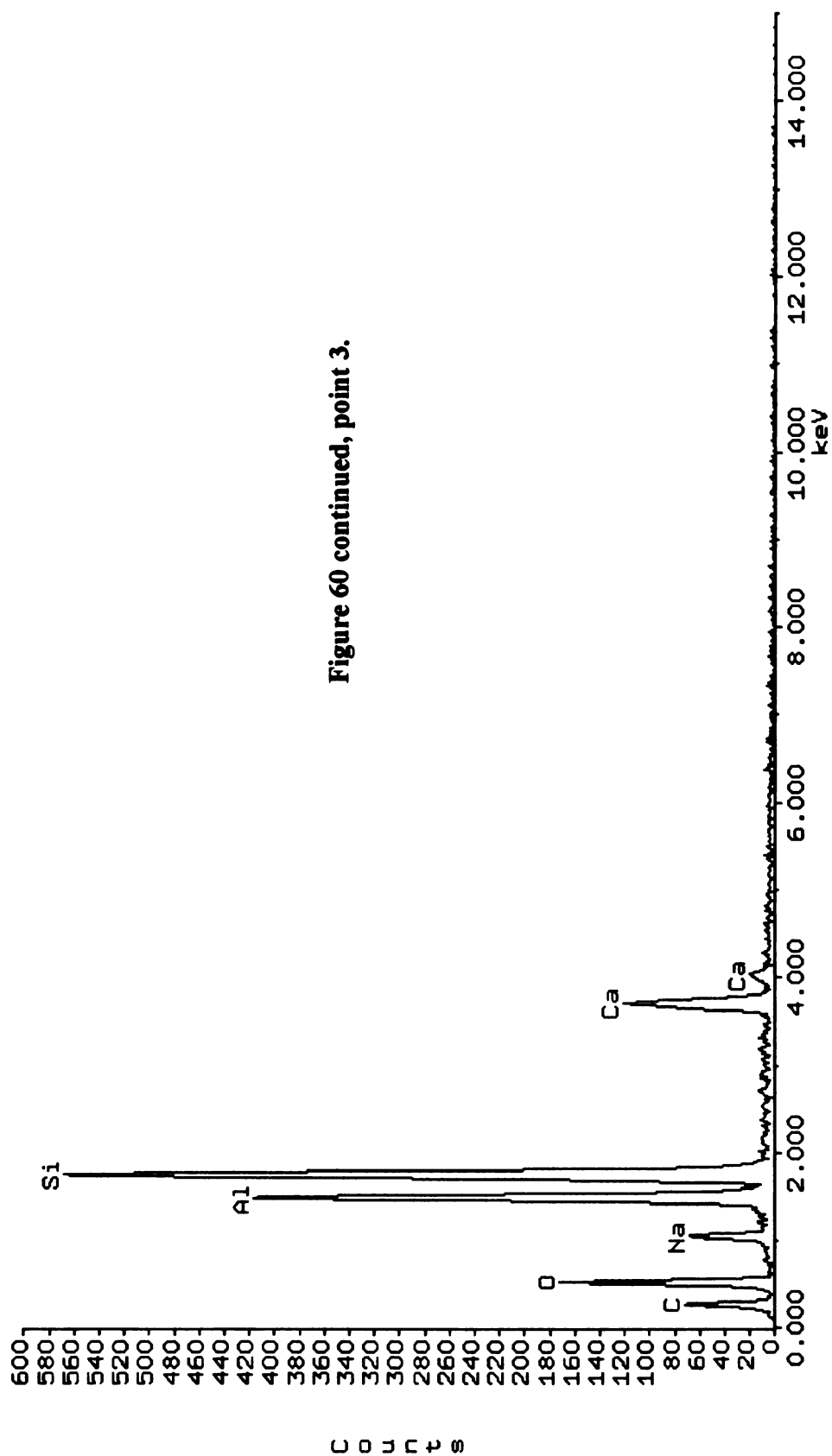


Figure 60 continued, point 3.



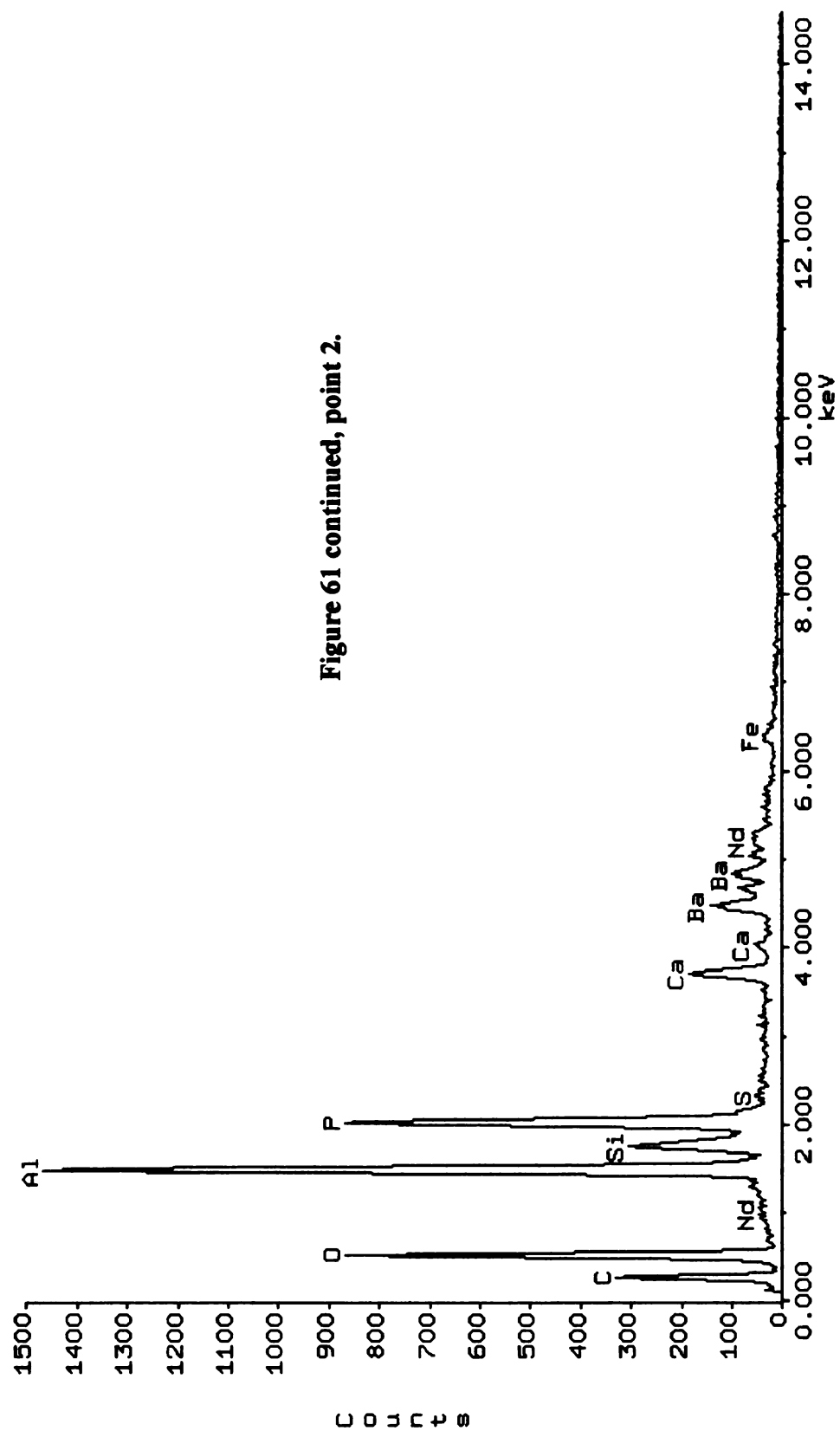


Figure 61 continued, point 2.

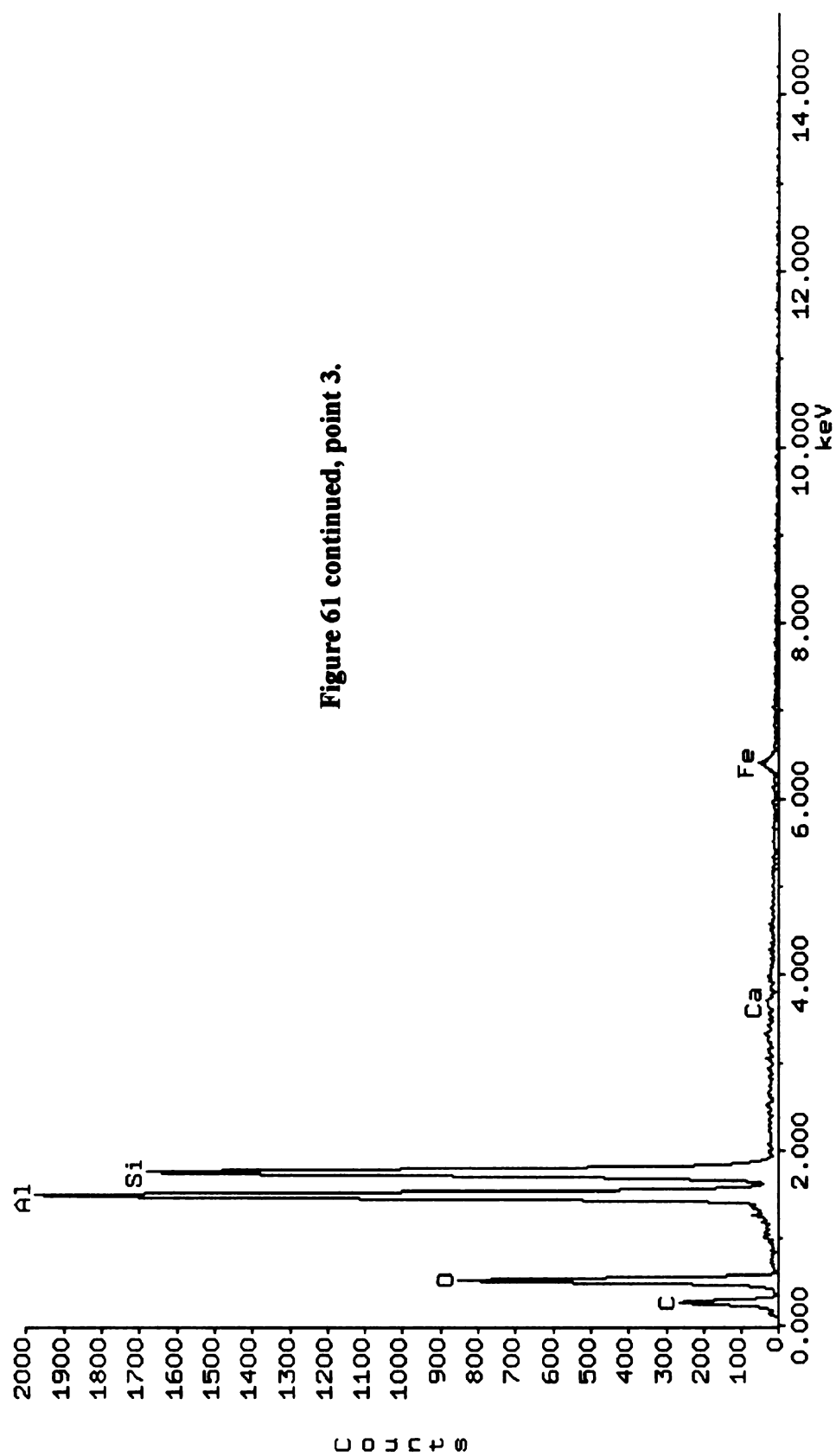


Figure 61 continued, point 3.

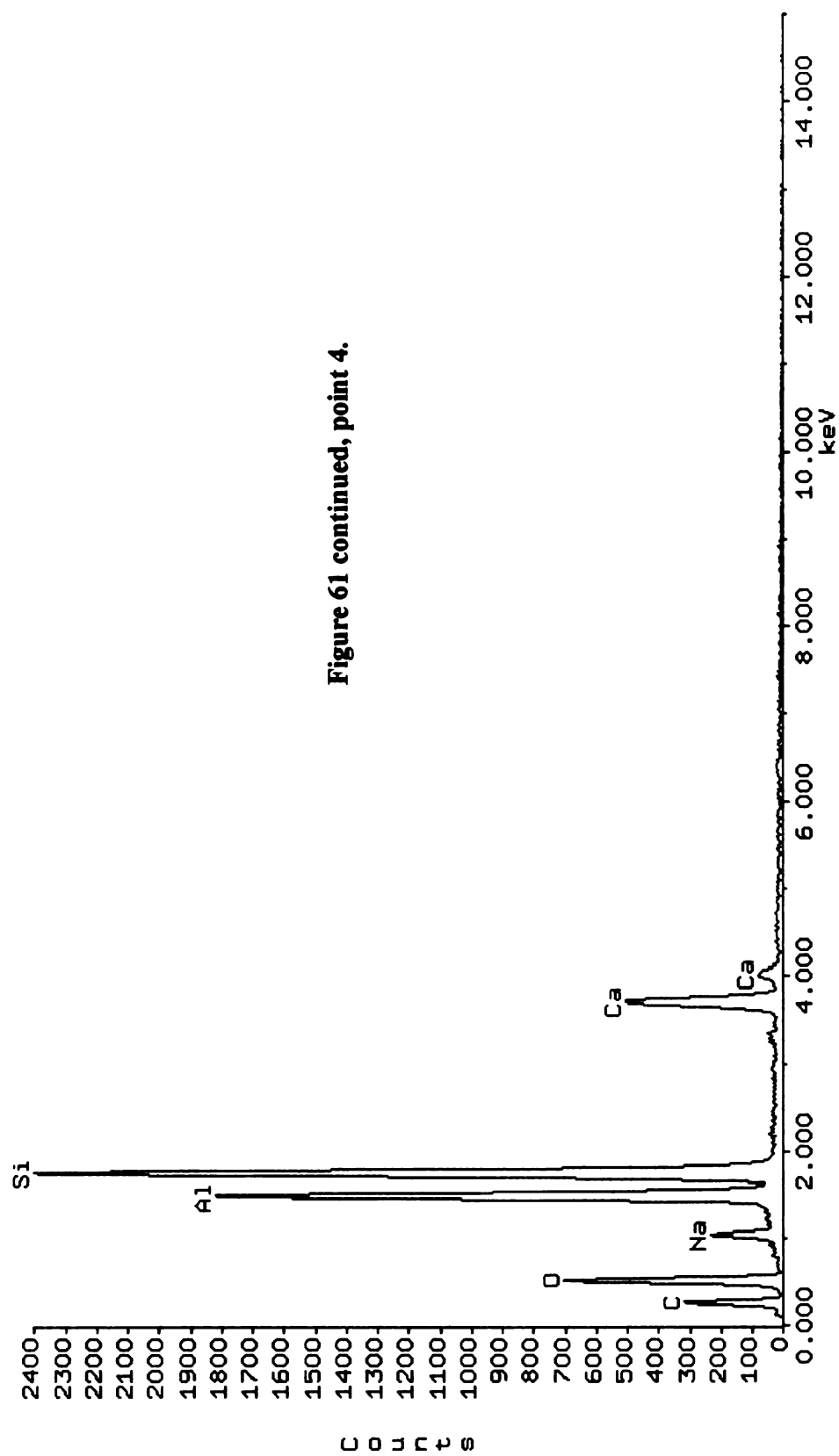
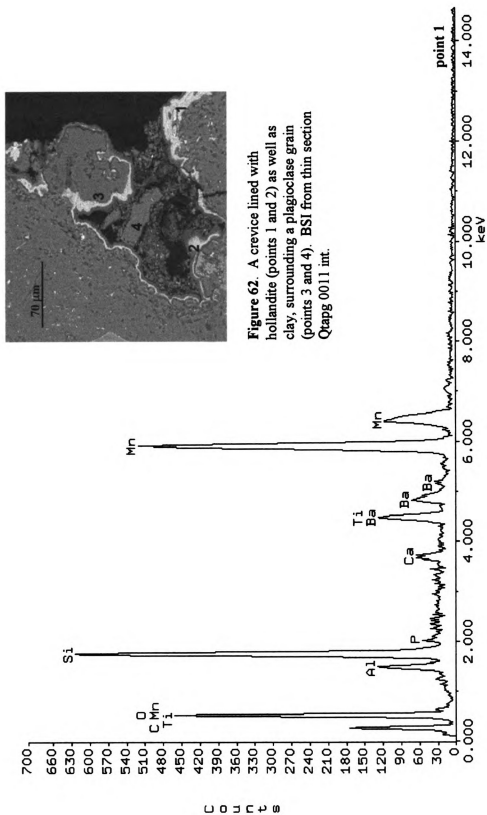


Figure 61 continued, point 4.



**Figure 62.** A crevice lined with hollandite (points 1 and 2) as well as clay, surrounding a plagioclase grain (points 3 and 4). BSEI from thin section Qtapg 0011 int.

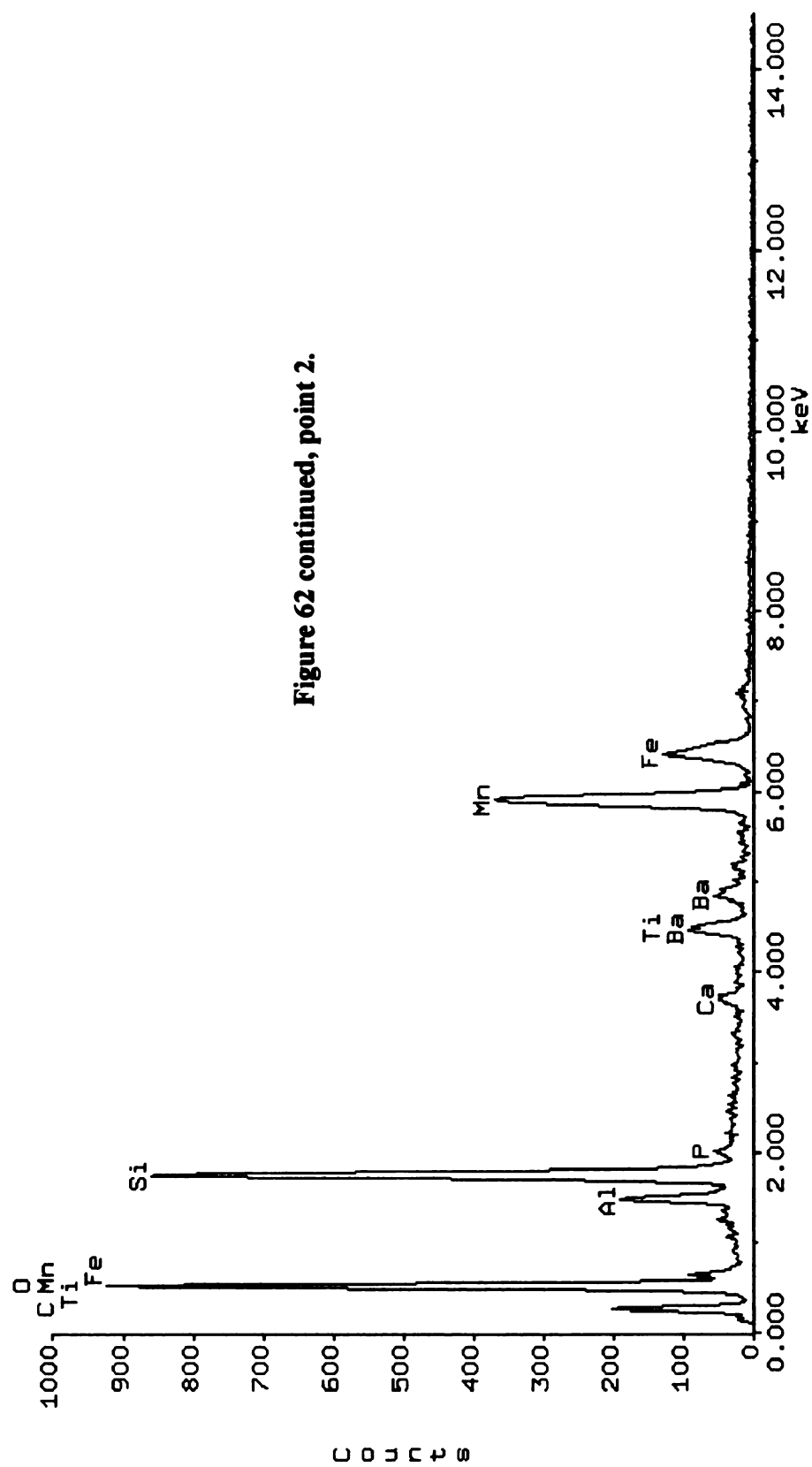


Figure 62 continued, point 2.



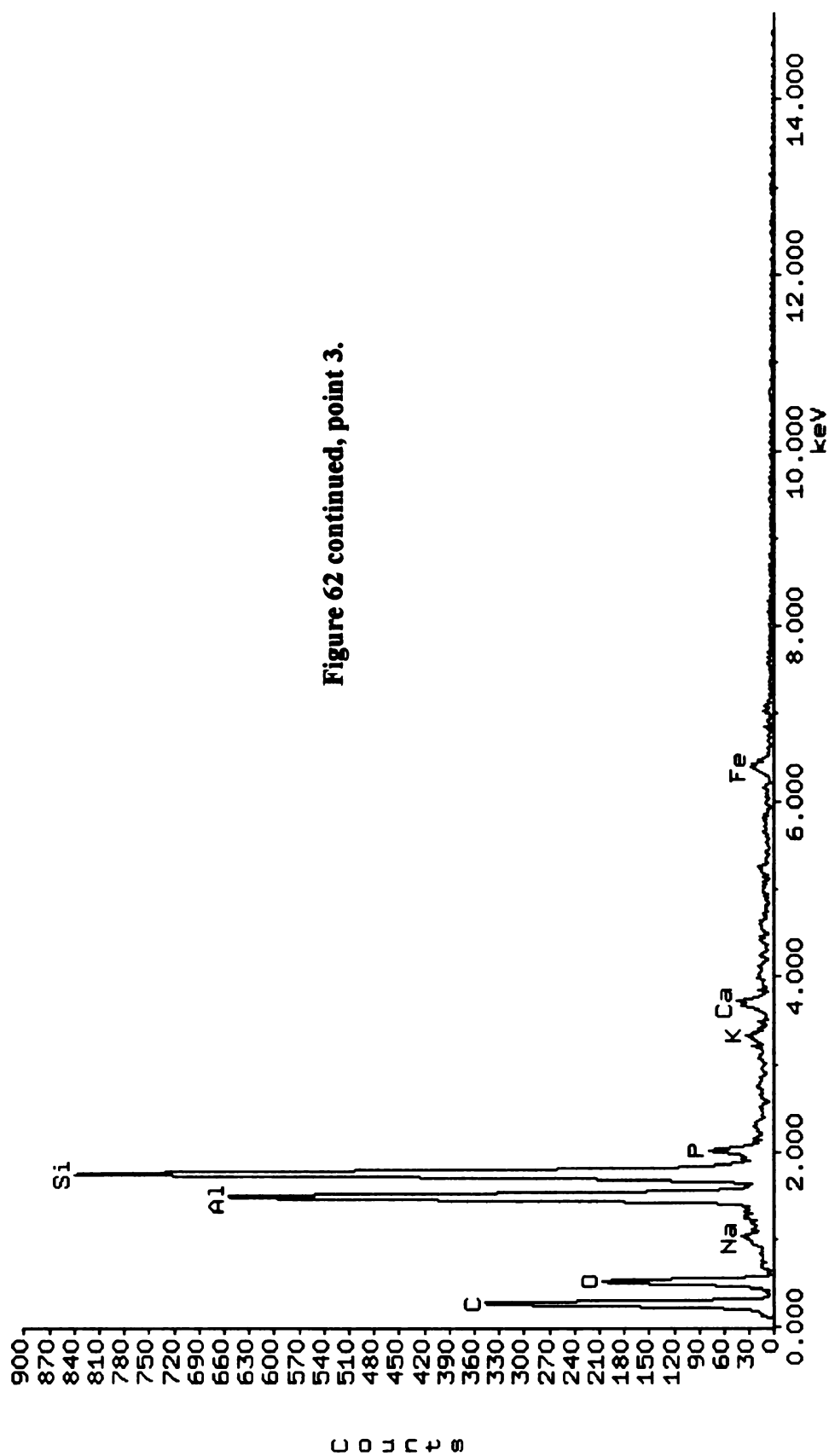
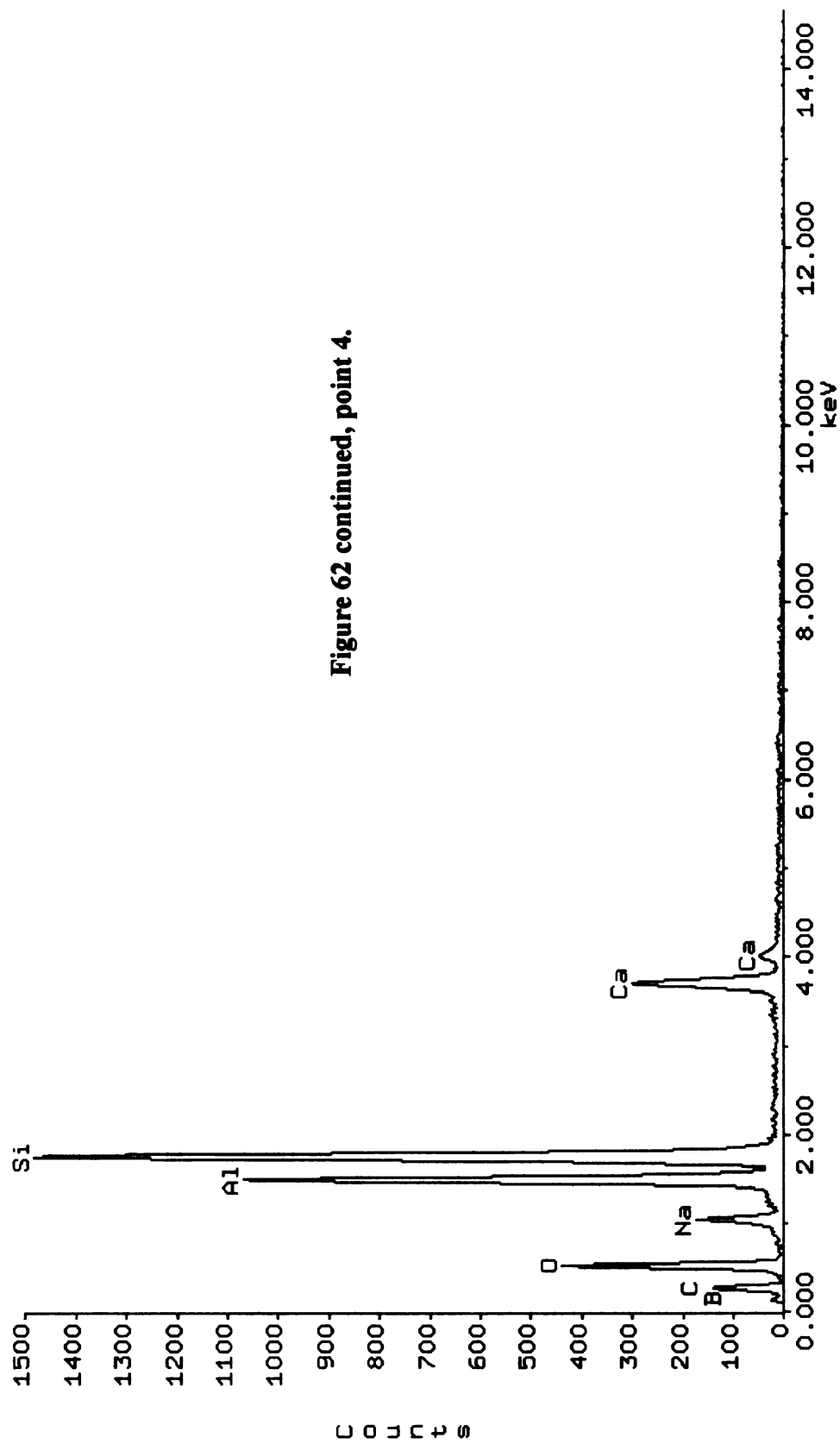
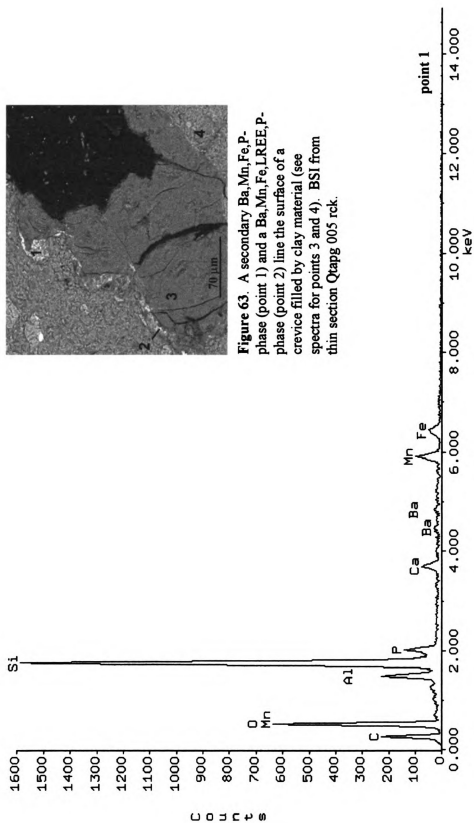
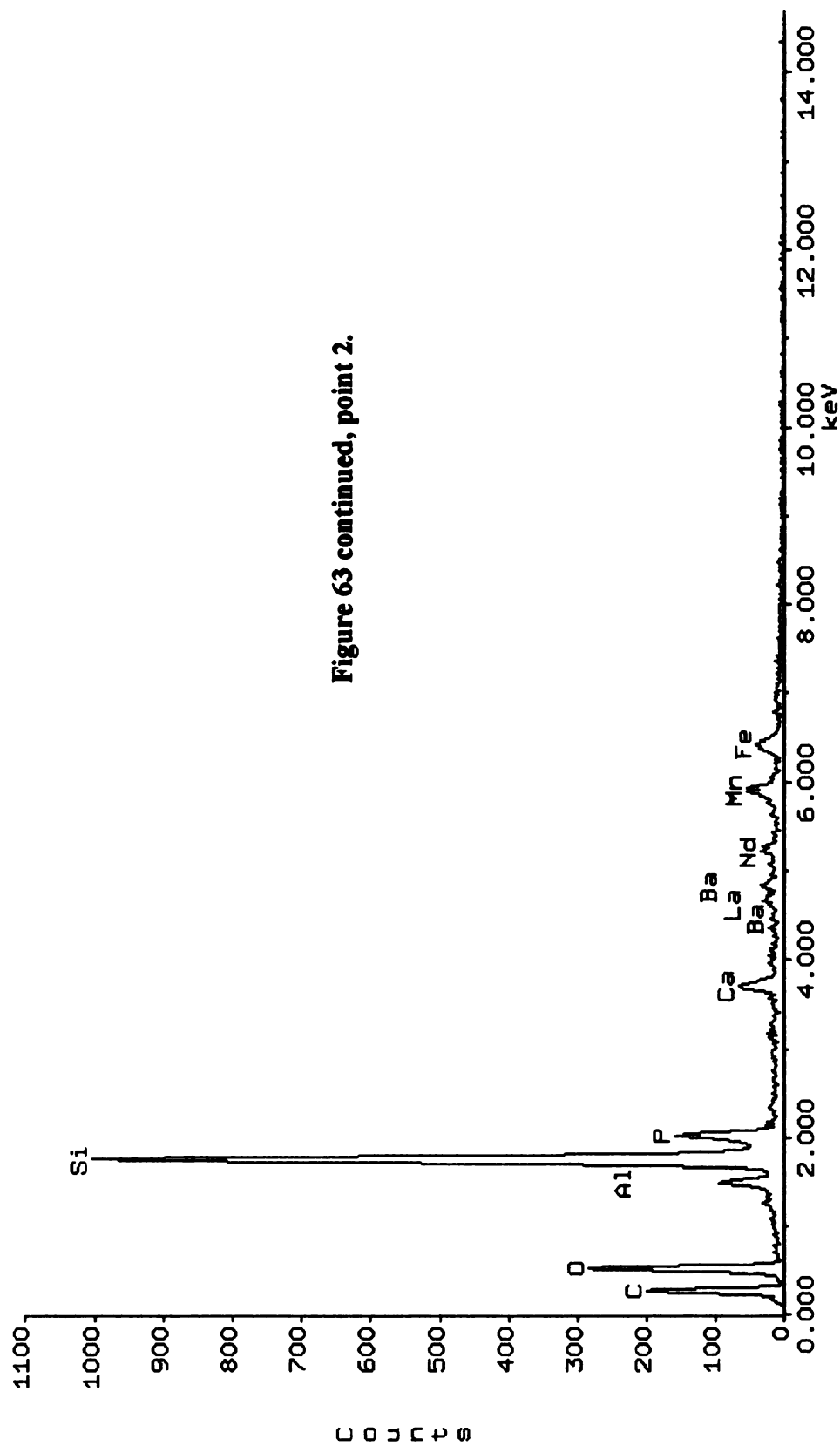


Figure 62 continued, point 3.





**Figure 63.** A secondary Ba, Mn, Fe, P-phase (point 1) and a Ba, Mn, Fe, LREE, P-phase (point 2) line the surface of a crevice filled by clay material (see spectra for points 3 and 4). BSI from thin section Qapg 005 rck.



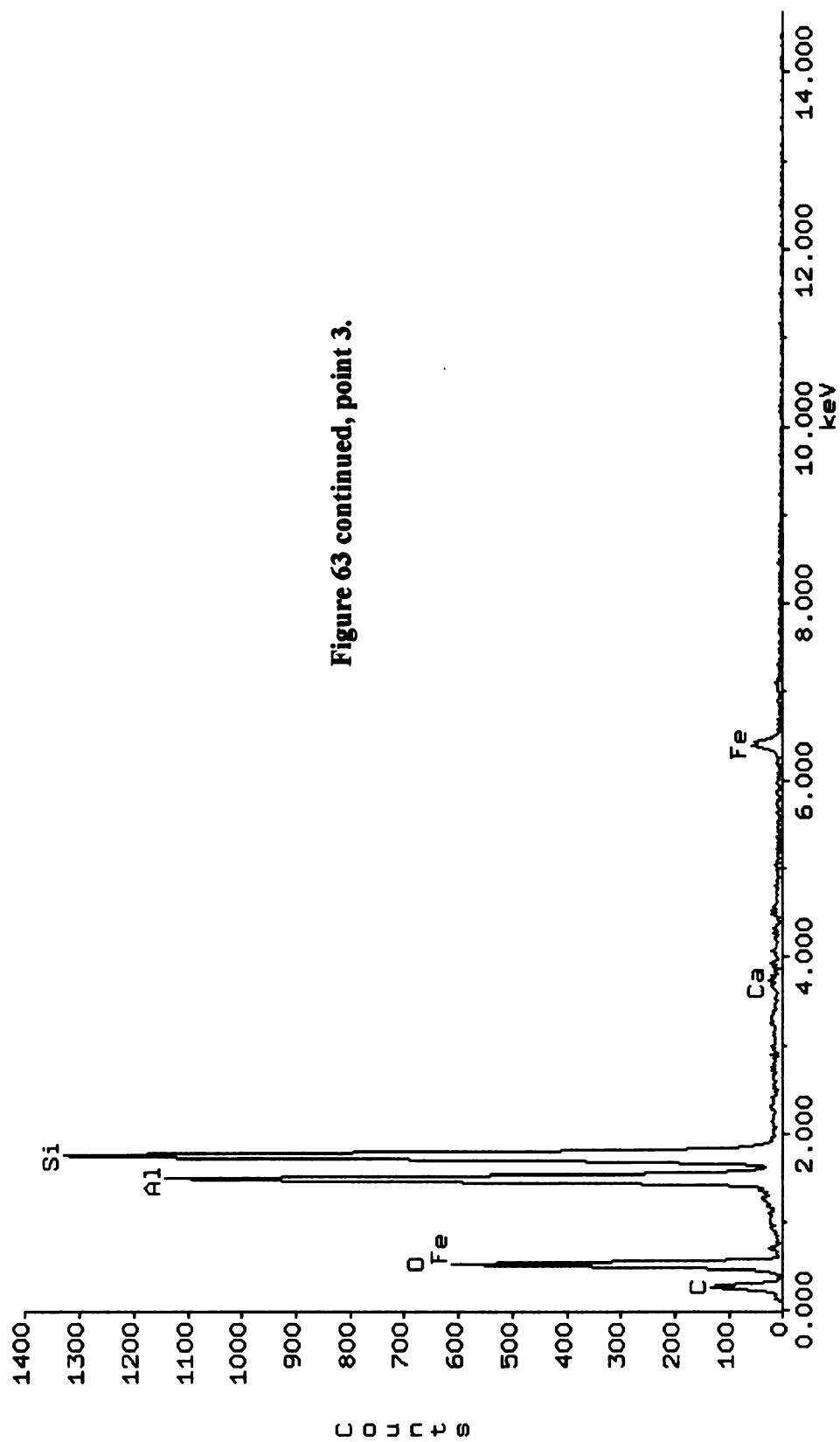


Figure 63 continued, point 3.

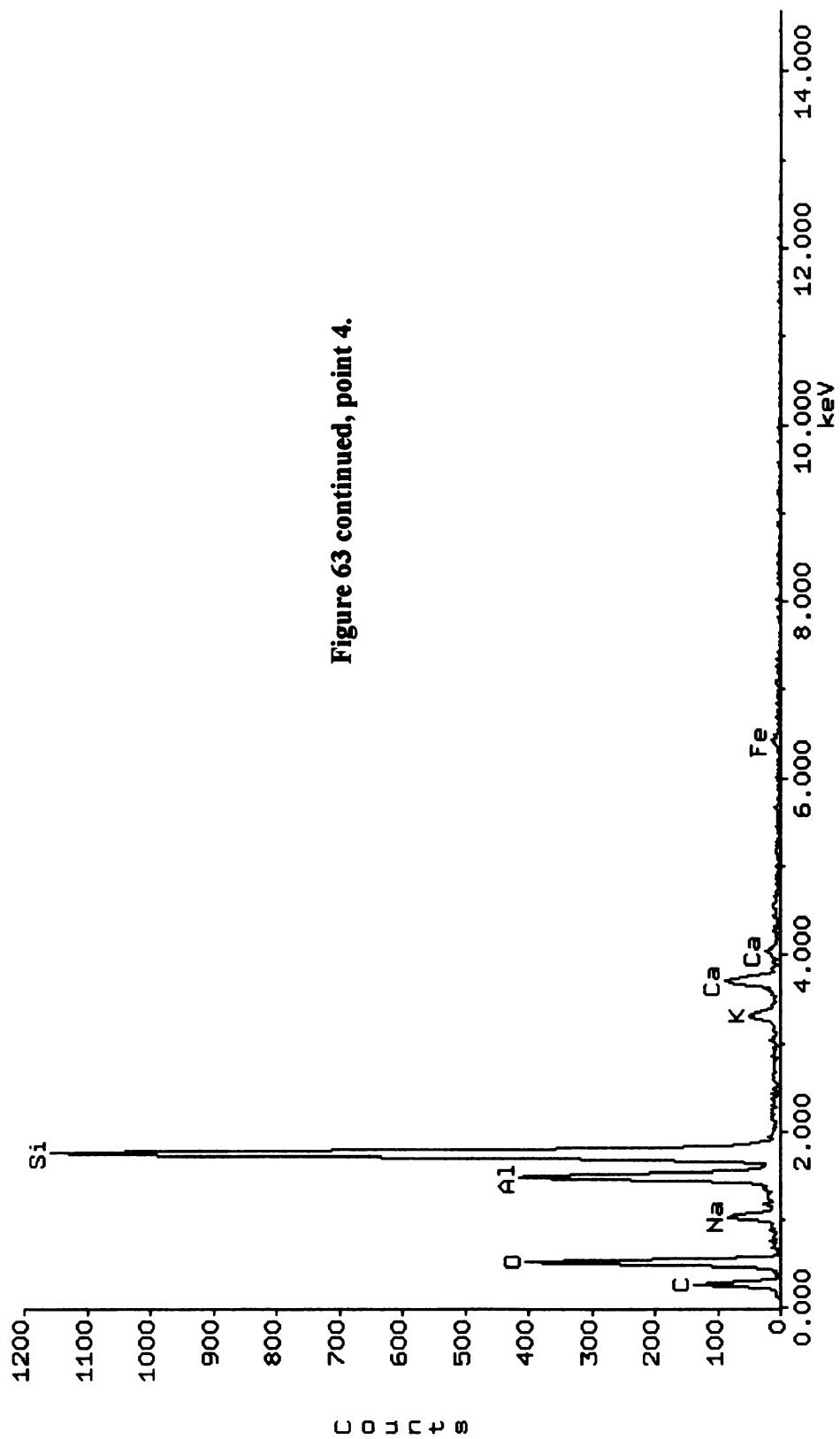
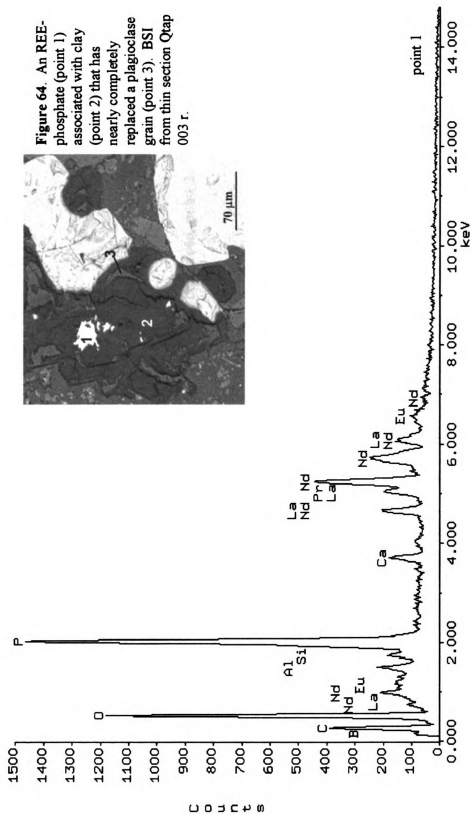


Figure 63 continued, point 4.



**Figure 64.** An REE-phosphate (point 1) associated with clay (point 2) that has nearly completely replaced a plagioclase grain (point 3). BSI from thin section Qtap 003 r.

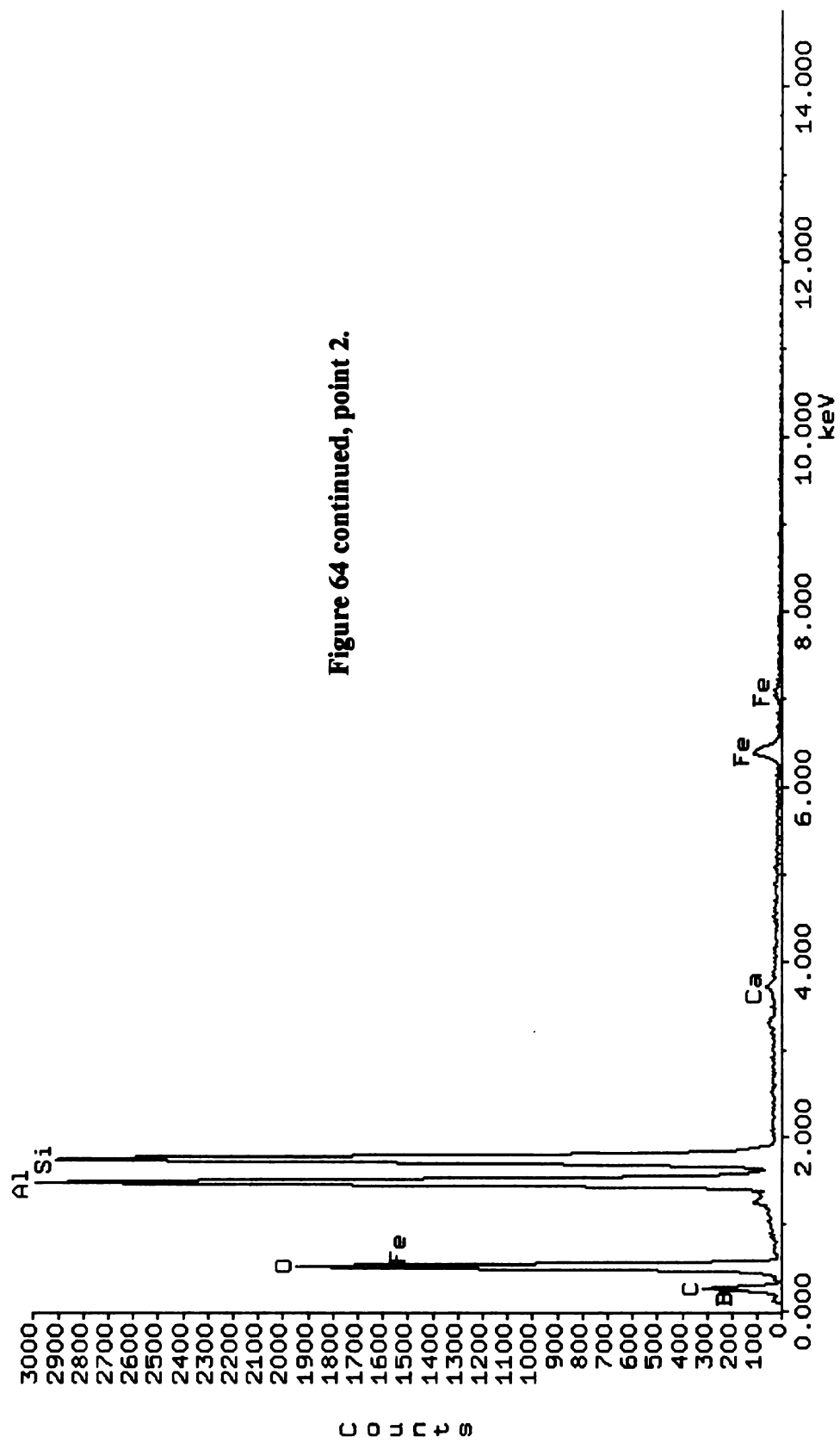


Figure 64 continued, point 2.



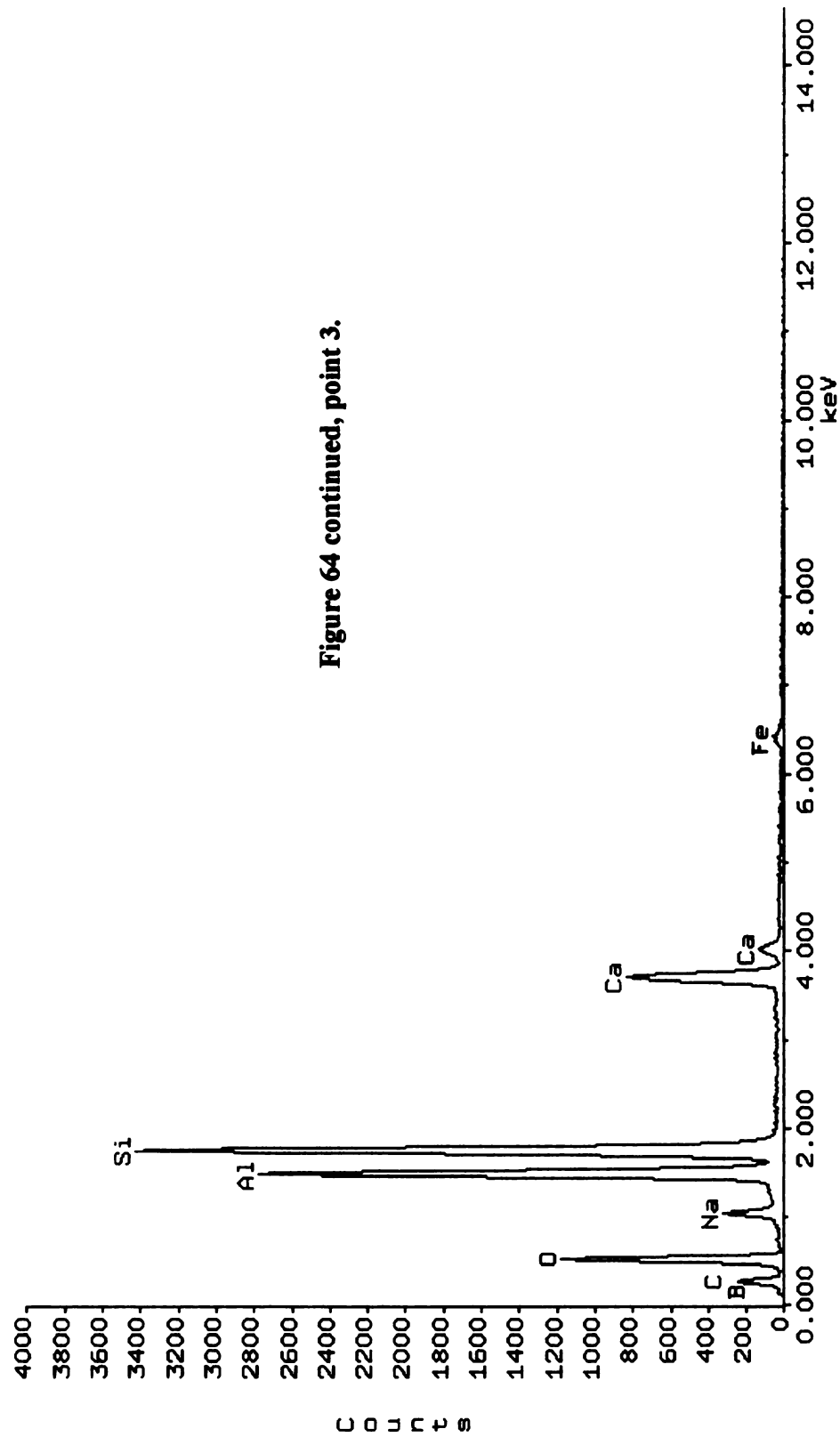
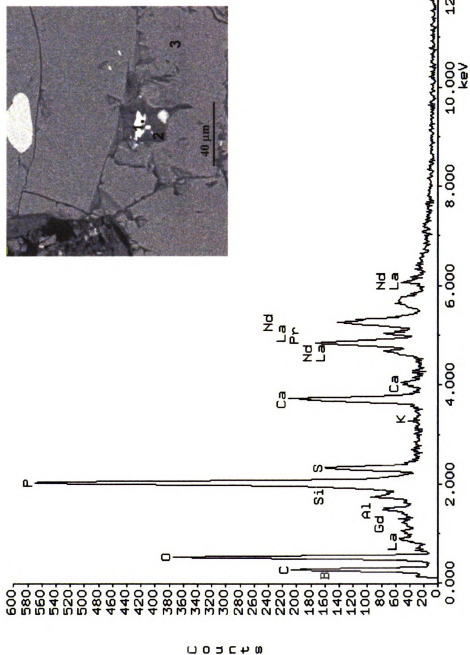


Figure 64 continued, point 3.

**Figure 65.** An LREE-P phase (point 1) among clay (point 2) within a fracture in a clinopyroxene (point 3). BSI from thin section Qtapg 001 r.



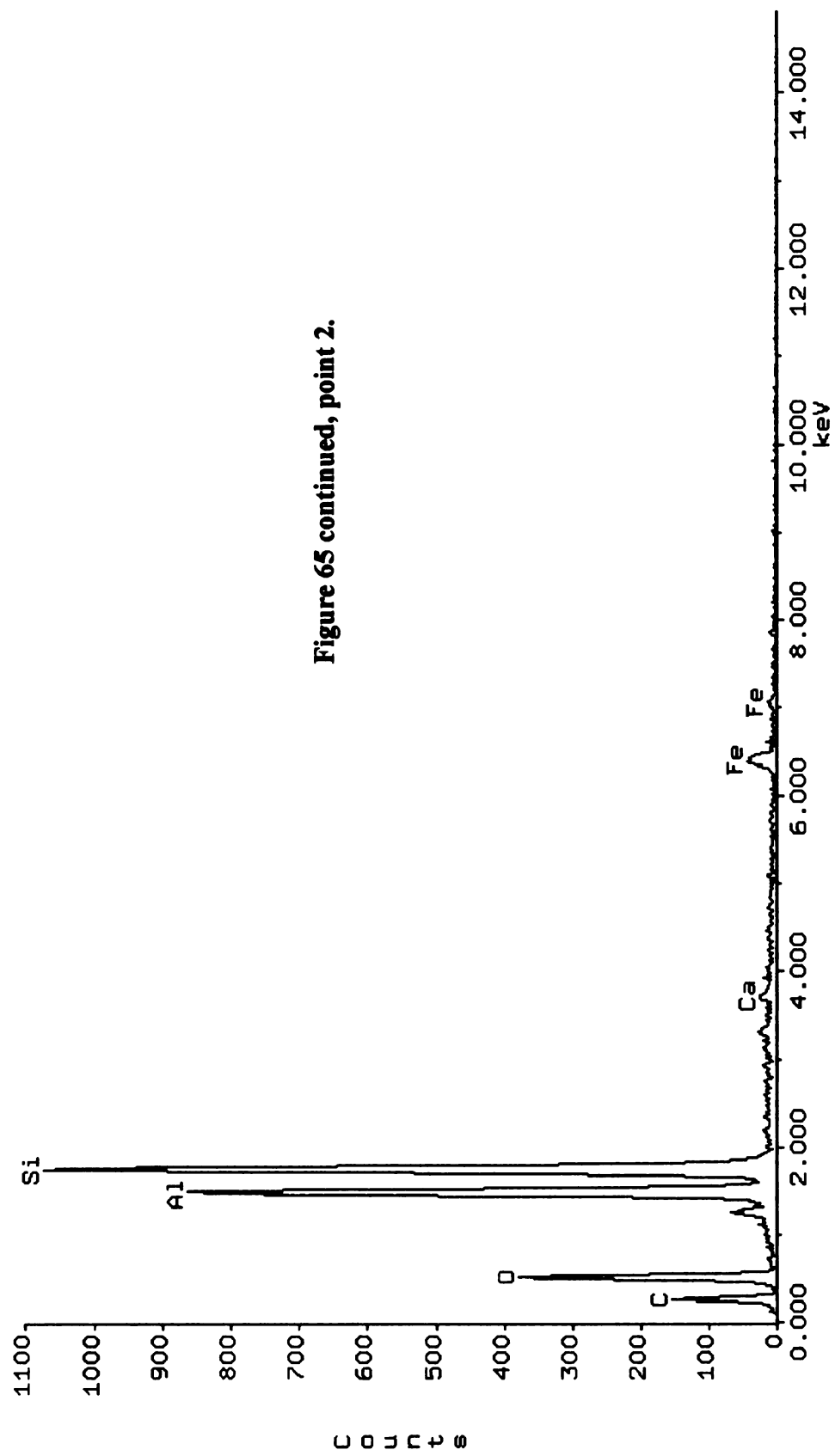


Figure 65 continued, point 2.

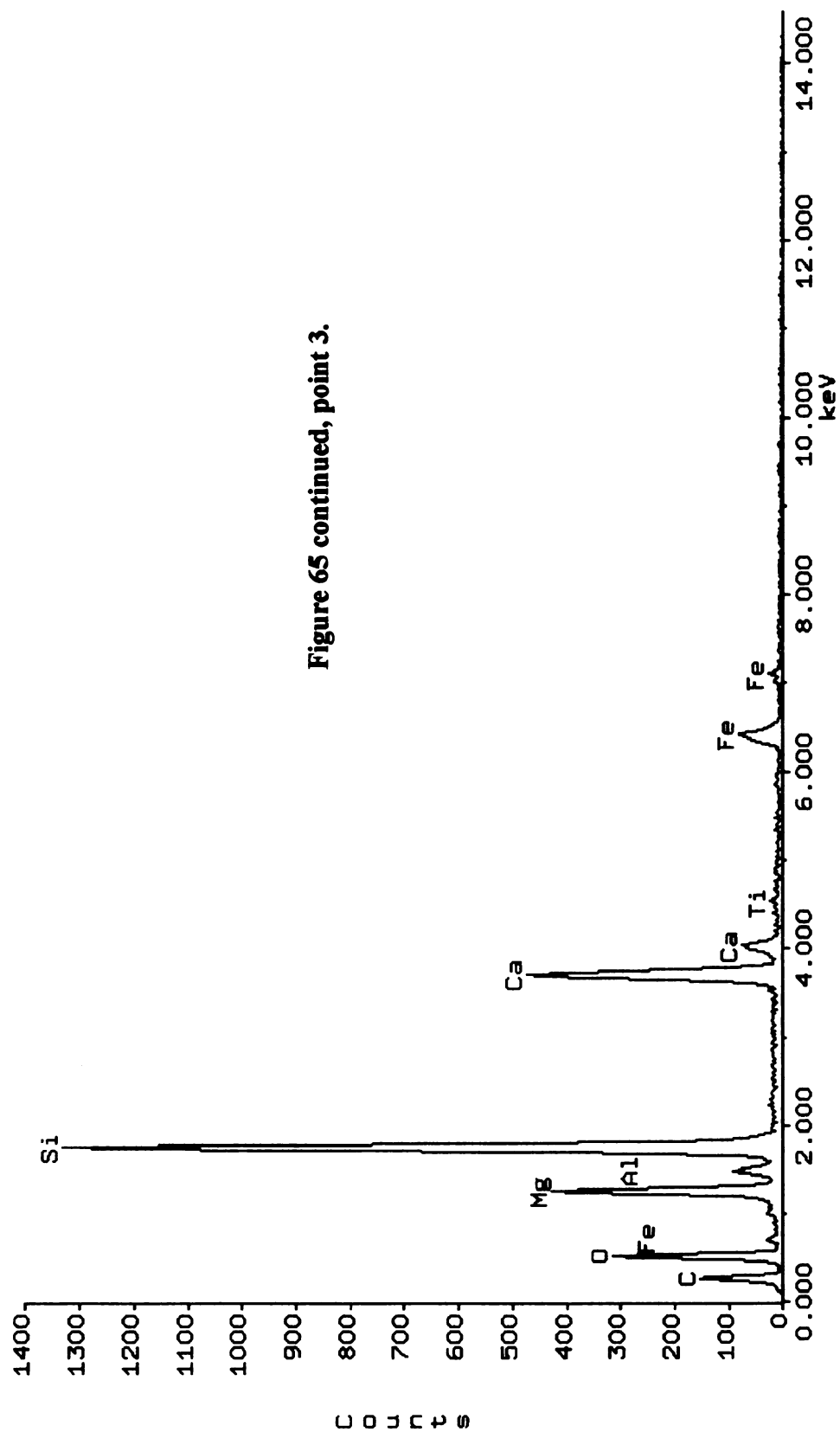
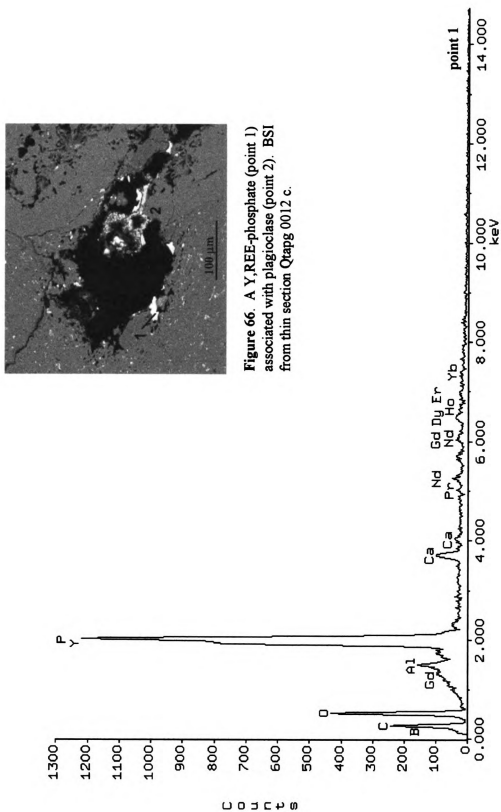


Figure 65 continued, point 3.



**Figure 66.** A Y, REE-phosphate (point 1) associated with plagioclase (point 2). BSI from thin section Qtzpg 0012 c.

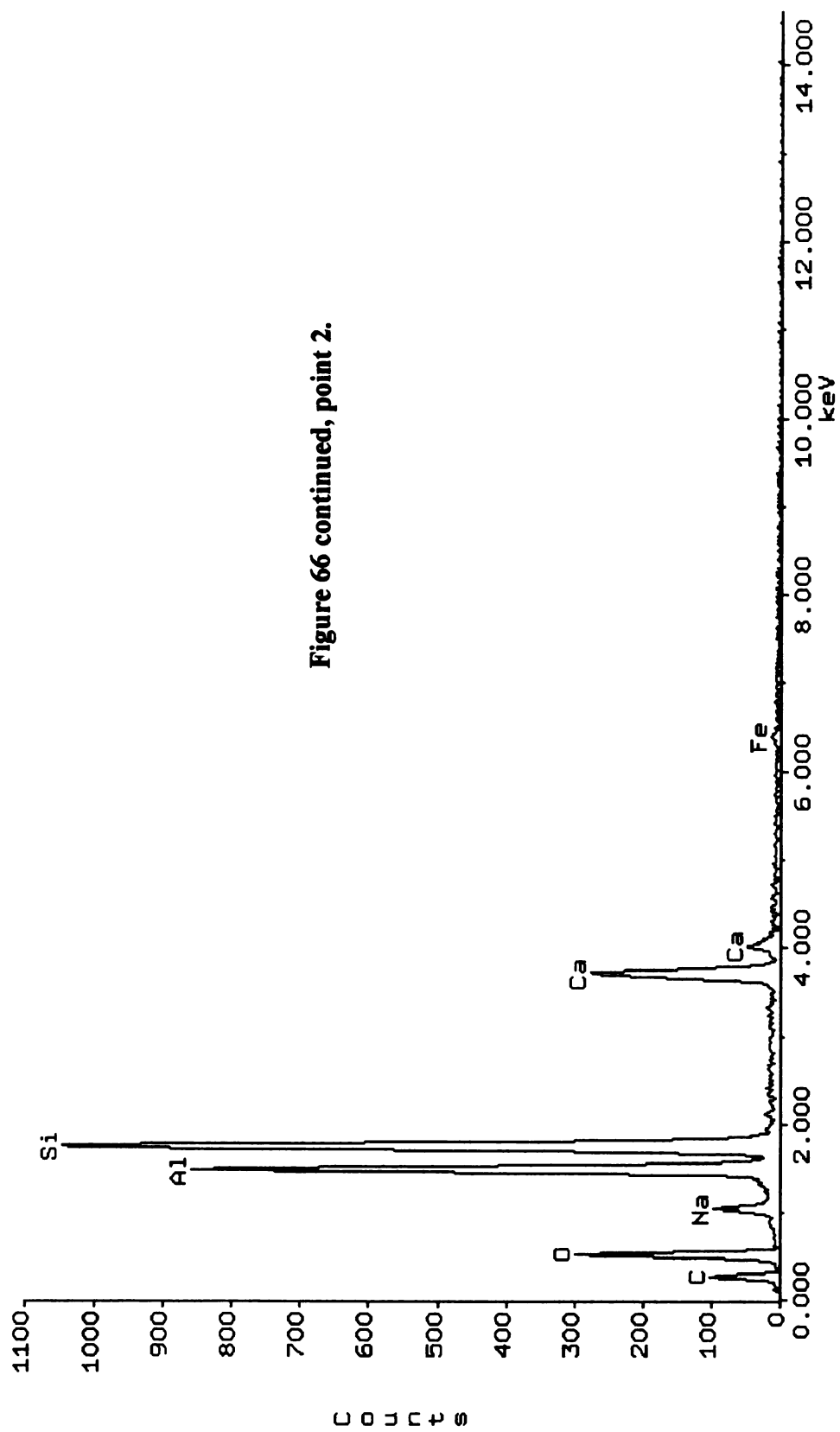
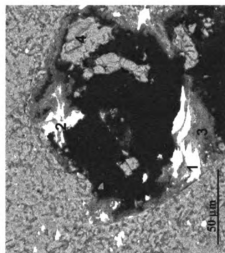
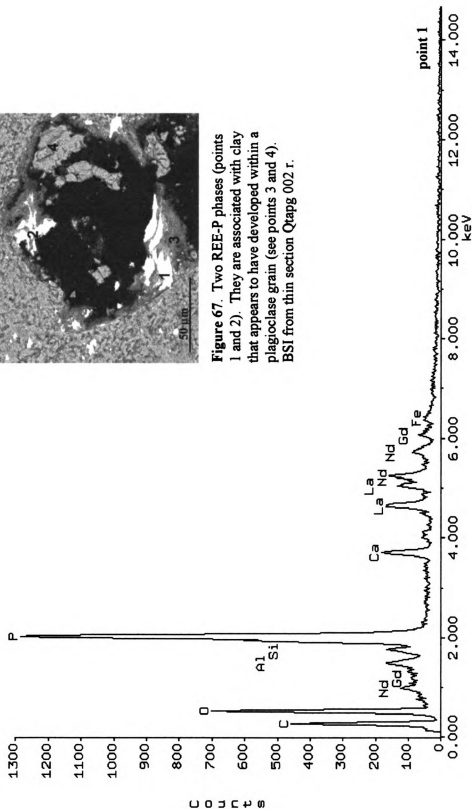


Figure 66 continued, point 2.



**Figure 67.** Two REE-P phases (points 1 and 2). They are associated with clay that appears to have developed within a plagioclase grain (see points 3 and 4). BSI from thin section Qapg 002 r.



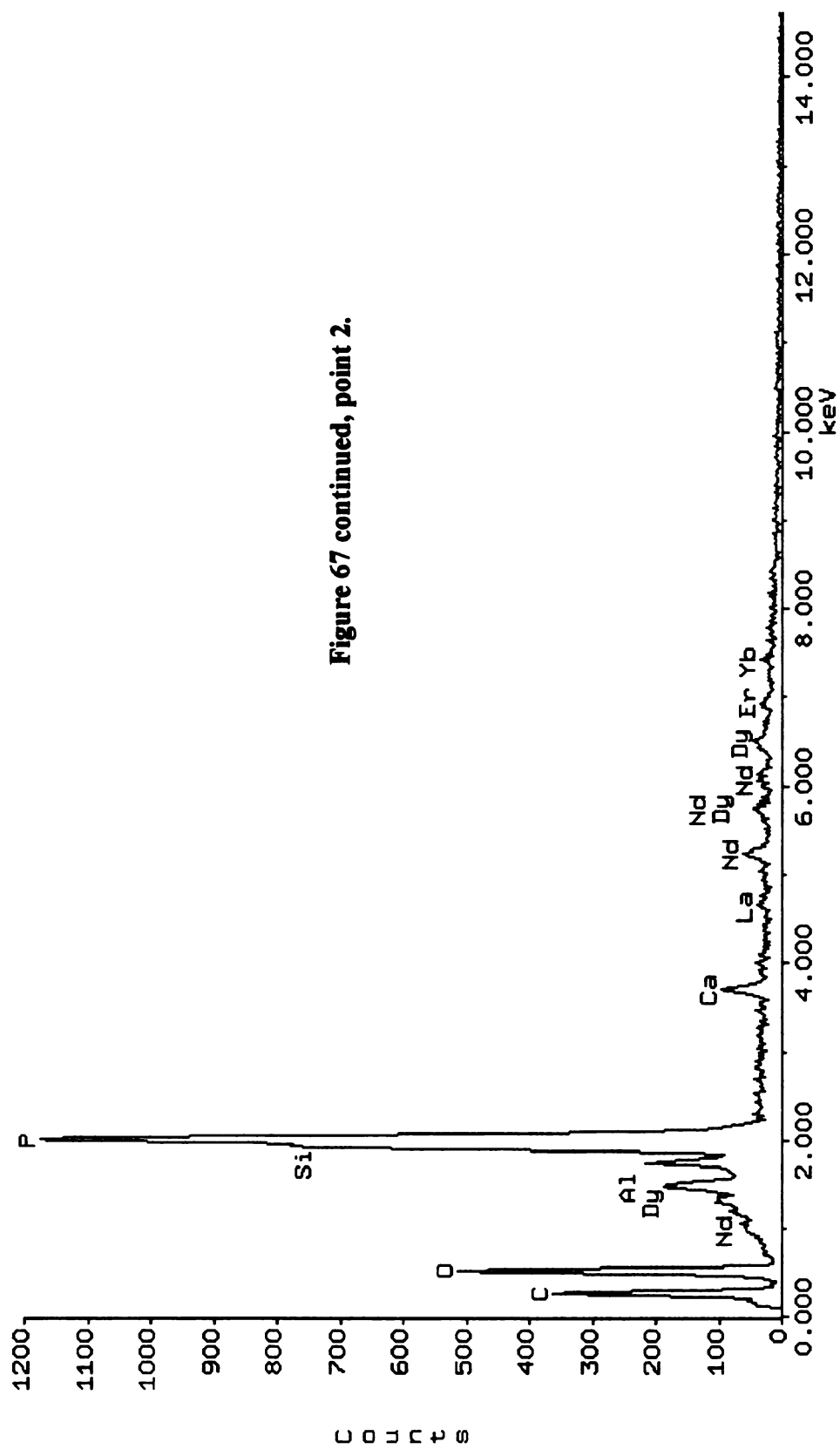


Figure 67 continued, point 2.



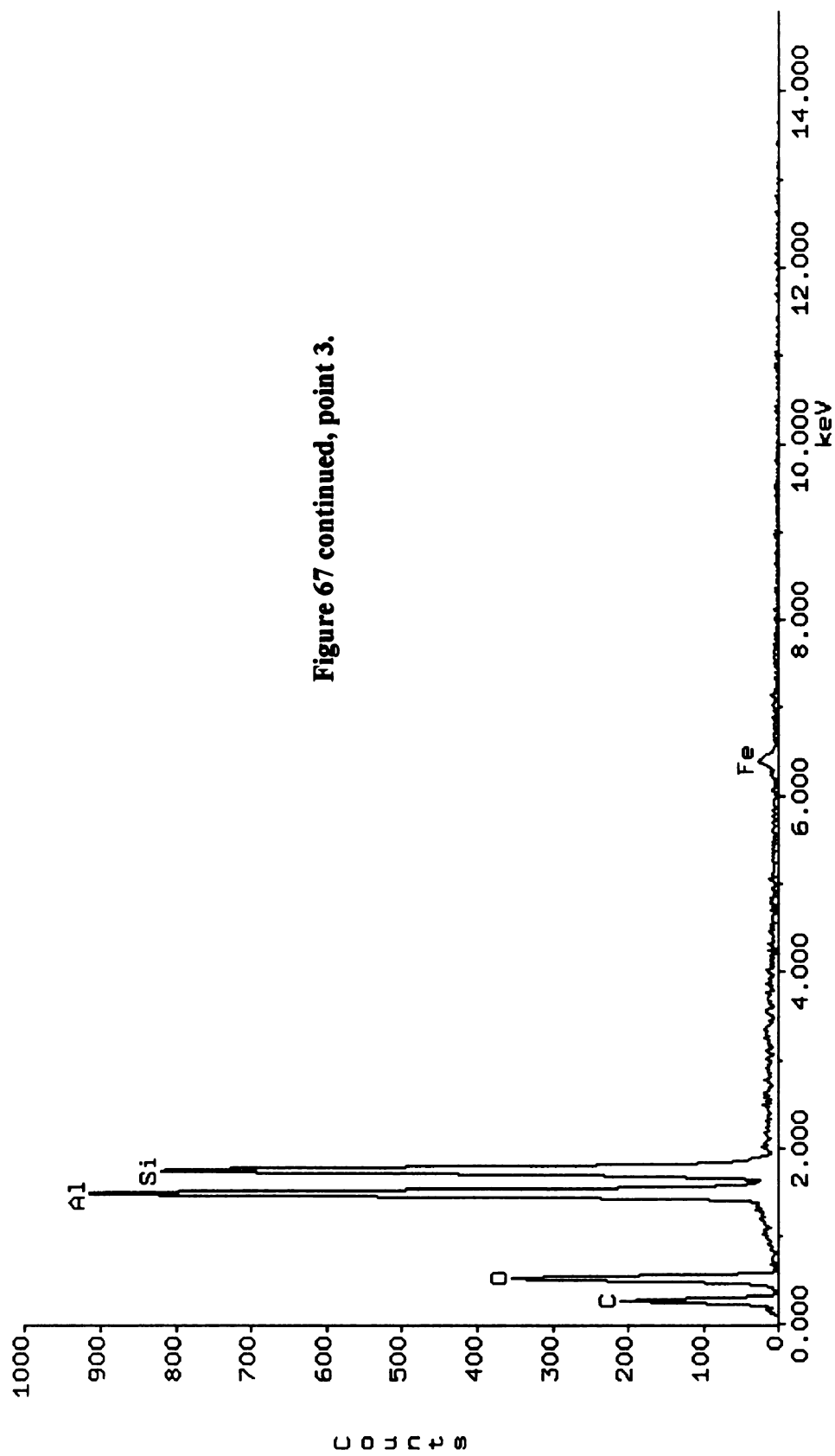


Figure 67 continued, point 3.

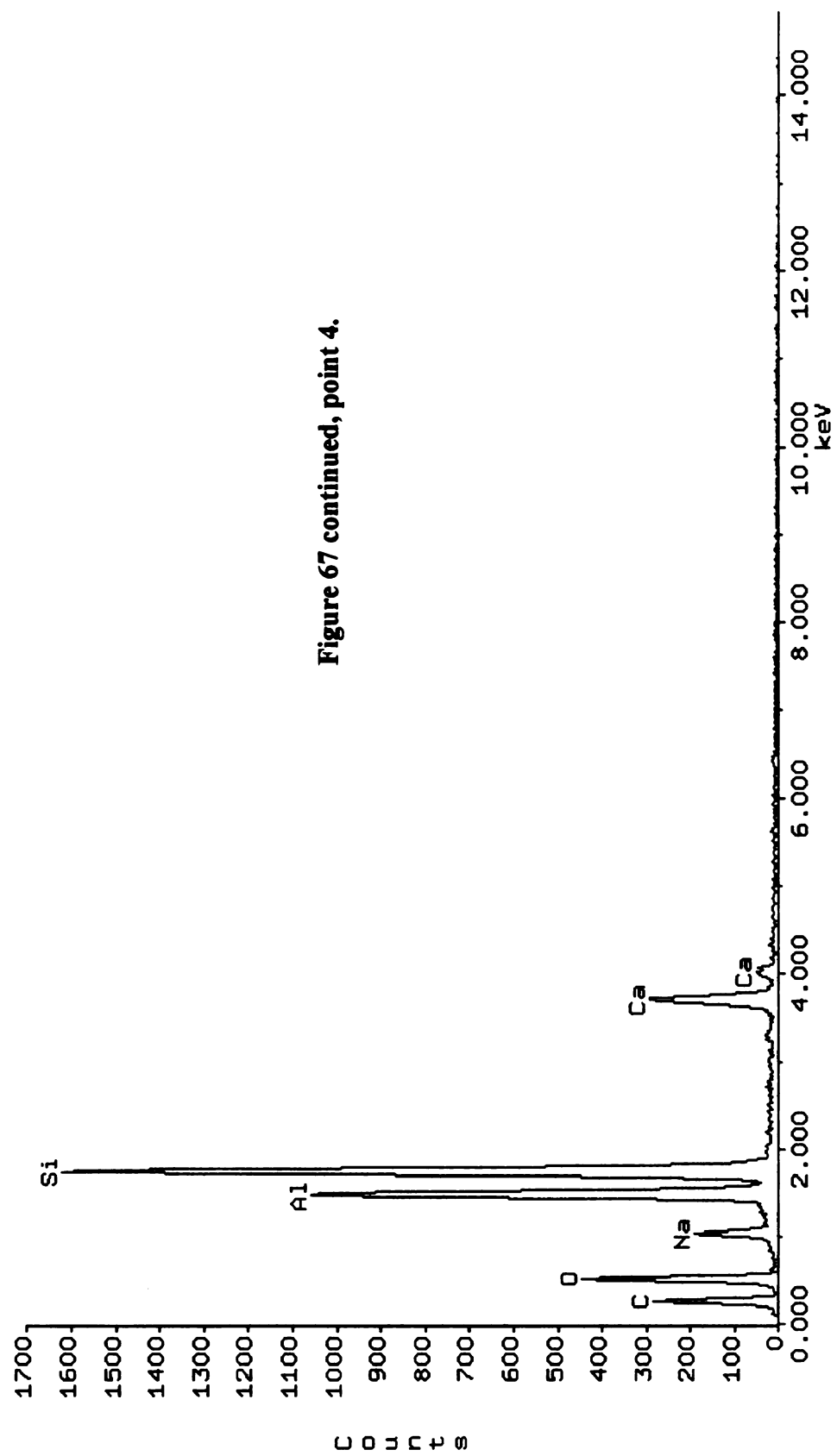
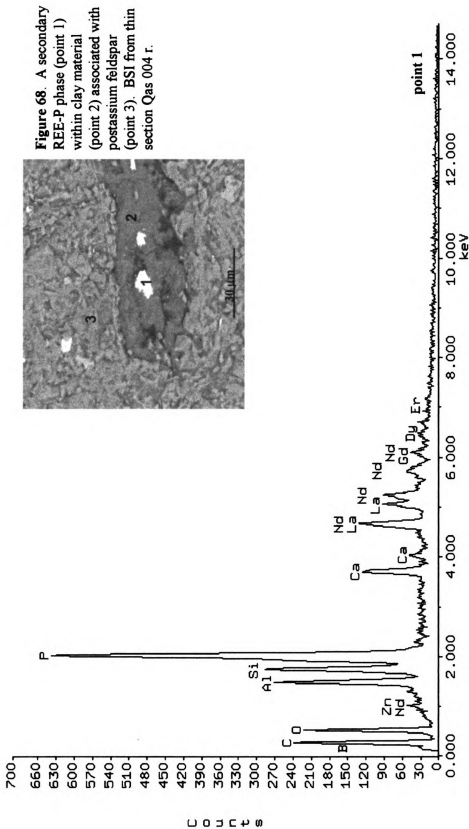
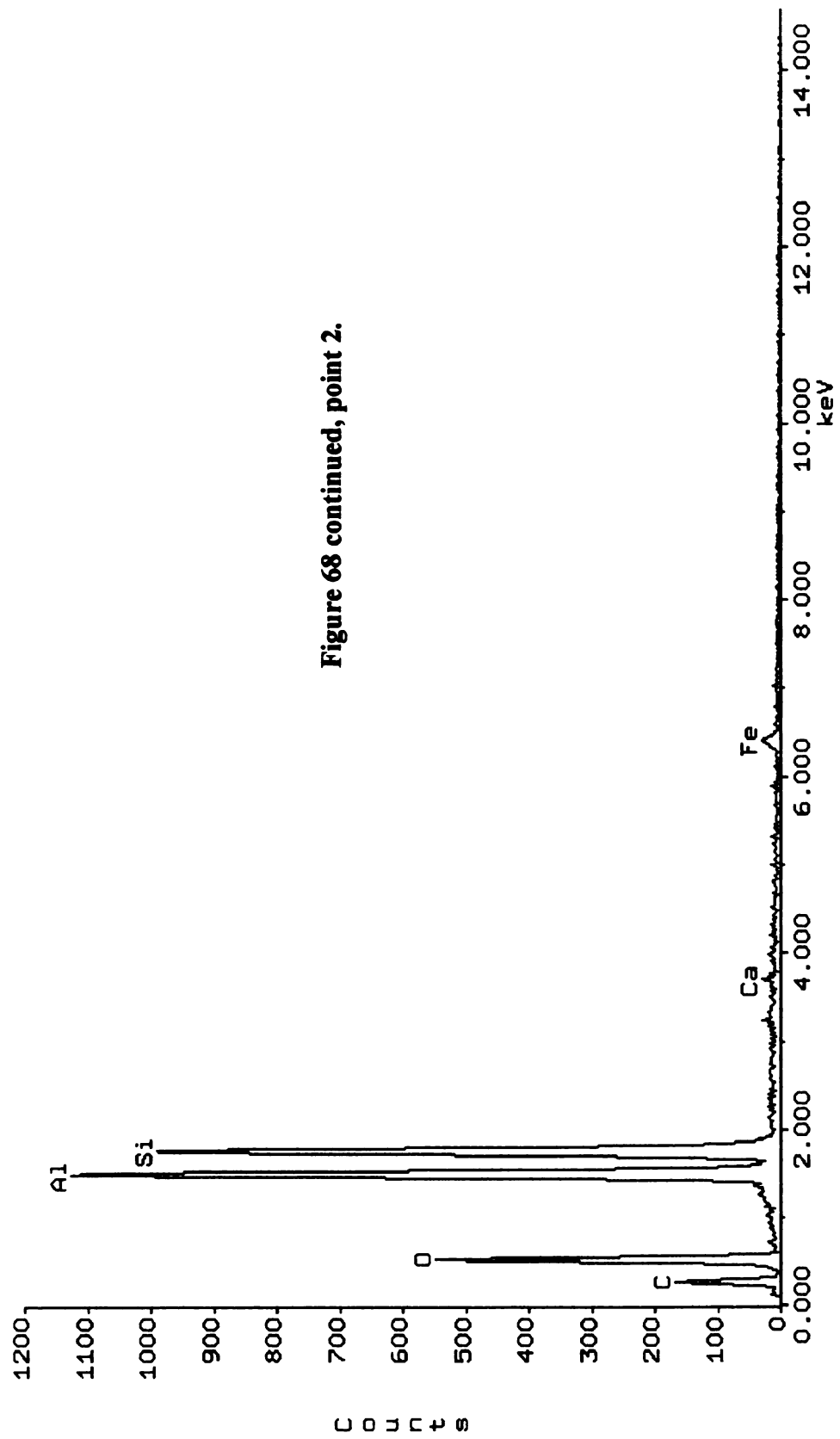


Figure 67 continued, point 4.





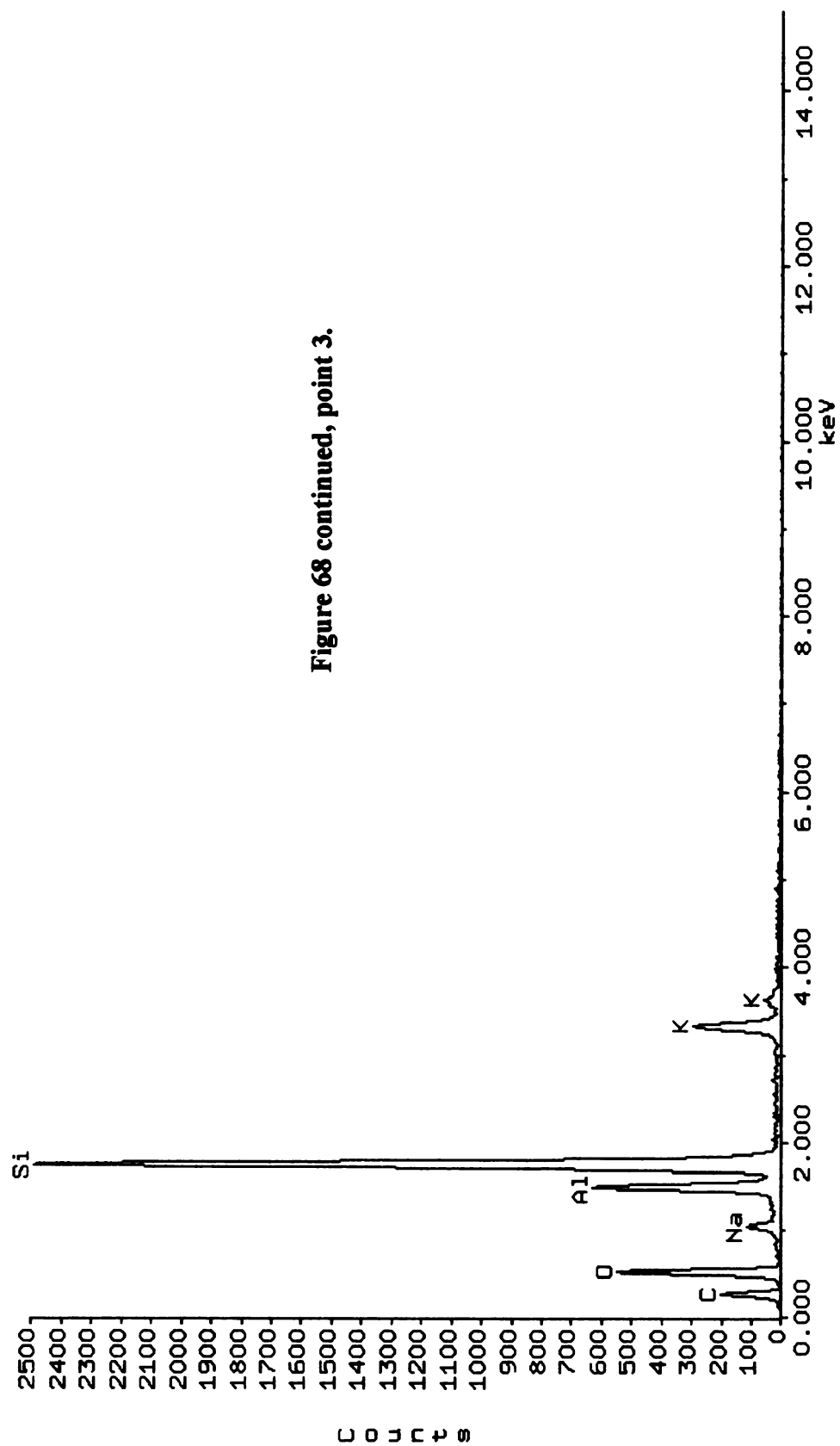
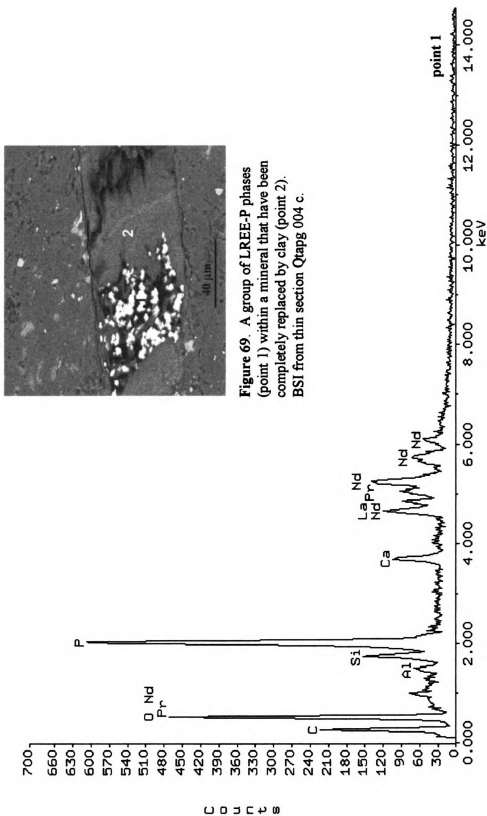
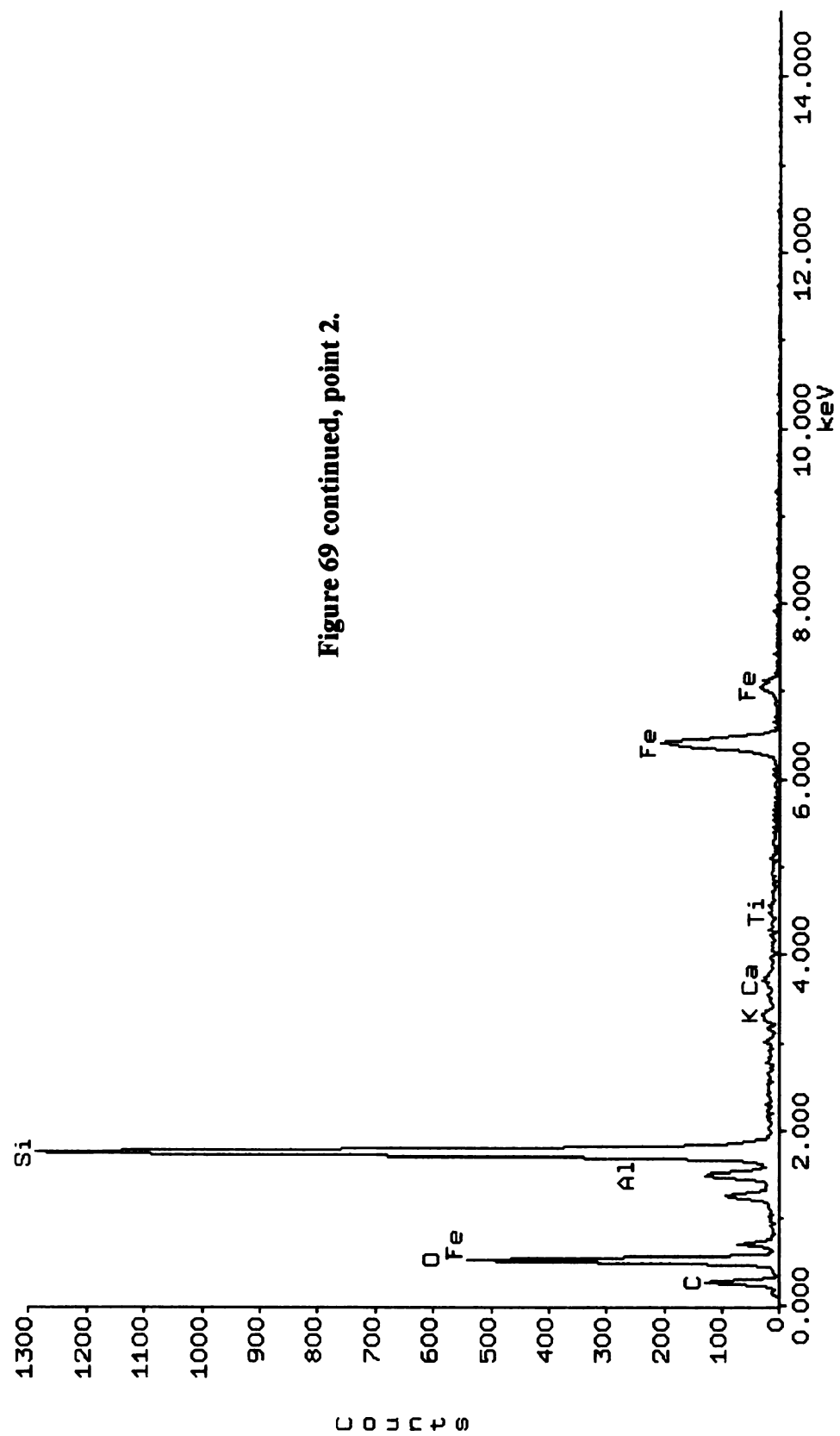
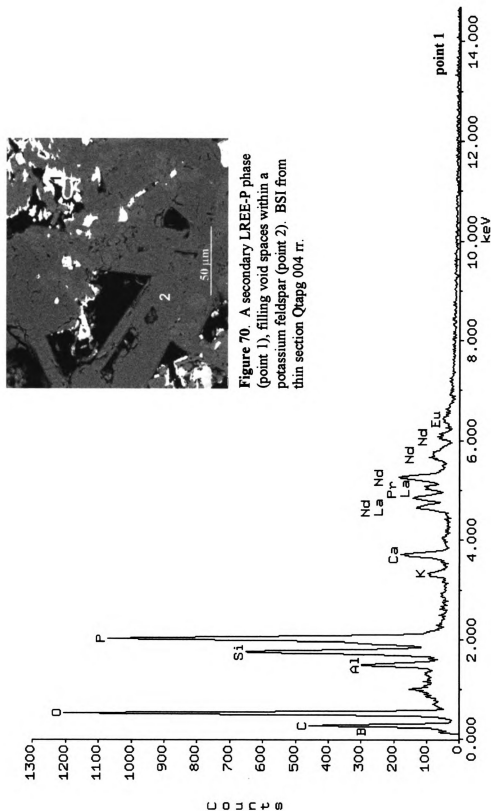


Figure 68 continued, point 3.



**Figure 69.** A group of LREE-P phases (point 1) within a mineral that have been completely replaced by clay (point 2). BSI from thin section Qtapg 004 c.





**Figure 70** A secondary LREE-P phase (point 1), filling void spaces within a potassium feldspar (point 2). BSI from thin section Qtapg 004 tr.



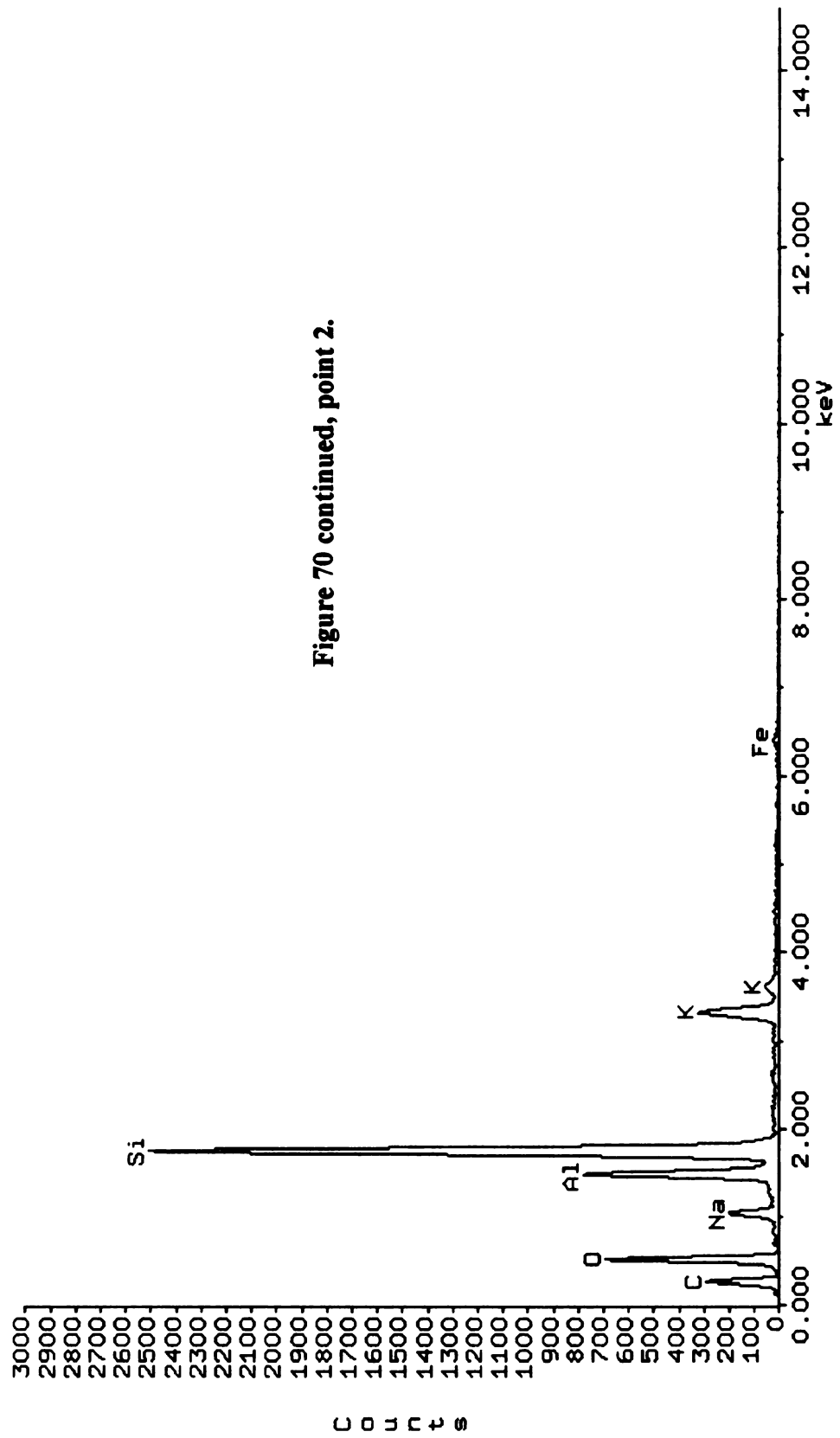
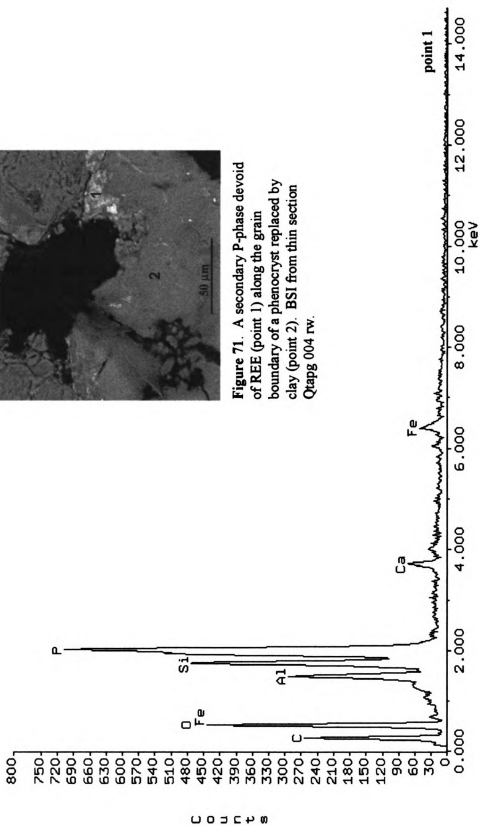


Figure 70 continued, point 2.



**Figure 71.** A secondary P-phase devoid of REE (point 1) along the grain boundary of a phenocryst replaced by clay (point 2). BSI from thin section Qapag 004 rw.

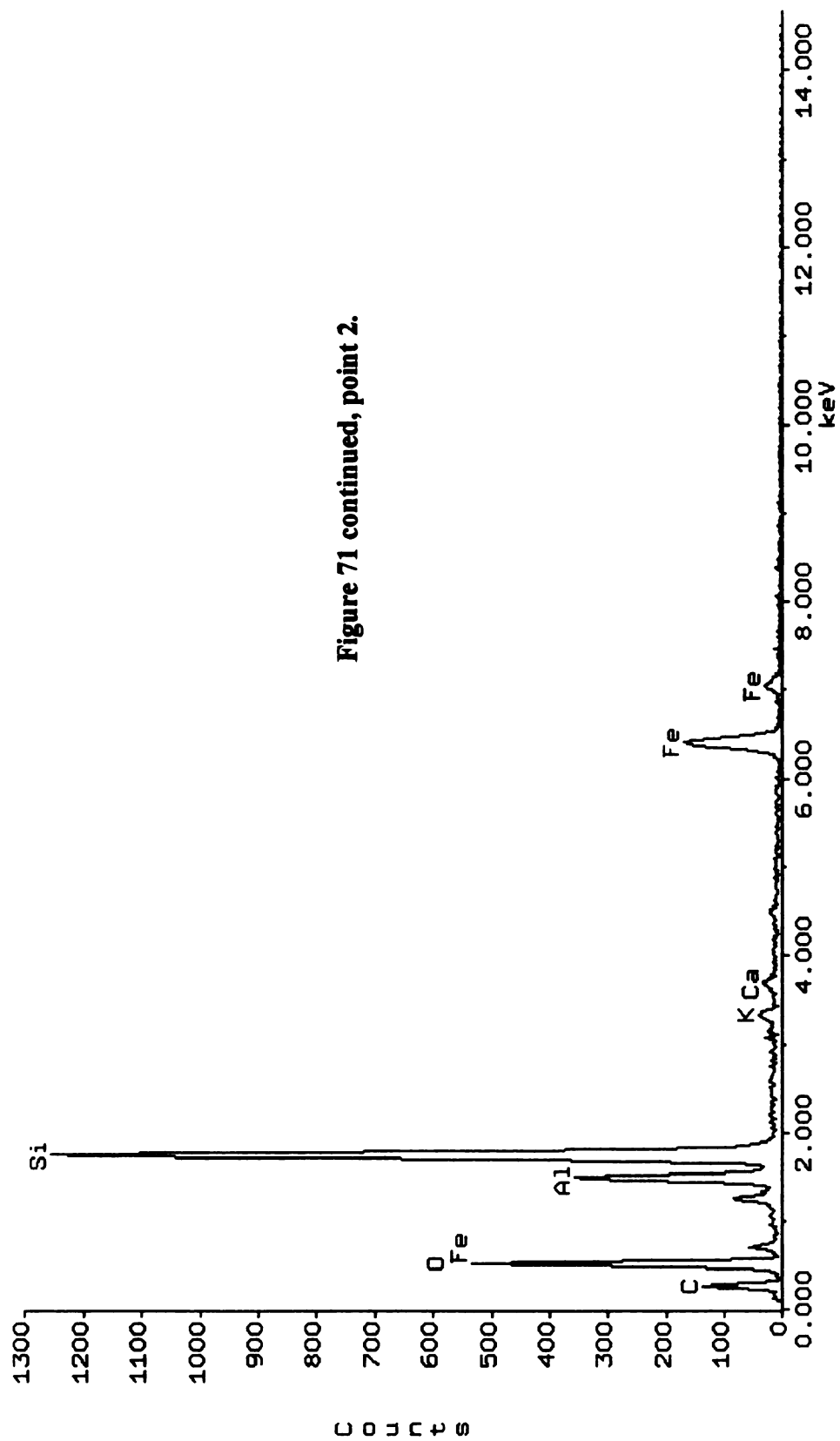
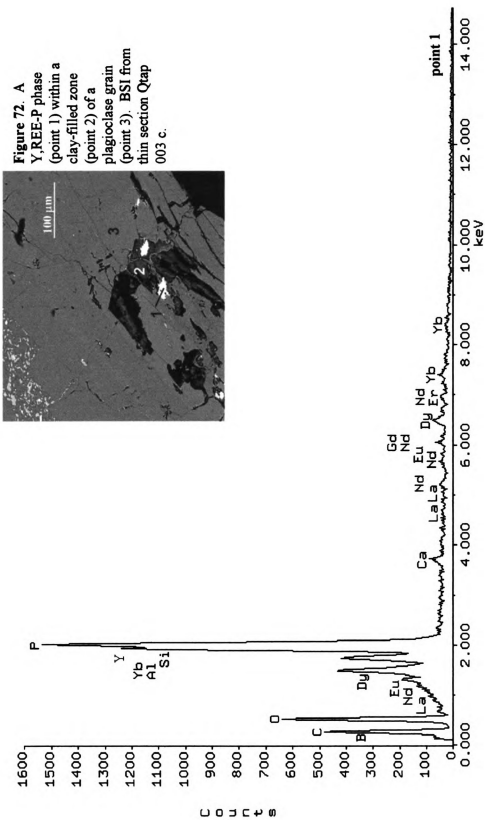


Figure 71 continued, point 2.



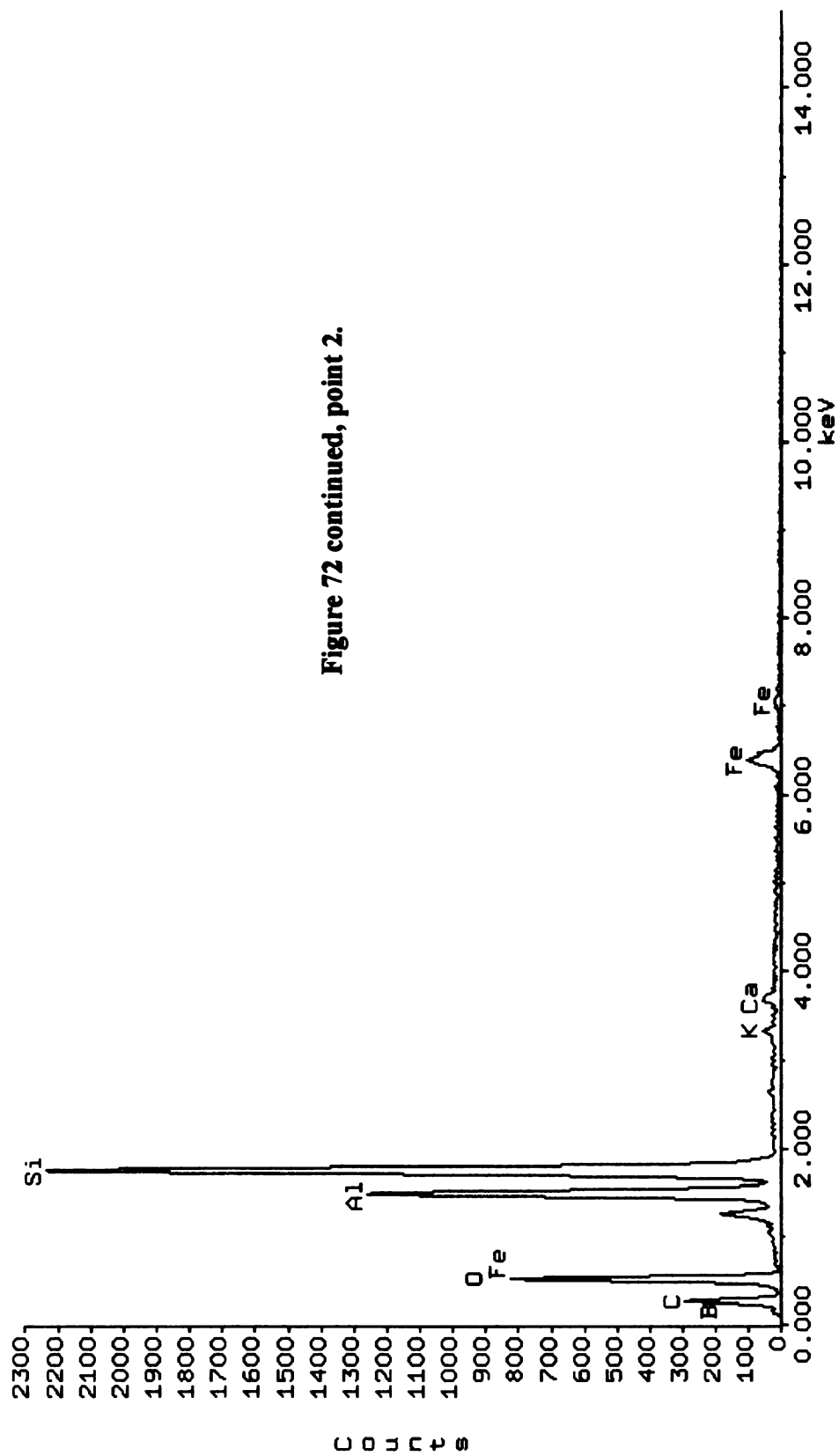


Figure 72 continued, point 2.

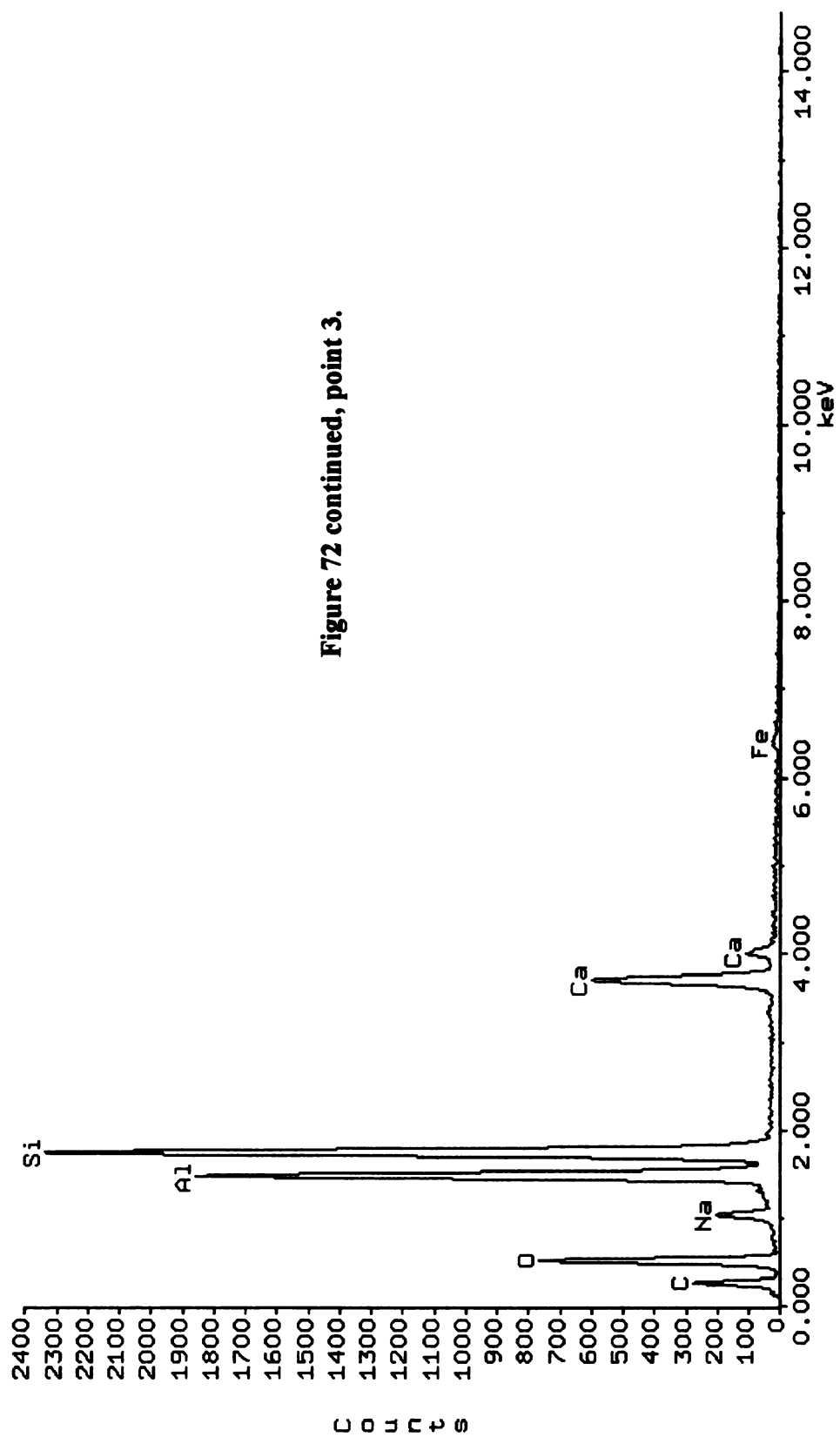
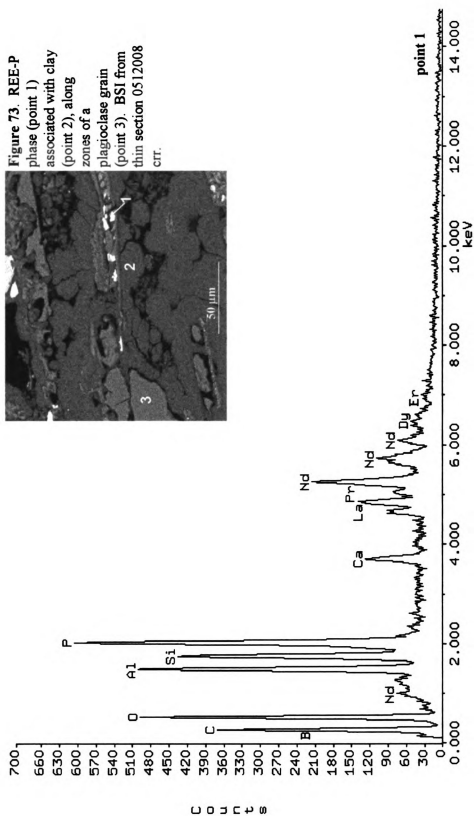


Figure 72 continued, point 3.



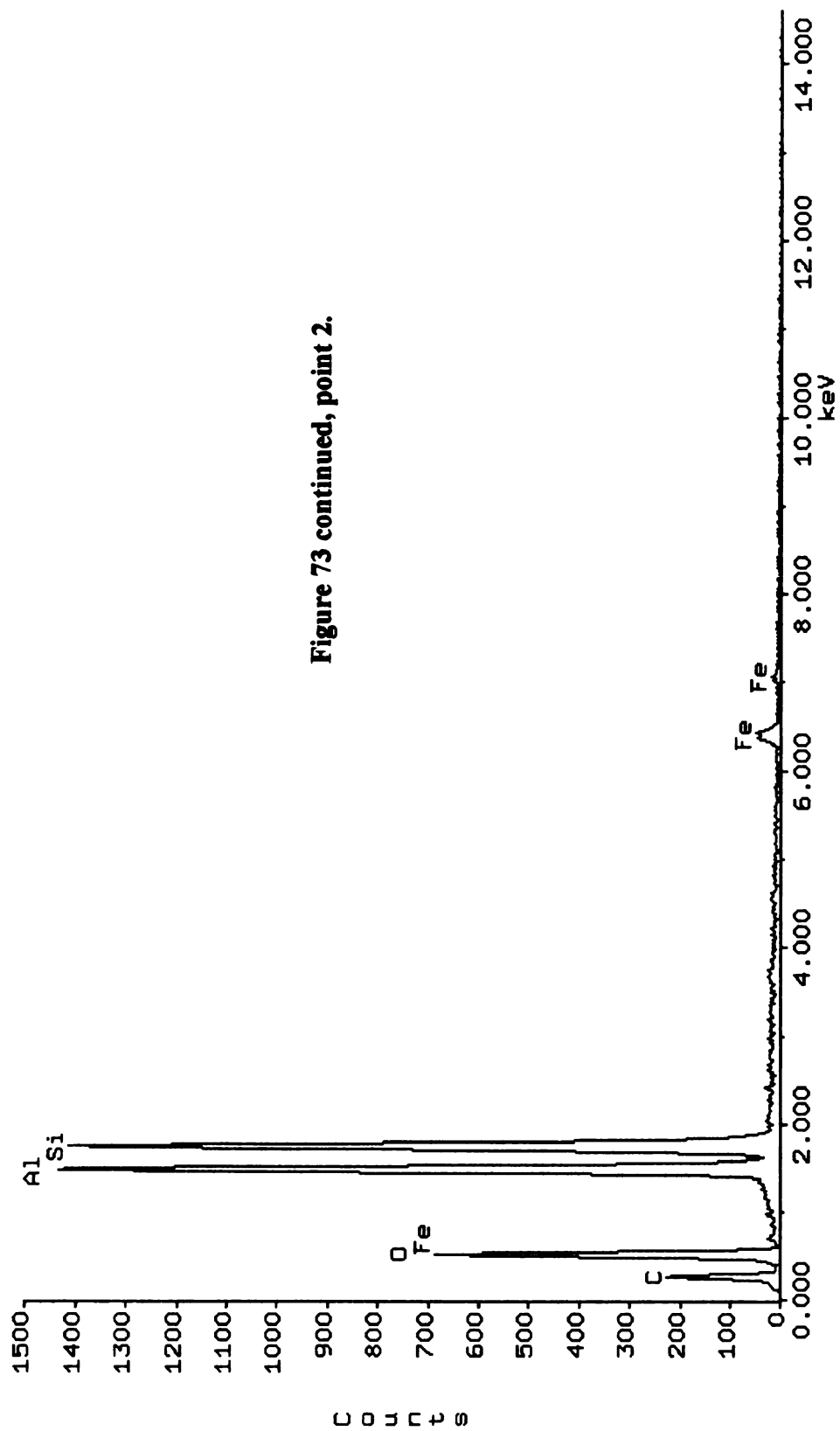


Figure 73 continued, point 2.



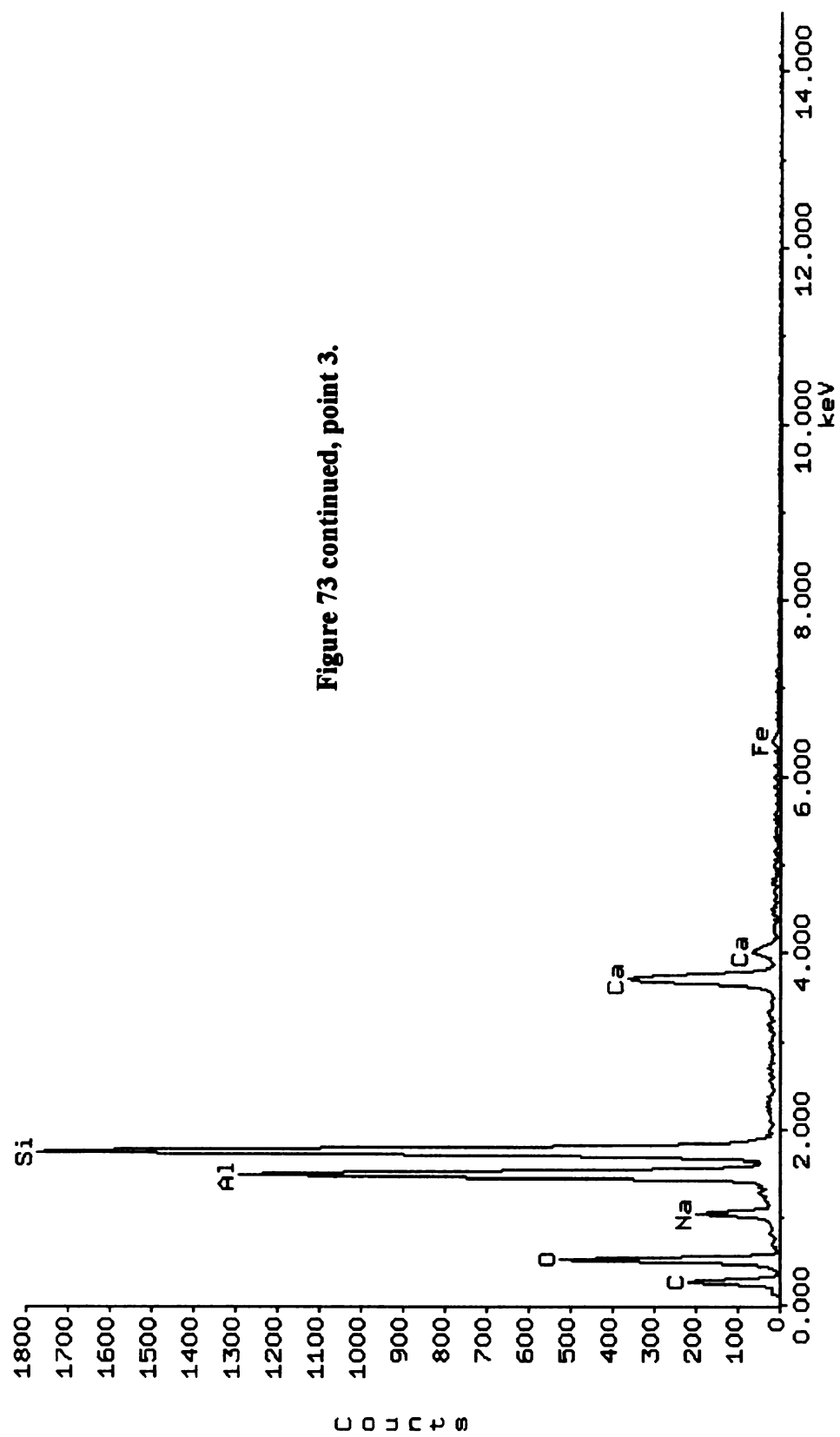
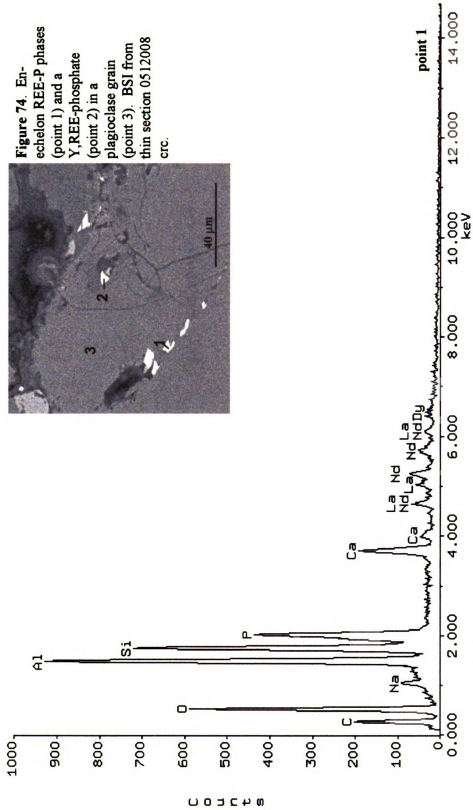


Figure 73 continued, point 3.



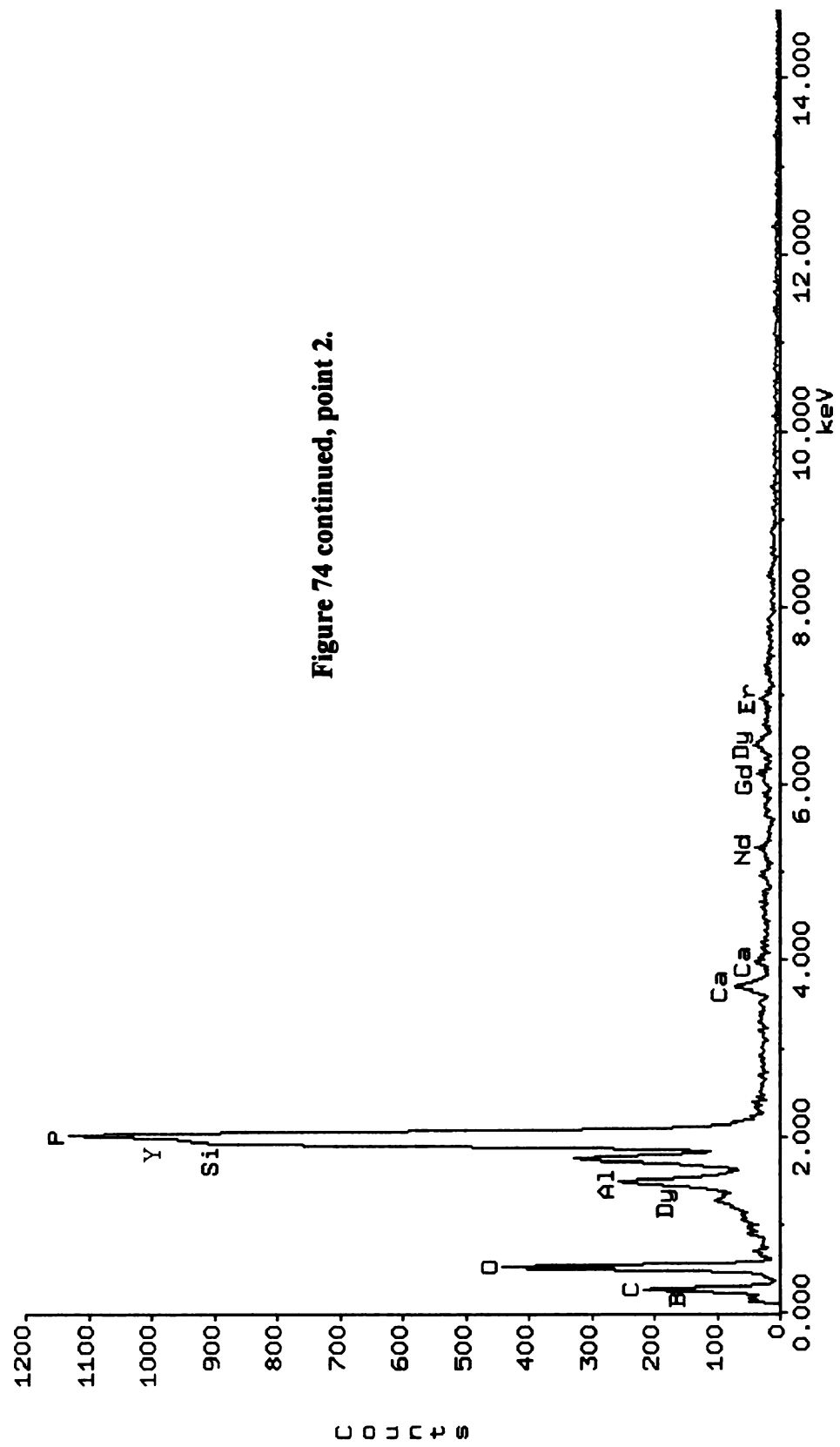
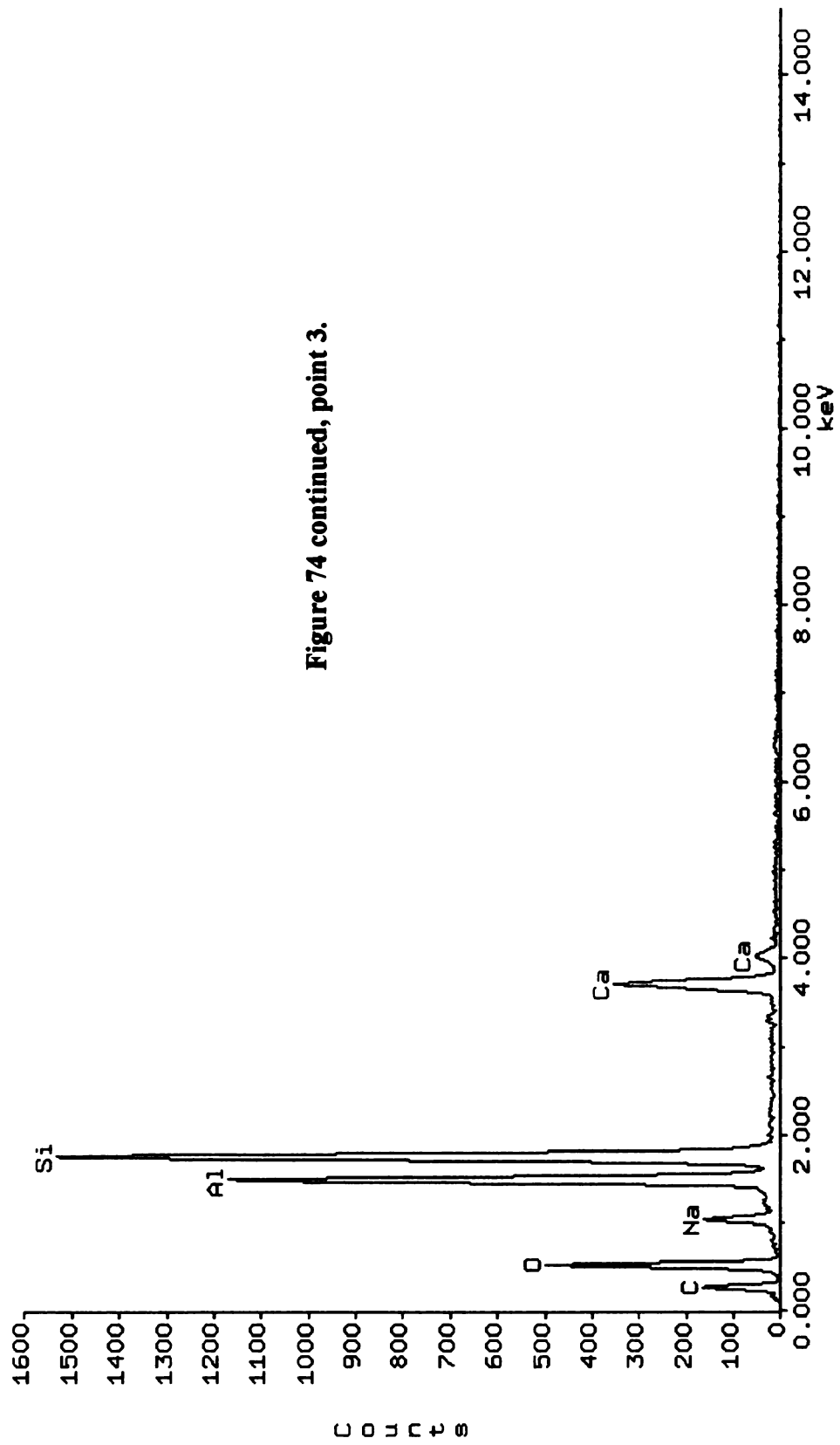
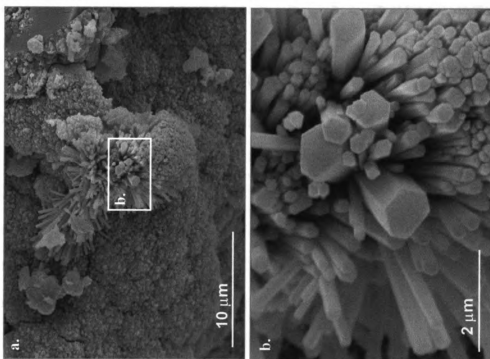


Figure 74 continued, point 2.





**Figure 75.** Secondary-electron image of an REE-phosphate on the surface of a clay-lined crevice in a plagioclase phenocryst from the rind of corestone 0512008. Image b is a magnified section of image a.

## DISCUSSION

### *Primary mineral alteration*

The mobilization and distribution of trace elements within a weathering profile depends on the weathering and/or precipitation of host phases. The REE and other trace elements are important to petrologists because they give insight into magma source composition and degrees of melting. Therefore, it is crucial to understand the nature and distribution of weathering processes that can alter trace element compositions and mislead petrologists.

Appendix D lists the mineralogies observed in the Tecuamburro samples (plagioclase, pyroxene, hornblende, potassium feldspar, apatite, and opaque minerals). Of the primary minerals observed, apatite plays a particularly important role in this study. Apatite weathers more easily than pyroxene or hornblende, and its instability has even been compared to olivine (Bateman and Catt, 1985). As acidity increases, apatite solubility increases greatly. EDS data show that the common secondary REE-phases have high concentrations of phosphorous. Apatite has the highest distribution coefficient for REE of any other mineral observed at Tecuamburro (the  $K_d$  for all REE is  $>1$ , and ranges from 14.5–46; Koppers and Nielsen, 2002). It is therefore likely that primary apatite is the source of P (and possibly REE) for the secondary phases, as observed by Harlavan and Erel (2002), in granitoids; Taunton et al. (2000), in granites; and Walter et al. (1995), in carbonatites). Since the only primary apatite observed in the samples is present as inclusions in phenocrysts (e.g. Qas 003; figure 58), it is inferred not only that

the weathering of apatite is important, but weathering of the phenocrysts is important as well.

Throughout the Tecuamburro samples, plagioclase is the most weathered phenocryst (weathering mainly along compositional zones and at glass inclusions), and is also the phase that most often hosts the secondary REE-P-bearing phases. Pyroxene and K-feldspar are also hosts of these secondary phases, but are generally less weathered than the plagioclase grains within the same thin section. If fractures and other pathways open in a phenocryst due to weathering, the apatite inclusions are highly susceptible to the weathering solution, and can release the REE and P needed to eventually precipitate the secondary REE-phases.

Plagioclase and pyroxene weathering rates vary with pH, temperature, and mineral composition (Brantley and Chen, 1995; Blum and Stillings, 1995). There is some compositional variation in the phenocrysts from Tecuamburro. Cameron (1998) noted a range of compositions in plagioclase along the Guatemalan volcanic front from  $An_{46}$  to  $An_{92}$ . Two Tecuamburro plagioclase phenocrysts analyzed from unit Qai (38 ka, younger than the units included in this study) yielded values of a)  $An_{79.25}$  in the core,  $An_{66.58}$  in the rim, and b)  $An_{88.47}$  in the core,  $An_{72.44}$  in the rim, placing them in the labradorite-bytownite range. Microprobe data for Tecuamburro clinopyroxenes from unit Qai indicate compositions ranging from 41.48–43.60 mol% Wollastonite, and 44.50–44.82 mol% Enstatite (Cameron, 1998). The calcic nature of the phenocrysts in these rocks may explain the ease and variability with which they weather.

### *Clays and other secondary minerals*

The clays observed in the Tecuamburro samples by SEM and XRD (kaolinite and smectite; figures 46–49) are expected, given the primary mineralogy (Colman, 1982). Because plagioclase is the most easily weathered phenocryst phase, Al-rich secondary minerals are common (e.g. figures 54, 63, and 64) and that in some samples, gibbsite has precipitated (figure 51).

In addition to clays, secondary phases that affect Ba concentration, such as barite and hollandite, are present in a number of samples. Barite is observed in the rind of Qas 003, and in the intermediate zone and rind of Qtapg 001 (figures 59 and 60). Although Qas 003 does not contain the REE-P-phase, the core and intermediate zones do contain fresh, primary apatite inclusions in plagioclase and pyroxene phenocrysts (figure 58). Qtapg 001 contains not only REE-P-phases (including one that has sulfur), but hollandite as well (figure 62).

Barite is stable over a range of temperatures (0–400°C), pressures (1–2000 bars), and redox conditions. However, it is easily destroyed in reducing conditions and at pH < 4 (Hanor, 2000). Hollandite can also form under a range of conditions. It has been documented as a host for weathering-mobilized trace elements in basaltic soils by Fodor et al. (1994), who observe hollandite in 1.15–1.4 Ma lavas on Kahoolawe Island, Hawai'i. They speculate that REE and Y were mobilized from apatite, and precipitated into the Mn-oxides and secondary phosphates. Microprobe analyses indicate that Ce is highly concentrated in the Hawai'ian hollandite (Fodor et al., 1994) although it has not been observed in hollandite at Tecuamburro. However, the microprobe data used by these



workers has a higher resolution than the SEM data used in this study. It is therefore possible that the hollandite seen in these samples contains Ce in concentrations undetectable by the SEM used. The wide range of conditions under which these phases are stable does not help constrain the nature of the alteration solution, since the relative timing of their formation in these samples is not yet understood.

#### *Development of the REE-P-phase*

The REE-phases in the Tecuamburro samples are observed in both the cores and rims of some Tecuamburro samples, and are usually observed within phenocrysts (figure 72), not in the groundmass. This can be explained in two ways: 1) compositional differences between phenocryst and microlitic plagioclase, and 2) the distribution of apatite inclusions. Plagioclase phenocrysts usually have higher An content than microlites within the same rock. Phenocrysts appear more weathered than the microlites in the Tecuamburro samples. This observation may be explained by the work done by Blum and Stillings (1995). These authors conclude that anorthite weathers, on average,  $10^4$  times faster than albite. Not only are the calcic phenocrysts more easily weathered, but apatite inclusions are commonly observed in phenocrysts like plagioclase. Therefore, the secondary REE-P-phase is more likely to develop in the calcic, weathered phenocrysts, and not the groundmass, where easily weathered apatite can be the source of elements to form the secondary REE-P phases.

Where the LREE are enriched relative to fresh lavas (e.g. Qtap 003), secondary LREE-P-phases are observed (figures 42d and 64), and where all REE are enriched, LREE-, MREE-, and HREE-P-phases are observed (figures 43b and 67).

Correspondingly, in samples where there is no REE enrichment, no REE-P-phases are observed. The REE-P phase is present in samples with a wide range of Ce anomalies, and samples with a large Ce anomaly ( $Ce/Ce^* < 0.6$ ) always contain REE-P-phases (figure 76).

Because many studies of secondary REE-phosphates focus on phosphorous-rich rocks like granites, it is interesting to note that in the Tecuamburro samples there is no correlation between bulk rock  $P_2O_5$  values and the presence of the secondary REE-P-phase (figure 76). There is also, as expected, no correlation with normative apatite (figure 76). Banfield and Eggleton (1989) observe that granites that develop secondary REE-P-phases have normative apatite values  $\geq 1\%$ , and that most rocks studied for phosphate-related REE enrichment have even higher values. However, normative apatite in the Tecuamburro core samples does not exceed 0.7% (figure 76). In fact, the samples that develop the REE-P-phases contain only between 0.2-0.5% normative apatite. This is important because it indicates that a high phosphorous content is not needed to support the early development of secondary REE-P-phases.

Secondary phosphates have been documented as the host for REE in weathered and hydrothermally altered rocks. Fodor et al. (1987) noted the presence of rhabdophane, a hydrous, REE-Y-bearing phosphate, in the groundmass of 1.03 Ma basalts from Kahoolawe Island. Because of the abundance of hydrothermal vents, and the presence of barite in the samples, they attribute the presence of this secondary mineral to hydrothermal alteration, not weathering.

Taunton et al. (2000) observed that secondary REE-phosphates such as rhabdophane and florencite had crystallized on the etched surfaces of primary apatite

grains in weathered and microbially altered granites. Secondary phosphates in the soil zone concentrated  $\text{Ce}^{4+}$  rather than the trivalent REE, because the  $\text{REE}^{3+}$ -bearing phase had been leached from that zone. However, secondary phosphates that host  $\text{REE}^{3+}$  were found lower in the profile, beneath the highly weathered soil.

Cotten et al. (1995) identified an Al-free, REE-Y-phosphate (rhabdophane) in 1.3-7.1 Ma French Polynesian, REE-enriched basalts. The  $\text{REE}^{3+}$  and Y are inferred to have been mobilized at a low pH by meteoric water, and transported a short distance, so as to not allow time for LREE-depletion and late, relative HREE enrichment. Negative Ce anomalies were observed in these samples as well.

### *Relative Element Mobility*

In almost all samples that are enriched in REE relative to fresh lavas, negative Ce anomalies ( $\text{Ce}/\text{Ce}^* < 1$ ) are present, and the magnitude of this anomaly varies from 0.22 to 0.97. It is widely recognized that Ce fractionates from the other REE during weathering of basalts (Cotten et al., 1995; Marsh, 1991; Ludden and Thompson, 1979), as well as granodiorite and granite (Gavshin et al., 1997; Nesbitt and Markovics, 1997; Banfield and Eggleton, 1989; Nesbitt, 1979) and meteorites (Croaz and Wadhwa, 2001; Mittlefehldt and Lindstrom, 1991) due to the change in oxidation state from  $\text{Ce}^{3+}$  to  $\text{Ce}^{4+}$ . Most large Ce anomalies at Tecuamburro are due to the immobility of  $\text{Ce}^{4+}$  relative to the mobility of the other  $\text{REE}^{3+}$  previously mentioned.

The two rinds of Qtapg 004 (recall figure 13) demonstrate both REE-enriched and REE-depleted behaviors, relative to both the core and fresh lavas (figure 43d). The unusual behavior of two rinds on one sample may support the idea that some rinds, like

that of Qtapg 002, depleted in REE relative to their core, represent more advanced stages of weathering than samples like Qtap 003, where the rinds are more enriched in REE than the cores (figure 42d). In Qtapg 004, the white and chalky rind, depleted in REE relative to the core, may have been more extensively weathered over the same period of time than the enriched, thinner, red rind (figure 43d). This is supported by petrography and SEM data that show that most primary phenocrysts in the white rind have been replaced by clay, while many primary phenocrysts in the red rind remain intact (figures 35, 36, 37 and 38). Also, REE-P-phases exist in the core and red rind of Qtapg 004, while in the white rind, the only P-phase found is devoid of REE (figure 71).

Support for this idea is found in the corestone sample (051200, sampled near Qtap 003), and is discussed in detail by Patino et al. (in review). The REE pattern of the center (core) of the corestone is relatively flat, with a pronounced negative Ce anomaly (figure 77). Compared to the REE pattern of fresh lavas from the region, it is obvious that the REE enrichment and negative Ce anomaly are the result of post-emplacement processes (figure 77). The rind of the center of the corestone is even more enriched in REE than the core, and the spheroidally exfoliated shells are depleted of REE. One shell has a positive Ce anomaly, most likely because the other REE are relatively depleted.

It can be concluded that the lava began with a composition similar to that reported in the literature for fresh samples, and as weathering progressed, and the corestone developed, the  $\text{REE}^{3+}$  were soluble (as observed by Harlavan and Erel, 2002; Aubert et al., 2001; Aiuppa et al., 2000; Gavshin et al., 1997; Cotten et al., 1995). It is thought that low pH enhances the mobility of  $\text{REE}^{3+}$ , and that high pH can induce their precipitation (Fodor et al., 1987; Duddy, 1980; Nesbitt, 1979). The low-pH weathering solution could

carry the easily mobilized  $\text{REE}^{3+}$  from the distal parts of the outcrop (the exfoliated shells in the case of the corestone) into less altered sections (rinds and cores). As the solution reacts with the unaltered rocks, elements like Ca and Na increase in solution, raising the pH, and subsequently precipitating the  $\text{REE}^{3+}$ . This would leave less altered sections of the rock enriched in  $\text{REE}^{3+}$ , and the exfoliated shells, or the overlying regolith, depleted. Since under oxidizing conditions  $\text{Ce}^{4+}$  was unable to move with the rest of the REE, a positive Ce anomaly develops in the shells or surrounding regolith (e.g. Taunton et al., 2000), and, because  $\text{REE}^{3+}$  are mobilized into the less-weathered, high-pH corestone, they can be enriched relative to the corestone's  $\text{Ce}^{4+}$  content, resulting in a negative Ce anomaly.

Other workers have presented similar models for the redistribution of the REE (Braun et al., 1998; Condie et al., 1995; Cotten et al., 1995; Nesbitt, 1979). The corestone model may explain the patterns observed in this study. Because the samples were taken from boulder fields, it is likely that the boulders sampled were once corestones themselves, from which their corresponding spheroidal shells and surrounding regolith material were separated by a debris flow or other form of mass wasting on the geomorphically active, rugged, and deeply incised slope of Tecumaburro volcano.

Relative mobility plots are an easy way to see which elements are moving within a given sample. In figure 78, the intermediate zone and rind of Qtapg 001, and the red and white rinds of Qtapg 004, are plotted normalized to their respective cores. The intermediate and rind sections of Qtapg 001, and the red rind of Qtapg 004 confirm that the heavy REE move later than (or not as much as) the light REE. In Qtapg 001, Rb, Sr, and Nb are progressively depleted, while Ba is enriched equally in the rind and

intermediate samples. In Qtapg 004, Ba, Pb, and the REE (except some HREE and Y) are enriched in the red rind, and then depleted in the more heavily weathered white rind. Yttrium, Yb, and Lu are depleted in the white rind. Strontium, U and, to a lesser extent Nb are progressively lost from the core, red, and white rind. In the red rind, phosphorous is slightly depleted while the LREE are enriched. In the white rind, both P and the REE are significantly depleted. This relationship is likely dominated by the weathering of apatite and the secondary REE-P phase. As apatite begins to weather, as in the red rind, Ca is rapidly lost and P is only slightly lost, while the REE are precipitated into a phosphate. Then, as weathering progresses and there are no longer alkalis left to keep the pH high, acidity increases and the secondary REE-phosphate is dissolved, releasing all of the remaining REE and P, as in the white rind.

In figure 79, the core and rind of Qtap 005, and the core, rind, and sub-rind weathering front (or 'egg') of Qtap 004 are plotted normalized to their respective cores. In Qtap 005, only Nb is depleted from the rind. In Qtap 004, the 'egg' weathering front and the rind have very similar patterns: Nb is highly depleted, followed by the REE, Sr, Rb, and K. This may indicate that, in some samples, Nb is mobilized earlier than the REE. The chemical similarity between the sub-rind weathering front of Qtap 004 and the exposed rind suggests that the two were formed by the same secondary process.

The rinds of Qas 004 and Qas 005a are plotted, normalized to their respective cores, in figure 80. In Qas 004, Rb and Ba are enriched in the rind with the L-MREE, while P, Sr and Nb are depleted. In 005a, Rb and, to a lesser extent Nb are depleted with the REE in the rind, and it is interesting to note that the HREE are slightly more depleted than the others.

Workers in Hawai'i (Kurtz et al., 2000) and Ireland (Hill et al., 2000) document the immobility of Nb in soil. Since it is obviously mobile in these incipiently weathered rocks from Guatemala, there must be some transitional stage of weathering during which it becomes immobile. Because there is no real change in Nb concentration from the red rind to the white rind in Qtapg 004 (figure 78), Nb may have reached the peak of its mobility at that stage of weathering.

Figure 81 is a general model for element mobility in the Tecuamburro samples. A low pH, maintained possibly by either the reaction of water with organic material to form carbonic acid, or the influx of hydrothermal waters, dominates in the regions where REE are mobile. A high pH dominates in regions such as the rind, where the REE-P-phases are precipitated. As mentioned previously, the high pH is maintained by the release of alkalis during the weathering of the rock.

The REE (except Ce), Y, and Ba move together from more to less weathered material. The parallel movement of these elements was also observed in the Kahoolaeian basalts by Fodor et al. (1987). Titanium and Zr are relatively immobile, but small amounts could possibly be mobilized by solution.  $Ce^{4+}$  remains in the regolith, unless conditions become reduced and it is mobilized. Iron is fairly immobile, but some can be lost in solution with the other major elements. Strontium, Rb, and most major elements are mobilized into the solution and taken out of the weathering profile, while Nb is mobilized into solution, then becomes immobile after possibly being re-precipitated. Some Mn and Pb may move from more to less weathered material, but most is lost to solution and removed.

### *Possible solution conditions*

Waters from the Tecuamburro volcanic complex were sampled by Janik et al. (1992) as part of an exploratory geothermal study. Laguna Ixpaco, a large hydrothermal lake situated south of unit Qas is characterized by high temperatures ( $\sim 80^{\circ}\text{C}$ ) and low pH ( $\sim 2.5$ ). Some steam-heated springs throughout the volcanic complex have temperatures of approximately  $55^{\circ}\text{C}$ , and pH ranging from 4 to 7 (Janik et al., 1992). Cold, meteoric waters that inflow to Ixpaco have a temperature of  $20^{\circ}\text{C}$ , and a pH of 7.29. Ranges in temperature and pH of the waters at Tecuamburro could easily explain the variety in weathering styles across the three units. The ranges may also explain the heterogeneity in the distribution of secondary minerals. Differences in hydrology, especially leaching conditions and leaching history, within a given flow may also explain the heterogeneous distribution of the secondary phases. Within different parts of a given lava flow, at least two solutions must be at work. The first has a low pH, and mobilizes trace elements out of that part of the profile. The second has a high pH, and enables the precipitation of trace elements into secondary phases. The increased secondary porosity in the more extensively weathered sections will allow the weathering solution to move rapidly through the sample, and a low pH is maintained due to the absence of alkalis. In less weathered sections, leaching may be slow, and alkalis released by phenocryst weathering raise the pH high enough for the secondary REE-phases to precipitate. The details of the pH and temperature conditions of the solutions are not well constrained.



## CONCLUSIONS

Compositional changes in volcanic rocks do occur at the early stages of weathering. While trace elements such as Th and Zr are less mobile, Nb, Rb, Sr, and particularly Ba, Y, and the REE are highly mobile. Barium, the REE<sup>3+</sup>, and Y are commonly enriched relative to fresh lavas in this slightly weathered system, precipitated into secondary minerals (Ba into barite or hollandite, and the REE and Y into secondary phosphate phases). The exact conditions for the precipitation of the REE-phases in the Tecuamburro complex are somewhat uncertain. However, it is clear that the secondary REE-phases are P-rich, and fractionate the LREE and HREE. Rubidium, Sr, and to a lesser degree Nb are generally lost from the system, either to be concentrated elsewhere in the regolith, or removed in solution.

While it is, at first glance, surprising that weathering rinds are enriched in the mobile trace elements, the corestone model proposed does provide a good first-order explanation. However, it is still unclear why some samples have precipitated the REE-P-phases, and others have not. For instance, there is no correlation between the age of the lava flows and the presence of the secondary REE-phases. It is likely that regional differences in water temperature, pH, and leaching conditions over time have created variations in secondary product development.

Continued work will focus on determining the stoichiometry of the primary REE host, as well as the secondary REE-phases within the lavas. Understanding how natural waters impact the composition of volcanic rocks will improve the accuracy of petrogenetic models for lavas from this and other arcs, in that workers will better be able

to recognize and discard samples whose chemistry has been altered by weathering. In the meantime, the ternary diagram in figure 82 is a good way to discern altered Central American lavas from fresh samples.

Cerium, Nd, and CaO were chosen for the following reasons: 1) Ce is immobile even in most highly weathered samples, 2) altered samples are commonly enriched in Nd, due to the precipitation of the secondary REE-P-phase, and 3) CaO is highly mobile, and is strongly depleted in altered samples due to the weathering of plagioclase and other phenocrysts. The shaded field represents fresh, unweathered samples from Central America. Samples that fall outside that field are considered altered, and should not be included in petrogenetic studies of the region. Note that Qtapg 001 falls within the 'fresh' field. This sample does contain REE-P-phases (figures 65 and 66), as well as barite (figure 60). However, it appears fresh on the ternary plot, and is not significantly enriched in REE (figure 43a). This may be a transitional sample, with unaltered chemistry, but secondary phases starting to form and concentrate trace elements.

Some samples, such as the core of Qtapg 001, contain the REE-P-phase and contain other mobile elements, but are not enriched enough in REE for it to fall outside the shaded "fresh" field (figure 82). If an igneous petrologist is only interested in the REE of a sample, the plot is excellent for separating out altered samples. However, it cannot necessarily separate out those samples in which only other elements (such as Nb or Rb) are mobile.

The goal of this study was, primarily, to identify geochemical signs of incipient alteration (e.g. element enrichment or depletion relative to fresh lavas) in volcanic samples that otherwise in the field, in hand sample and thin section, appear unaltered, and

to identify the secondary minerals responsible for the altered chemistries. While numerous workers have examined the effects of weathering and hydrothermal alteration in well-developed regoliths, few have looked at element mobility during the earliest stages of alteration. It is clear that the chemical alteration of volcanic rocks at these early stages is dramatic, and should be considered whenever sampling boulder fields or lava flows that have been exposed for some time. In tropical regions, such as Central America, boulder fields are often the only remaining sample sites for lavas older than 1 Ma. However, workers should be aware that these boulders could have been corestones that have been mobilized from the regolith by mass wasting, and therefore are likely to be far from fresh. This study has identified elements that are easily mobilized during incipient weathering, and the element enrichment and depletion trends presented should help igneous petrologists identify altered samples before they are used in petrogenetic studies.

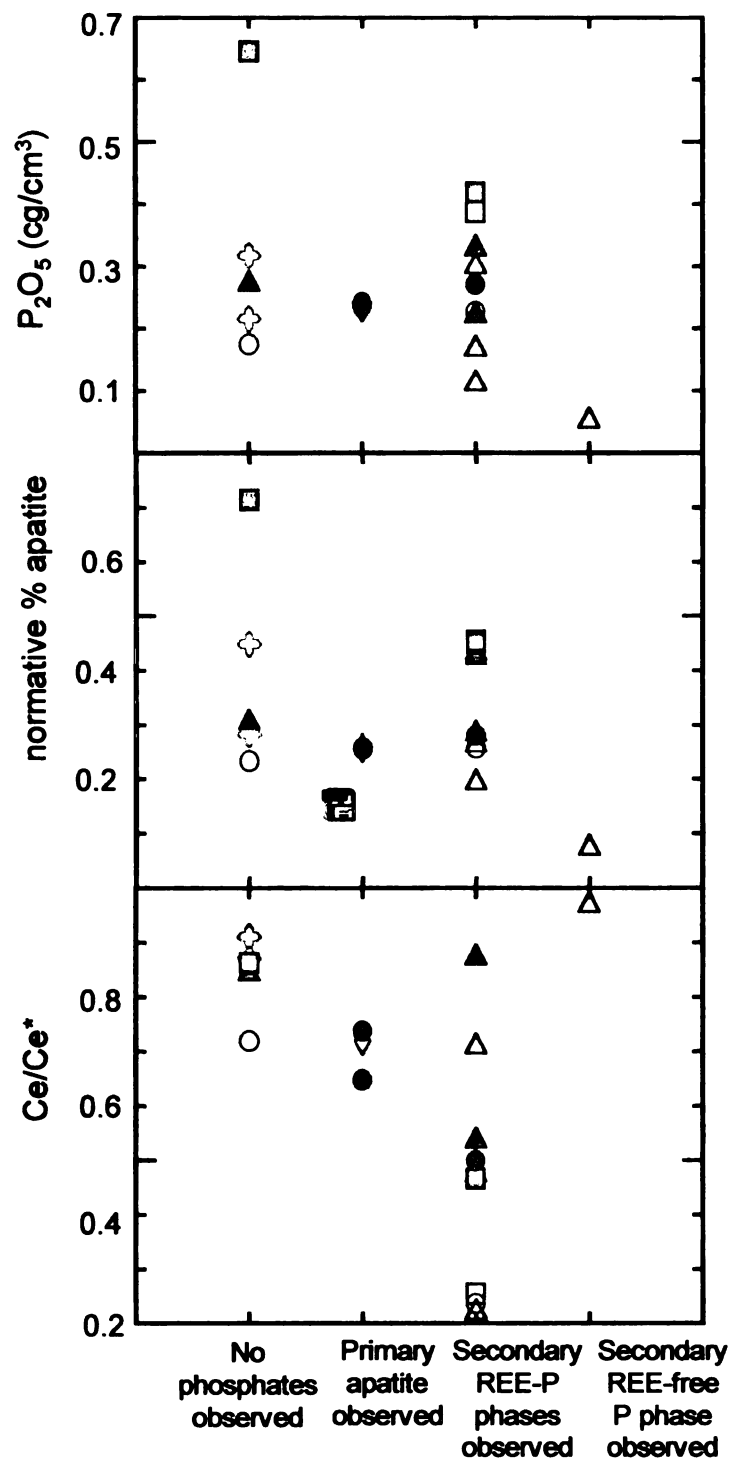


**Figure 76.** Plots of a) volumetric concentration of  $P_2O_5$ , b) normative % apatite, and c) Ce/Ce\* anomaly, all versus the presence (or absence) of primary and secondary phosphate phases. Note that there is no correlation between  $P_2O_5$  or apatite and the presence of the REE-P-phase, and that any sample with Ce/Ce\* < 0.6 contains the secondary REE-P-phases.

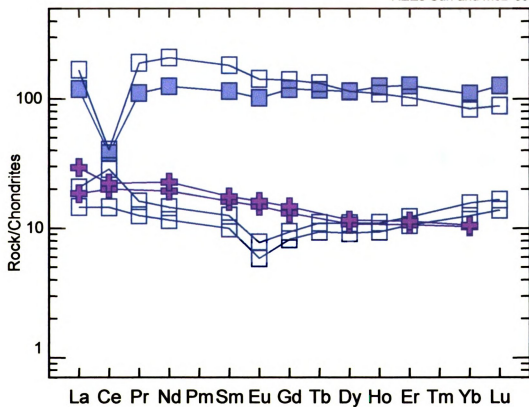


**Figure 77.** REE plot of the corestone 051200, from unit Qtap. ■ = core, □ = rind and exfoliated shells. + = values for fresh lavas of the volcanic complex. Note the enrichment of the core and rind of the corestone, and relative depletion of the highly weathered, spheroidally exfoliated shells (Patino et al., in review).

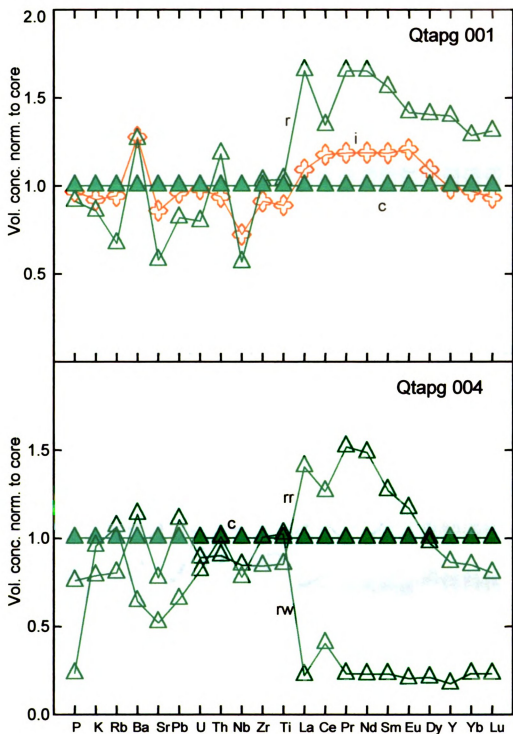


**Figure 78.** Element mobility plots for Qtapg 001 (core, intermediate, and rind) and Qtapg 004 (core, red rind, and white rind). All samples normalized to the core. Note that unlike previous trace element plots, the scale is linear, not log.

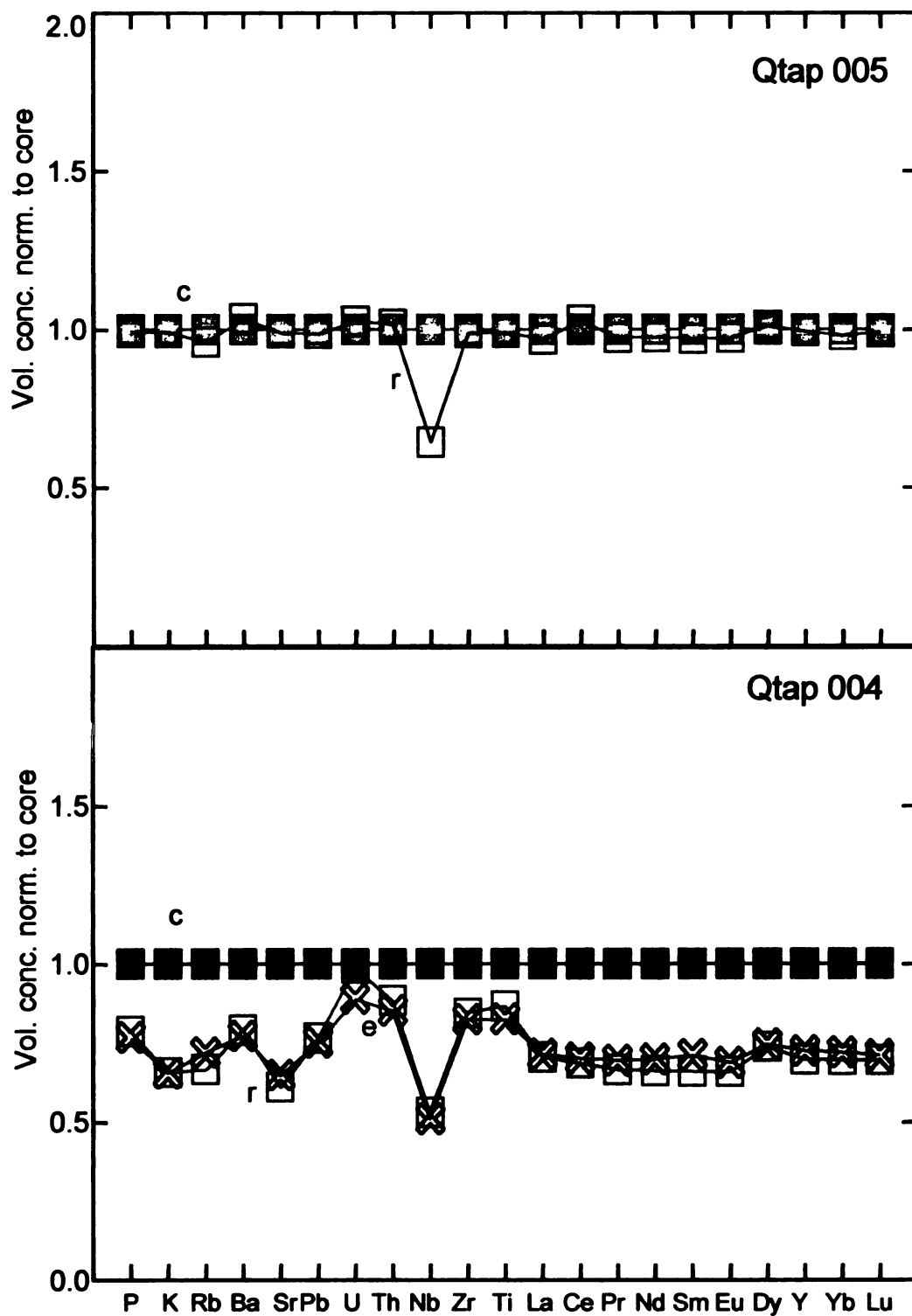


**Figure 79.** Element mobility plots for Qtap 005 (core and rind) and Qtap 004 (core, sub-rind weathering front ('egg'), and rind). All samples normalized to the core. Note that unlike previous trace element plots, the scale is linear, not log.

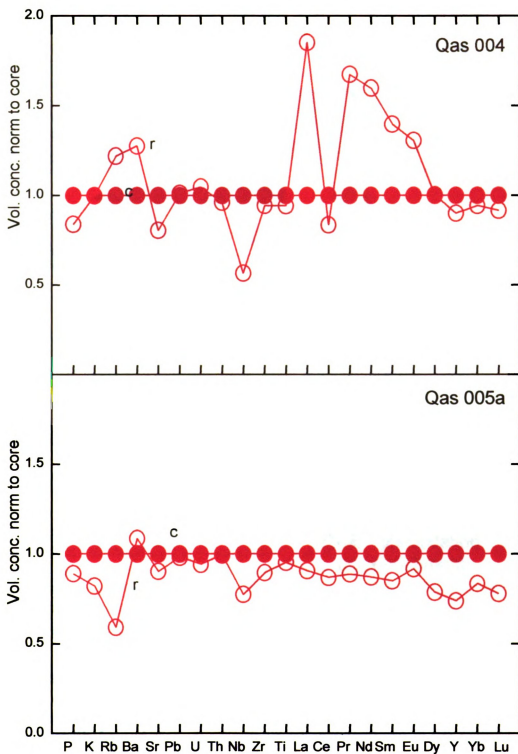



**Figure 80.** Element mobility plots for the cores and rinds of Qas 004 and 005. All samples normalized to the core. Note that unlike previous trace element plots, the scale is linear, not log.



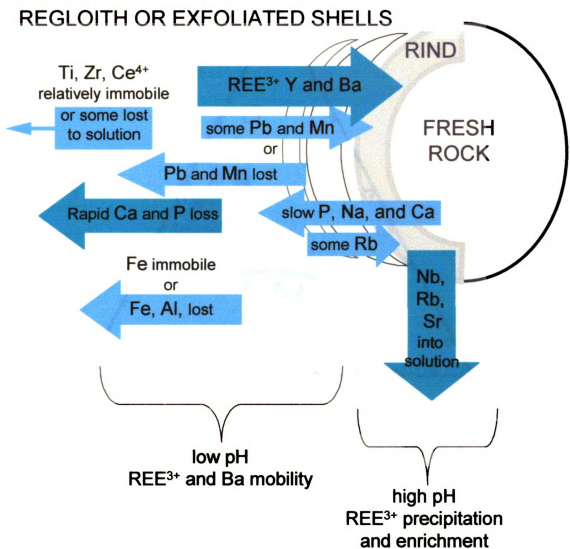


**Figure 81.** Element mobility model for Tecuamburro. In the zone of low pH (the regolith of exfoliated shells), most elements are mobilized into solution, while the rest are either immobile, or move into less weathered material (e.g.  $\text{REE}^{3+}$ , Y, Ba, and sometimes Rb, Pb, and Mn). In the zone of high pH (the rind and part of the core/fresh material), the REE, Y and Ba precipitate, and Na and Ca are only slowly lost.

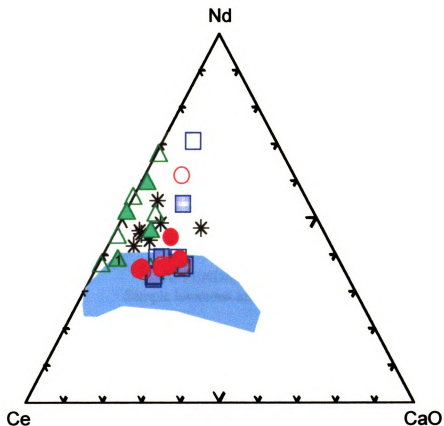


**Figure 82.** Ternary diagram that plots Ce, Nd, and CaO, in order to discern altered from fresh samples. The shaded field represents fresh Central American arc lavas. Samples that fall outside the shaded field are considered altered. Asterisks represent samples from Central America (other than those used in this study) that were sampled for petrogenetic studies, but were then found to be altered and excluded from the studies. Tecuamburro samples from this study are plotted as squares (Qtap), circles (Qas), and triangles (Qtapg). Filled symbols are cores, open symbols are rinds. Altered Tecuamburro samples in which the secondary REE-P-phases were found plot outside the fresh field (with the exception of Qtapg 001c, the transitional sample indicated as ) , and samples which are less altered fall within.

**APPENDIX A**  
**Sample locations and types**

UTM coordinates			sample type
<b>QTAP</b>	001	$773^{750}$ $1581^{100}$	angular block
	002	$773^{600}$ $1584^{400}$	outcrop
	003	$771^{450}$ $1579^{900}$	boulder
	004	$771^{900}$ $1579^{550}$	- ? -
	005	$773^{800}$ $1580^{450}$	outcrop
<b>QAS</b>	001	$775^{550}$ $1571^{800}$	boulder
	002	$775^{550}$ $1571^{800}$	boulder
	003	$777^{200}$ $1571^{650}$	boulder
	004	$777^{650}$ $1573^{200}$	rubbly outcrop
	005	$777^{850}$ $1574^{850}$	boulder
<b>QTAPG</b>	001	$783^{400}$ $1579^{450}$	boulder
	002	$783^{400}$ $1579^{750}$	boulder
	003	$783^{850}$ $1580^{200}$	boulder
	004	$784^{900}$ $1580^{500}$	block
	005	$782^{700}$ $1580^{750}$	boulder

**Appendix A.** Sample locations and types.

**APPENDIX B**  
**XRD sample preparation techniques**

## **APPENDIX B.**

### **X-ray diffraction sample preparation techniques**

Rock samples were cut into approximately 1 cm x 3 cm x 8 cm pieces using a diamond-blade saw, then hand-ground by mortar and pestle until approximately 6 grams of powder was produced. Equal amounts of powder were placed in two glass crystallizing dishes. The dishes were filled three-quarters with distilled water, and placed in a sonic bath for 8 minutes. Approximately 2 mL of liquid soap solution was added to the solution to prevent flocculation. The crystallizing dishes were then filled completely with distilled water, stirred, and left to settle for 2.5-3 hours, depending on ambient room temperature. After the appropriate settling time, the clay suspension solution was pipetted from both crystallizing dishes into a polypropylene bottle.

Four glass slides were then prepared for each sample: one raw, and three cation-saturated (Mg-saturated, Mg-saturated with glycerol solvation, and K-saturated). The raw sample was prepared by filtering 5 mL of clay solution through a 25 mm diameter, 0.45  $\mu\text{m}$  Millipore<sup>®</sup> filter vacuum system, to form clay cakes on the filters. The clay cake was rinsed with distilled water while still in the vacuum system, then removed and rolled onto a standard glass slide with a glass stirring rod and left to dry before the filter was removed, following Drever, 1973.

The cation exchange solutions were prepared with the following solutions:

- Magnesium exchange solution: 50.53 g  $\text{MgCl}_2 \cdot 6\text{H}_2\text{O}$  in 500 ml distilled water
- Magnesium exchange solution with glycerol: 10% glycerol by volume added to the above magnesium exchange solution

- Potassium exchange solution: 7.5 g KCl crystals in 1 L distilled water

Cation-saturated slides were prepared using the vacuum system method described above for the raw sample, except that after the 5 mL of clay suspension was processed through the filter, 5 mL of the exchange solution was filtered before rinsing. Postassium-saturated samples were prepared on heat resistant pyrex slides; once the K-saturated sample was analyzed in the XRD, it was then heated for 2 hours at 550°C and immediately rescanned after 10 minutes of cooling.

**APPENDIX C**  
**Bulk rock chemical analyses**



	qas0011c	qas0013i	qas0011r	qas002c	qas002r
SiO <sub>2</sub>	57.78	57.76	54.7	59.37	59.52
TiO <sub>2</sub>	0.74	0.74	0.73	0.73	0.75
Al <sub>2</sub> O <sub>3</sub>	17.6	17.42	17.47	16.69	17.22
Fe <sub>2</sub> O <sub>3</sub>	8.17	8.19	8.55	7.25	7.35
MnO	0.13	0.13	0.14	0.13	0.11
MgO	3.29	3.37	3.26	3.31	2.98
CaO	7.17	7.1	6.99	6.85	6.58
Na <sub>2</sub> O	3.16	3.19	3.17	3.15	3.02
K <sub>2</sub> O	1.33	1.34	1.33	1.5	1.47
P <sub>2</sub> O <sub>5</sub>	0.11	0.11	0.11	0.1	0.1
<b>Total</b>	<b>99.48</b>	<b>99.35</b>	<b>96.45</b>	<b>99.08</b>	<b>99.1</b>
Rb	28.3	26.6	32.9	26.8	24.7
Sr	372.3	364.5	374.7	352.3	341.6
Y	22.21	20.89	20.68	26.44	25.87
Zr	102.4	107.1	117	113	109.4
Nb	4.38	4.57	4.52	7.28	4.77
Ba	625.12	686.92	708.85	602.83	647.03
La	9.38	7.79	7.95	9.6	9.85
Ce	14.1	13.64	12.92	18.76	18.29
Pr	3.05	2.54	2.5	3.15	3.21
Nd	13.42	11.79	11.49	14.55	14.57
Sm	3.47	3.18	2.93	3.74	3.75
Eu	1.06	0.98	0.97	1.11	1.05
Gd	3.68	3.17	3.11	4.09	3.95
Tb	0.61	0.52	0.52	0.65	0.66
Dy	3.5	3.34	3.29	3.97	4.12
Ho	0.7	0.68	0.66	0.82	0.83
Er	2.16	1.99	2.01	2.46	2.5
Yb	2.32	2.22	2.11	2.7	2.71
Lu	0.33	0.31	0.3	0.4	0.39
Pb	3.51	3.24	3.8	7.64	8.8
Th	1.43	1.43	1.48	1.81	1.65
U	0.68	0.67	0.7	0.88	0.83
<b>blk.dens.</b>	<b>2.14</b>	<b>2.15</b>	<b>2.05</b>	<b>2.2</b>	<b>2.18</b>

**Appendix C. Concentrations of major element oxides (wt%) and trace elements (ppm), as well as bulk density values (g/cm<sup>3</sup>) for each sample. Major element, Zr, Rb, and Sr analyses obtained by XRF, and all other trace elements by LA-ICP-MS.**

	<b>qas0031c</b>	<b>qas0031r</b>	<b>qas004c</b>	<b>qas004r</b>
<b>SiO<sub>2</sub></b>	59.9	60.13	60.17	61.15
<b>TiO<sub>2</sub></b>	0.68	0.75	0.68	0.7
<b>Al<sub>2</sub>O<sub>3</sub></b>	17.19	17.27	16.81	17.08
<b>Fe<sub>2</sub>O<sub>3</sub></b>	7.28	8.02	7.4	7.77
<b>MnO</b>	0.13	0.14	0.13	0.13
<b>MgO</b>	2.85	2.76	2.97	2.64
<b>CaO</b>	6.67	5.87	6.18	5.02
<b>Na<sub>2</sub>O</b>	3.39	3.05	3.41	3.06
<b>K<sub>2</sub>O</b>	1.48	1.57	1.57	1.71
<b>P<sub>2</sub>O<sub>5</sub></b>	0.11	0.1	0.12	0.11
<b>Total</b>	<b>99.68</b>	<b>99.66</b>	<b>99.44</b>	<b>99.37</b>
<b>Rb</b>	26.4	31.4	27.2	36.2
<b>Sr</b>	367.8	332.5	356	312.7
<b>Y</b>	25.29	22.82	41.44	40.69
<b>Zr</b>	117.4	118.8	126.6	130.5
<b>Nb</b>	7.24	4.14	7.19	4.45
<b>Ba</b>	583.71	749.63	598.94	833.57
<b>La</b>	9.55	8.28	14.62	29.55
<b>Ce</b>	16.17	13.68	16.11	14.69
<b>Pr</b>	3	2.51	4.11	7.51
<b>Nd</b>	13.22	11.45	17.98	31.36
<b>Sm</b>	3.36	2.95	4.48	6.83
<b>Eu</b>	0.99	0.96	1.27	1.81
<b>Gd</b>	3.6	3.18	5.1	7.01
<b>Tb</b>	0.61	0.54	0.86	1.08
<b>Dy</b>	3.66	3.42	5.51	6.03
<b>Ho</b>	0.75	0.71	1.16	1.18
<b>Er</b>	2.39	2.14	3.5	3.32
<b>Yb</b>	2.5	2.29	3.37	3.47
<b>Lu</b>	0.37	0.34	0.48	0.48
<b>Pb</b>	4.52	4.77	4.4	4.86
<b>Th</b>	1.74	1.82	1.78	1.87
<b>U</b>	0.83	0.87	0.84	0.96
<b>blk.dens.</b>	<b>2.2</b>	<b>1.75</b>	<b>2.26</b>	<b>2.07</b>

**Appendix C continued.**

	<b>qas005ac</b>	<b>qas005ar</b>	<b>qas005cc</b>	<b>qas005cr</b>
<b>SiO<sub>2</sub></b>	58.18	57.15	58.31	57.82
<b>TiO<sub>2</sub></b>	0.95	0.98	0.9	0.93
<b>Al<sub>2</sub>O<sub>3</sub></b>	16.41	17.44	16.62	17.38
<b>Fe<sub>2</sub>O<sub>3</sub></b>	7.8	7.83	7.48	7.95
<b>MnO</b>	0.14	0.13	0.13	0.13
<b>MgO</b>	3.67	3.35	3.34	3.54
<b>CaO</b>	6.66	6.35	6.46	6.6
<b>Na<sub>2</sub>O</b>	3.21	3.3	3.24	3.11
<b>K<sub>2</sub>O</b>	1.99	1.77	2.06	1.74
<b>P<sub>2</sub>O<sub>5</sub></b>	0.27	0.26	0.25	0.26
<b>Total</b>	<b>99.28</b>	<b>98.56</b>	<b>98.79</b>	<b>99.46</b>
<b>Rb</b>	40.4	25.9	43.2	32.8
<b>Sr</b>	507.7	496.2	505.4	500.8
<b>Y</b>	27.22	21.75	24.79	22.38
<b>Zr</b>	162.1	157.1	153.7	154.2
<b>Nb</b>	8.55	7.17	8.87	6.92
<b>Ba</b>	723.49	850.57	735.87	788.15
<b>La</b>	15.29	15.02	15.26	14.28
<b>Ce</b>	28.81	27.09	29.15	26.68
<b>Pr</b>	4.59	4.41	4.62	4.24
<b>Nd</b>	20.24	19.09	19.91	18.29
<b>Sm</b>	4.59	4.22	4.48	4.25
<b>Eu</b>	1.36	1.35	1.35	1.32
<b>Gd</b>	4.56	3.93	4.36	4.2
<b>Tb</b>	0.71	0.62	0.67	0.67
<b>Dy</b>	4.31	3.67	3.97	3.78
<b>Ho</b>	0.86	0.73	0.78	0.74
<b>Er</b>	2.46	2.15	2.29	2.1
<b>Yb</b>	2.5	2.26	2.45	2.19
<b>Lu</b>	0.38	0.32	0.35	0.33
<b>Pb</b>	5.2	5.53	5.56	5.71
<b>Th</b>	2.21	2.38	2.43	2.49
<b>U</b>	0.94	0.96	1.01	0.95
<b>blk.dens.</b>	<b>2.23</b>	<b>2.06</b>	<b>2.17</b>	<b>1.97</b>

**Appendix C continued.**

	qtapg0012c	qtapg0011i	qtapg0011r	qtapg002c	qtapg002r
<b>SiO<sub>2</sub></b>	62.88	62.78	60.32	66.46	63.78
<b>TiO<sub>2</sub></b>	0.66	0.64	0.75	0.65	0.87
<b>Al<sub>2</sub>O<sub>3</sub></b>	16.86	17.09	18.01	15.57	17.26
<b>Fe<sub>2</sub>O<sub>3</sub></b>	5.61	5.46	8.02	4.4	6.32
<b>MnO</b>	0.11	0.12	0.15	0.15	0.1
<b>MgO</b>	1.77	1.72	1.82	0.58	0.53
<b>CaO</b>	4.69	4.28	2.72	2.59	0.98
<b>Na<sub>2</sub>O</b>	3.77	3.67	3	4.45	2.87
<b>K<sub>2</sub>O</b>	2.45	2.46	2.3	3.35	3.54
<b>P<sub>2</sub>O<sub>5</sub></b>	0.18	0.19	0.18	0.16	0.08
<b>Total</b>	98.98	98.41	97.27	98.36	96.33
<b>Rb</b>	60.5	62.2	44.5	91.4	91.2
<b>Sr</b>	355.7	333.1	224.8	262.2	89.7
<b>Y</b>	41.52	44.54	63.49	90.27	54.34
<b>Zr</b>	221.2	220	249.4	335.8	437.8
<b>Nb</b>	9.6	7.57	5.95	17.92	9.1
<b>Ba</b>	945.78	1316.96	1309.11	1362.96	727.03
<b>La</b>	27.29	32.52	49.48	60.03	52.79
<b>Ce</b>	53.64	68.76	78.95	45.72	23.03
<b>Pr</b>	8.7	11.26	15.76	17.36	12.5
<b>Nd</b>	35.92	46.52	65.03	69.22	47.85
<b>Sm</b>	8.41	10.86	14.38	15.63	9.72
<b>Eu</b>	2.16	2.84	3.35	3.59	2.05
<b>Gd</b>	7.88	9.6	12.21	14.14	8.58
<b>Tb</b>	1.23	1.45	1.89	2.19	1.4
<b>Dy</b>	7.09	8.43	10.92	13.2	8.73
<b>Ho</b>	1.35	1.53	2.03	2.59	1.69
<b>Er</b>	3.9	4.14	5.66	7.32	4.94
<b>Yb</b>	4.28	4.52	6.03	7.79	5.3
<b>Lu</b>	0.62	0.63	0.89	1.1	0.78
<b>Pb</b>	9.34	9.79	8.38	15.53	9.67
<b>Th</b>	4.55	4.65	5.9	6.77	8.44
<b>U</b>	2.48	2.65	2.17	4.54	3.55
<b>blk.dens.</b>	1.82	1.67	1.66	2	1.38

**Appendix C continued.**

	qtapg0031c	qtapg0031r	qtapg004c	qtapg004rr	qtapg004rw
SiO <sub>2</sub>	58.83	60.47	67.31	66.74	65.84
TiO <sub>2</sub>	0.65	0.72	0.64	0.66	0.71
Al <sub>2</sub> O <sub>3</sub>	16.74	16.46	15.71	15.38	16.82
Fe <sub>2</sub> O <sub>3</sub>	7.07	8.36	4.36	4.39	4.98
MnO	0.13	0.13	0.06	0.08	0.09
MgO	2.84	2.65	0.56	0.59	0.52
CaO	5.54	4.35	2.19	2.14	1.21
Na <sub>2</sub> O	3.42	2.85	4.32	4.3	3.15
K <sub>2</sub> O	1.88	2.12	3.43	3.27	3.55
P <sub>2</sub> O <sub>5</sub>	0.15	0.14	0.12	0.11	0.03
Total	97.25	98.25	98.7	97.66	96.9
Rb	47.8	54.5	97.3	94.7	112.4
Sr	402.4	307.8	257.5	241.3	145.2
Y	38.19	40.08	181.77	190.1	34.11
Zr	152.8	167.4	339.9	346.4	369.6
Nb	7.16	5.26	12.76	13.1	10.75
Ba	1023.47	873.44	1243.28	1713.57	862.87
La	19.76	19.29	96.8	164.87	23.13
Ce	25.76	20.7	114.64	175.69	50.08
Pr	5.92	5.64	30.44	56	7.59
Nd	26.53	25.37	120.78	217.23	29.65
Sm	6.51	6.08	27.72	42.67	6.86
Eu	1.56	1.45	6.89	9.76	1.51
Gd	6.62	6.4	25.54	34.28	5.8
Tb	1	0.95	4.03	5.12	0.94
Dy	5.96	5.66	25	29.51	5.65
Ho	1.18	1.11	4.99	5.42	1.12
Er	3.41	3.26	14.24	14.94	3.31
Yb	3.58	3.24	14.58	14.94	3.64
Lu	0.54	0.49	2.14	2.08	0.53
Pb	13.31	17.16	18.4	24.67	13.02
Th	3.52	3.91	6.9	7.53	7.54
U	1.48	1.54	4.86	5.23	4.3
blk.dens.	2.06	1.71	1.83	1.51	1.69

Appendix C continued.

	qtapg0051c	qtapg0051r	qtapg0052rck
SiO <sub>2</sub>	59.14	57.64	58.15
TiO <sub>2</sub>	0.68	0.72	0.71
Al <sub>2</sub> O <sub>3</sub>	17.14	17.7	17.55
Fe <sub>2</sub> O <sub>3</sub>	7.51	7.83	7.72
MnO	0.13	0.14	0.14
MgO	3.25	3.35	3.41
CaO	6.95	6.32	6.32
Na <sub>2</sub> O	3.05	2.95	2.9
K <sub>2</sub> O	1.86	1.78	1.81
P <sub>2</sub> O <sub>5</sub>	0.13	0.15	0.12
<b>Total</b>	<b>99.84</b>	<b>98.58</b>	<b>98.83</b>
Rb	37.3	37.8	38.8
Sr	399.9	371.4	364.7
Y	21.61	24.34	25.41
Zr	130.6	138.7	132.8
Nb	7.54	5.54	5.05
Ba	602.55	671.7	740.04
La	10.88	11.46	10.57
Ce	20.91	21.42	21.01
Pr	3.4	3.52	3.32
Nd	14.77	15.4	14.39
Sm	3.59	3.77	3.77
Eu	1.02	1.07	1.05
Gd	3.53	3.7	3.72
Tb	0.56	0.6	0.6
Dy	3.47	3.76	3.76
Ho	0.69	0.74	0.77
Er	2.05	2.22	2.31
Yb	2.06	2.36	2.46
Lu	0.33	0.37	0.37
Pb	5.16	5.32	5.42
Th	2.88	3.11	2.85
U	1.15	1.18	1.12
<b>blk.dens.</b>	<b>2.08</b>	<b>1.98</b>	<b>1.8</b>

Appendix C continued.

	qtap001bc	qtap001ar	qtap002ac	qtap002ar
SiO <sub>2</sub>	53.16	53.55	49.63	49.97
TiO <sub>2</sub>	0.82	0.84	1.2	1.23
Al <sub>2</sub> O <sub>3</sub>	18.56	18.56	16.99	16.81
Fe <sub>2</sub> O <sub>3</sub>	9.01	9.37	9.25	9.63
MnO	0.15	0.15	0.15	0.15
MgO	3.83	3.83	7.46	7.43
CaO	8.07	7.44	8.77	8.68
Na <sub>2</sub> O	3.25	3.13	3.4	3.24
K <sub>2</sub> O	0.89	0.93	0.96	0.96
P <sub>2</sub> O <sub>5</sub>	0.16	0.16	0.3	0.31
<b>Total</b>	<b>97.9</b>	<b>97.96</b>	<b>98.11</b>	<b>98.41</b>
Rb	17.3	18	13.3	10.4
Sr	513.4	473.9	512.5	499.8
Y	27.72	30.56	24.62	25.05
Zr	97	98.5	154.8	156.6
Nb	9.18	4.27	10.06	9.97
Ba	446.69	574.47	356.46	372.85
La	8.75	9.74	13.64	13.57
Ce	15.23	15.01	26.32	26.8
Pr	2.81	3.04	3.94	4.14
Nd	13.68	14.34	17.5	18.21
Sm	3.62	3.77	4.14	4.34
Eu	1.18	1.23	1.37	1.41
Gd	3.85	4.05	4.15	4.27
Tb	0.62	0.66	0.67	0.68
Dy	3.9	4.15	3.95	4.03
Ho	0.82	0.89	0.81	0.83
Er	2.4	2.49	2.26	2.33
Yb	2.48	2.48	2.29	2.42
Lu	0.38	0.39	0.34	0.36
Pb	2.86	2.98	3.12	3.35
Th	1.43	1.49	1.5	1.49
U	0.57	0.58	0.53	0.56
<b>blk.dens.</b>	<b>2.2</b>	<b>1.95</b>	<b>2.15</b>	<b>1.99</b>

Appendix C continued.

	qtap002bc	qtap002br	qtap0031c	qtap0031r
<b>SiO<sub>2</sub></b>	49.59	49.35	54.9	54.05
<b>TiO<sub>2</sub></b>	1.21	1.23	0.86	0.89
<b>Al<sub>2</sub>O<sub>3</sub></b>	17.07	16.99	18.03	18.18
<b>Fe<sub>2</sub>O<sub>3</sub></b>	9.31	9.58	9.09	9.23
<b>MnO</b>	0.15	0.15	0.17	0.18
<b>MgO</b>	7.43	7.71	3.22	3.32
<b>CaO</b>	8.89	8.58	7.52	7.06
<b>Na<sub>2</sub>O</b>	3.34	3.27	3.57	3.48
<b>K<sub>2</sub>O</b>	0.92	0.9	1	1.01
<b>P<sub>2</sub>O<sub>5</sub></b>	0.3	0.29	0.19	0.19
<b>Total</b>	98.21	98.05	98.55	97.59
<b>Rb</b>	10.8	10.1	19.9	21.2
<b>Sr</b>	515.8	502.6	474.6	453.7
<b>Y</b>	25.31	24.18	61.8	67.1
<b>Zr</b>	156.1	156	102	101
<b>Nb</b>	9.91	9.43	4.71	5.37
<b>Ba</b>	356.51	389.29	494.13	578.15
<b>La</b>	14.09	13.4	14.35	26.23
<b>Ce</b>	27.01	25.88	17.28	18.14
<b>Pr</b>	4.12	3.99	5.83	12.47
<b>Nd</b>	18.43	17.87	28.61	60.58
<b>Sm</b>	4.35	4.2	8.04	16.35
<b>Eu</b>	1.4	1.4	2.64	4.84
<b>Gd</b>	4.21	4.03	8.25	13.62
<b>Tb</b>	0.68	0.65	1.48	2.21
<b>Dy</b>	4.2	3.94	9.84	13.07
<b>Ho</b>	0.84	0.79	2.13	2.52
<b>Er</b>	2.3	2.21	6.28	6.83
<b>Yb</b>	2.36	2.18	7.06	7.63
<b>Lu</b>	0.36	0.35	1.11	1.13
<b>Pb</b>	3.2	4.13	3.14	3.13
<b>Th</b>	1.49	1.51	1.45	1.5
<b>U</b>	0.51	0.46	0.57	0.58
<b>blk.dens.</b>	1.96	1.91	2.2	2.04

Appendix C continued.



	qtap0041c	qtap0041r	qtap0041e	qtap0042e
SiO <sub>2</sub>	54.85	50.84	54.81	51.04
TiO <sub>2</sub>	0.74	0.86	0.75	0.84
Al <sub>2</sub> O <sub>3</sub>	18.82	22.17	19.01	21.68
Fe <sub>2</sub> O <sub>3</sub>	7.74	8.94	8	8.98
MnO	0.18	0.12	0.13	0.13
MgO	2.99	2.61	2.91	2.74
CaO	7.66	6.3	7.18	6.56
Na <sub>2</sub> O	3.26	2.93	3.17	2.95
K <sub>2</sub> O	1.51	1.33	1.48	1.36
P <sub>2</sub> O <sub>5</sub>	0.18	0.19	0.18	0.19
<b>Total</b>	<b>97.93</b>	<b>96.29</b>	<b>97.62</b>	<b>96.47</b>
Rb	39.4	35.2	40.1	39
Sr	484.8	396.6	463.3	432.2
Y	29.6	27.64	30.92	29.48
Zr	136.6	154.7	138.5	154.9
Nb	6.54	4.65	5.42	4.58
Ba	490.72	520.16	606.54	521.23
La	12.38	11.69	14.91	12.17
Ce	21.91	20.13	23.45	21.13
Pr	4.18	3.73	5.49	3.99
Nd	19	16.87	25.04	18.22
Sm	4.67	4.13	6.09	4.57
Eu	1.29	1.14	1.67	1.22
Gd	4.69	4.28	5.38	4.43
Tb	0.75	0.7	0.86	0.73
Dy	4.45	4.4	5.01	4.56
Ho	0.91	0.9	1	0.95
Er	2.59	2.57	2.81	2.69
Yb	2.8	2.61	2.88	2.77
Lu	0.44	0.41	0.45	0.43
Pb	4.26	4.37	4.43	4.41
Th	3.2	3.79	3.34	3.75
U	1.21	1.6	1.21	1.48
<b>blk.dens.</b>	<b>2.13</b>	<b>1.59</b>	<b>1.58</b>	<b>1.55</b>

**Appendix C continued.**

	<b>qtap005c</b>	<b>qtap005r</b>
<b>SiO<sub>2</sub></b>	<b>51.69</b>	<b>51.64</b>
<b>TiO<sub>2</sub></b>	<b>0.94</b>	<b>0.94</b>
<b>Al<sub>2</sub>O<sub>3</sub></b>	<b>18.55</b>	<b>18.62</b>
<b>Fe<sub>2</sub>O<sub>3</sub></b>	<b>9.6</b>	<b>9.68</b>
<b>MnO</b>	<b>0.14</b>	<b>0.15</b>
<b>MgO</b>	<b>4.35</b>	<b>4.29</b>
<b>CaO</b>	<b>8.54</b>	<b>8.4</b>
<b>Na<sub>2</sub>O</b>	<b>3.21</b>	<b>3.2</b>
<b>K<sub>2</sub>O</b>	<b>0.89</b>	<b>0.89</b>
<b>P<sub>2</sub>O<sub>5</sub></b>	<b>0.18</b>	<b>0.18</b>
<b>Total</b>	<b>98.09</b>	<b>97.99</b>
<b>Rb</b>	<b>19.4</b>	<b>18.8</b>
<b>Sr</b>	<b>485.2</b>	<b>484.3</b>
<b>Y</b>	<b>23.84</b>	<b>23.9</b>
<b>Zr</b>	<b>100.6</b>	<b>100.3</b>
<b>Nb</b>	<b>8.68</b>	<b>5.63</b>
<b>Ba</b>	<b>388.03</b>	<b>404.67</b>
<b>La</b>	<b>7.79</b>	<b>7.61</b>
<b>Ce</b>	<b>14.85</b>	<b>15.41</b>
<b>Pr</b>	<b>2.84</b>	<b>2.79</b>
<b>Nd</b>	<b>13.7</b>	<b>13.51</b>
<b>Sm</b>	<b>3.71</b>	<b>3.63</b>
<b>Eu</b>	<b>1.15</b>	<b>1.13</b>
<b>Gd</b>	<b>3.88</b>	<b>3.83</b>
<b>Tb</b>	<b>0.63</b>	<b>0.62</b>
<b>Dy</b>	<b>3.82</b>	<b>3.9</b>
<b>Ho</b>	<b>0.77</b>	<b>0.78</b>
<b>Er</b>	<b>2.18</b>	<b>2.11</b>
<b>Yb</b>	<b>2.12</b>	<b>2.1</b>
<b>Lu</b>	<b>0.33</b>	<b>0.33</b>
<b>Pb</b>	<b>2.32</b>	<b>2.31</b>
<b>Th</b>	<b>1.52</b>	<b>1.56</b>
<b>U</b>	<b>0.57</b>	<b>0.59</b>
<b>blk.dens.</b>	<b>2.15</b>	<b>2.13</b>

**Appendix C continued.**

**APPENDIX D**  
**Primary and secondary mineralogies**

	QTAPG									
	0012 c	0011 l	0011 r	002 r	004 c	004 rr	004 rw	005 rck		
optical microscope										
plagioclase	X	X	X	X	X	X	X	X		
clinopyroxene	X	X	X	X	X	X	X			
orthopyroxene	X	X	X		X			X		
hornblende	X	X	X	X	X	X		X		
opaques	X	X	X	X	X	X	X	X		
SEM										
apatite										
LREE-P-phases	X		X	X	X	X				
MREE-P-phases	X		X	X						
HREE-P-phases	X		X							
2ndry P-phase (no REE)							X			
K-feldspar			X			X				
barite		X	X							
hollandite		X				/	/	/		
kaolinite/halloysite										
XRD										
kaolinite/halloysite				X						
smectite					X	X	X			
gibbsite										

**Appendix D.** Primary and secondary mineralogy of Tecuamburro samples, as observed using optical microscopy, scanning electron microscopy, and x-ray diffraction. X = present, / = inferred.

	QTAP		O51200					
	003 c	003 r	004 c	004 r	8cc	8crs (l)	8crs (r)	8a (s)
optical microscope	X	X	X	X	X	X	X	
plagioclase								
clinopyroxene	X	X	X	X	X	X	X	X
orthopyroxene			X	X				
hornblende								
opaques	X	X	X	X	X	X	X	X
SEM								
apatite								
LREE-P-phases		X			X	X	X	
MREE-P-phases	X	X			X	X	X	
HREE-P-phases	X				X	X	X	
2ndry P-phase (no REE)								
K-feldspar								
barite								
hollandite								
kaolinite/halloysite					X		X	
XRD								
kaolinite/halloysite							X	X
smectite								
gibbsite				X				

Appendix D continued.

	QAS					
	001 c	003 c	003 l	003 r	004 c	004 r
<b>optical microscope</b>						
plagioclase	X	X	X	X	X	X
clinopyroxene	X	X	X	X	X	X
orthopyroxene	X				X	X
hornblende	X					
opaques	X	X	X	X	X	X
<b>SEM</b>						
apatite	X	X	X			
LREE-P-phases					X	X
MREE-P-phases						X
HREE-P-phases						
2ndry P-phase (no REE)						
K-feldspar					X	
barite				X		
hollandite						
kaolinite/halloysite						
<b>XRD</b>						
kaolinite/halloysite						X
smectite						
gibbsite						

Appendix D continued.

**APPENDIX E**  
**Instrumental precision**

		N	Mean	StDev	SE**	Given*
<b>XRF</b>	SiO <sub>2</sub>	5	52.054	0.273	0.122	52.41
	TiO <sub>2</sub>	5	1.282	0.0045	0.002	1.32
	Al <sub>2</sub> O <sub>3</sub>	5	14.504	0.036	0.016	14.53
	Fe <sub>2</sub> O <sub>3</sub>	5	8.998	0.0045	0.002	9.05
	MnO	5	0.14	0	0	0.15
	MgO	5	7.824	0.0688	0.0308	7.83
	CaO	5	9.288	0.0084	0.0037	9.31
	Na <sub>2</sub> O	5	2.714	0.023	0.0103	2.73
	K <sub>2</sub> O	5	1.382	0.0045	0.002	1.4
	P <sub>2</sub> O <sub>5</sub>	5	0.268	0.00447	0.002	0.26
	<b>Totals</b>	5	98.454	0.171	0.076	98.99
<b>ICP-MS</b>	Rb	5	40.42	1.789	0.8	39
	Sr	5	459.76	2.16	0.96	442
	Zr	5	139.06	0.99	0.44	144
	Ba	5	473.72	5.74	2.57	504
	La	5	38.242	0.484	0.216	37.6
	Ce	5	62.632	1.248	0.558	65.9
	Pr	5	7.286	0.252	0.113	7.3
	Nd	5	27.364	0.815	0.364	26.9
	Sm	5	5.472	0.1997	0.0893	5.07
	Eu	5	1.54	0.0652	0.0292	1.46
	Gd	5	5.082	0.1434	0.0641	4.67
	Tb	5	0.79	0.01732	0.00775	0.69
	Y	5	24.568	0.174	0.078	24
	Dy	5	4.246	0.094	0.042	3.99
	Ho	5	0.834	0.0261	0.0117	0.71
	Er	5	2.296	0.0702	0.0314	2.18
	Yb	5	2.274	0.0907	0.0406	2.1
	Lu	5	0.332	0.01304	0.00583	0.33
	V	5	186.88	3.49	1.56	205
	Nb	5	27.214	0.666	0.298	26.9
	Hf	5	3.728	0.1813	0.0811	6.65
	Ta	5	1.83	0.0812	0.0363	1.93
	Pb	5	5.852	0.1788	0.08	6.76
	Th	5	10.018	0.359	0.16	9.03
	U	5	1.642	0.0676	0.0302	1.67

\* Imai et al. (1995) Geostandards Newsletter, 19, 135-213

\*\* Standard error = standard deviation divided by the square root of the number of samples

**Appendix E.** Instrumental precision. JB-1a was treated as an unknown for XRF and ICP-MS analyses. (5 different samples were prepared as glass disks.)



**APPENDIX F**  
**Evaluation of instrumental precision**

	abs(c-r) qtapg 001	error as % of core	abs(c-r) qtapg 002	error as % of core	abs(c-r) qtapg 003	error as % of core
SiO <sub>2</sub>	2.56	0.0767	2.68	0.0811	1.64	0.0718
TiO <sub>2</sub>	0.09	0.0000	0.22	0.0000	0.07	0.0000
Al <sub>2</sub> O <sub>3</sub>	1.15	0.0027	1.69	0.0025	0.28	0.0027
Fe <sub>2</sub> O <sub>3</sub>	2.41	0.0001	1.92	0.0001	1.29	0.0001
MnO	0.04	0.0000	0.05	0.0000	0	0.0000
MgO	0.05	0.0005	0.05	0.0002	0.19	0.0009
CaO	1.97	0.0002	1.61	0.0001	1.19	0.0002
Na <sub>2</sub> O	0.77	0.0004	1.58	0.0005	0.57	0.0004
K <sub>2</sub> O	0.15	0.0000	0.19	0.0001	0.24	0.0000
P <sub>2</sub> O <sub>5</sub>	0	0.0000	0.08	0.0000	0.01	0.0000
total	1.71	0.0752	2.03	0.0748	1	0.0739
Rb	16	0.4840	0.2	0.7312	6.7	0.3824
Sr	130.9	3.4147	172.5	2.5171	94.6	3.8630
Zr	28.2	0.9733	102	1.4775	14.6	0.8723
Ba	363.33	24.3065	635.93	35.0281	150.03	26.3032
La	22.19	0.0589	7.24	0.1297	0.47	0.0427
Ce	25.31	0.2983	22.69	0.2551	5.06	0.1437
Pr	7.08	0.0098	4.86	0.0196	0.28	0.0067
Nd	29.11	0.1307	21.37	0.2520	1.16	0.0866
Sm	5.97	0.0075	5.91	0.0140	0.43	0.0058
Eu	1.19	0.0006	1.54	0.0010	0.11	0.0005
Gd	4.33	0.0051	5.56	0.0091	0.22	0.0042
Tb	0.66	0.0001	0.79	0.0002	0.05	0.0001
Y	21.97	0.0324	35.93	0.0704	1.89	0.0298
Dy	3.83	0.0030	4.47	0.0055	0.3	0.0025
Ho	0.68	0.0002	0.9	0.0003	0.07	0.0001
Er	1.76	0.0012	2.38	0.0023	0.15	0.0011
Yb	1.75	0.0017	2.49	0.0032	0.34	0.0015
Lu	0.27	0.0000	0.32	0.0001	0.05	0.0000
V	15.17	2.1431	6.19	0.3303	83.78	2.7946
Nb	3.65	0.0286	8.82	0.0534	1.9	0.0213
Hf	1.86	0.0038	2.5	0.0058	0.51	0.0033
Ta	2.62	0.0012	6.14	0.0026	1.71	0.0011
Pb	0.96	0.0075	5.86	0.0124	3.85	0.0106
Th	1.35	0.0073	1.67	0.0108	0.39	0.0056
U	0.31	0.0007	0.99	0.0014	0.06	0.0004

**Appendix F.** Evaluation of instrumental precision. For each sample, the left column is the absolute value of the concentration of the core minus the rind. The right column is the percent standard error (see Appendix E) of the analysis of the core sample.

	abs(c-r) qtapg 004r	error as % of core	abs(c-r) qtapg 004w	error as % of core	abs(c-r) qtapg 005	error as % of core
SiO <sub>2</sub>	0.57	0.0821	1.47	0.0821	1.5	0.0722
TiO <sub>2</sub>	0.02	0.0000	0.07	0.0000	0.04	0.0000
Al <sub>2</sub> O <sub>3</sub>	0.33	0.0025	1.11	0.0025	0.56	0.0027
Fe <sub>2</sub> O <sub>3</sub>	0.03	0.0001	0.62	0.0001	0.32	0.0002
MnO	0.02	0.0000	0.03	0.0000	0.01	0.0000
MgO	0.03	0.0002	0.04	0.0002	0.1	0.0010
CaO	0.05	0.0001	0.98	0.0001	0.63	0.0003
Na <sub>2</sub> O	0.02	0.0004	1.17	0.0004	0.1	0.0003
K <sub>2</sub> O	0.16	0.0001	0.12	0.0001	0.08	0.0000
P <sub>2</sub> O <sub>5</sub>	0.01	0.0000	0.09	0.0000	0.02	0.0000
total	1.04	0.0750	1.8	0.0750	1.26	0.0759
Rb	2.6	0.7784	15.1	0.7784	0.5	0.2884
Sr	16.2	2.4720	112.3	2.4720	28.5	3.8390
Zr	6.5	1.4956	29.7	1.4956	8.1	0.5746
Ba	470.29	31.9523	380.41	31.9523	69.15	15.4855
La	68.07	0.2091	73.67	0.2091	0.58	0.0235
Ce	61.05	0.6397	64.56	0.6397	0.51	0.1167
Pr	25.56	0.0344	22.85	0.0344	0.12	0.0038
Nd	96.45	0.4396	91.13	0.4396	0.63	0.0538
Sm	14.95	0.0248	20.86	0.0248	0.18	0.0032
Eu	2.87	0.0020	5.38	0.0020	0.05	0.0003
Gd	8.74	0.0164	19.74	0.0164	0.17	0.0023
Tb	1.09	0.0003	3.09	0.0003	0.04	0.0000
Y	8.33	0.1418	147.68	0.1418	2.73	0.0169
Dy	4.51	0.0105	19.35	0.0105	0.29	0.0015
Ho	0.43	0.0006	3.87	0.0006	0.05	0.0001
Er	0.7	0.0045	10.93	0.0045	0.17	0.0006
Yb	0.36	0.0059	10.94	0.0059	0.3	0.0008
Lu	0.06	0.0001	1.61	0.0001	0.04	0.0000
V	2.9	0.2874	2.21	0.2874	2.96	2.9384
Nb	0.34	0.0380	2.01	0.0380	2	0.0225
Hf	0.27	0.0061	0.59	0.0061	0.17	0.0028
Ta	0.21	0.0011	1.79	0.0011	2.07	0.0016
Pb	6.27	0.0147	5.38	0.0147	0.16	0.0041
Th	0.63	0.0110	0.64	0.0110	0.23	0.0046
U	0.37	0.0015	0.56	0.0015	0.03	0.0003

Appendix F continued.

	error as % of core	abs(c-r) qtap 002a	error as % of core	abs(c-r) qtap 002b	error as % of core	abs(c-r) qtap 003	error as % of core
SiO <sub>2</sub>	0.0649	0.34	0.0605	0.24	0.0605	0.85	0.0670
TiO <sub>2</sub>	0.0000	0.03	0.0000	0.02	0.0000	0.03	0.0000
Al <sub>2</sub> O <sub>3</sub>	0.0030	0.18	0.0027	0.08	0.0027	0.15	0.0029
Fe <sub>2</sub> O <sub>3</sub>	0.0002	0.38	0.0002	0.27	0.0002	0.14	0.0002
MnO	0.0000	0	0.0000	0	0.0000	0.01	0.0000
MgO	0.0012	0.03	0.0023	0.28	0.0023	0.1	0.0010
CaO	0.0003	0.09	0.0003	0.31	0.0003	0.46	0.0003
Na <sub>2</sub> O	0.0003	0.16	0.0004	0.07	0.0003	0.09	0.0004
K <sub>2</sub> O	0.0000	0	0.0000	0.02	0.0000	0.01	0.0000
P <sub>2</sub> O <sub>5</sub>	0.0000	0.01	0.0000	0.01	0.0000	0	0.0000
total	0.0744	0.3	0.0746	0.16	0.0746	0.96	0.0749
Rb	0.1384	2.9	0.1064	0.7	0.0864	1.3	0.1592
Sr	4.9286	12.7	4.9200	13.2	4.9517	20.9	4.5562
Zr	0.4268	1.8	0.6811	0.1	0.6868	1	0.4488
Ba	11.4799	16.39	9.1610	32.78	9.1623	84.02	12.6991
La	0.0189	0.07	0.0295	0.69	0.0304	11.88	0.0310
Ce	0.0850	0.48	0.1469	1.13	0.1507	0.86	0.0964
Pr	0.0032	0.2	0.0045	0.13	0.0047	6.64	0.0066
Nd	0.0498	0.71	0.0637	0.56	0.0671	31.97	0.1041
Sm	0.0032	0.2	0.0037	0.15	0.0039	8.31	0.0072
Eu	0.0003	0.04	0.0004	0	0.0004	2.2	0.0008
Gd	0.0025	0.12	0.0027	0.18	0.0027	5.37	0.0053
Tb	0.0000	0.01	0.0001	0.03	0.0001	0.73	0.0001
Y	0.0216	0.43	0.0192	1.13	0.0197	5.3	0.0482
Dy	0.0016	0.08	0.0017	0.26	0.0018	3.23	0.0041
Ho	0.0001	0.02	0.0001	0.05	0.0001	0.39	0.0002
Er	0.0008	0.07	0.0007	0.09	0.0007	0.55	0.0020
Yb	0.0010	0.13	0.0009	0.18	0.0010	0.57	0.0029
Lu	0.0000	0.02	0.0000	0.01	0.0000	0.02	0.0001
V	2.9384	1.36	3.0617	0.62	2.9901	9.37	2.7766
Nb	0.0274	0.09	0.0300	0.48	0.0295	0.66	0.0140
Hf	0.0018	0.01	0.0026	0.18	0.0026	0.14	0.0021
Ta	0.0025	0.11	0.0010	0.63	0.0010	0.72	0.0009
Pb	0.0023	0.23	0.0025	0.93	0.0026	0.01	0.0025
Th	0.0023	0.01	0.0024	0.02	0.0024	0.05	0.0023
U	0.0002	0.03	0.0002	0.05	0.0002	0.01	0.0002

Appendix F continued.

	error as % of core	abs(c-r) qtap 005	error as % of core	abs(c-r) qas 001	error as % of core	abs(c-r) qas 002
SiO <sub>2</sub>	0.0689	0.05	0.0631	3.08	0.0705	0.15
TiO <sub>2</sub>	0.0000	0	0.0000	0.01	0.0000	0.02
Al <sub>2</sub> O <sub>3</sub>	0.0030	0.07	0.0030	0.13	0.0028	0.53
Fe <sub>2</sub> O <sub>3</sub>	0.0002	0.08	0.0002	0.38	0.0002	0.1
MnO	0.0000	0.01	0.0000	0.01	0.0000	0.02
MgO	0.0009	0.06	0.0013	0.03	0.0010	0.33
CaO	0.0003	0.14	0.0003	0.18	0.0003	0.27
Na <sub>2</sub> O	0.0003	0.01	0.0003	0.01	0.0003	0.13
K <sub>2</sub> O	0.0000	0	0.0000	0	0.0000	0.03
P <sub>2</sub> O <sub>5</sub>	0.0000	0	0.0000	0	0.0000	0
total	0.0744	0.1	0.0745	3.03	0.0756	0.02
Rb	0.3152	0.6	0.1552	4.6	0.2284	2.1
Sr	4.6541	0.9	4.6579	2.4	3.5741	10.7
Zr	0.6010	0.3	0.4426	14.6	0.4506	3.6
Ba	12.6115	16.64	9.9724	83.73	16.0656	44.2
La	0.0267	0.18	0.0168	1.43	0.0203	0.25
Ce	0.1223	0.56	0.0829	1.18	0.0787	0.47
Pr	0.0047	0.05	0.0032	0.55	0.0034	0.06
Nd	0.0692	0.19	0.0499	1.93	0.0488	0.02
Sm	0.0042	0.08	0.0033	0.54	0.0031	0.01
Eu	0.0004	0.02	0.0003	0.09	0.0003	0.06
Gd	0.0030	0.05	0.0025	0.57	0.0024	0.14
Tb	0.0001	0.01	0.0000	0.09	0.0000	0.01
Y	0.0231	0.06	0.0186	1.53	0.0173	0.57
Dy	0.0019	0.08	0.0016	0.21	0.0015	0.15
Ho	0.0001	0.01	0.0001	0.04	0.0001	0.01
Er	0.0008	0.07	0.0007	0.15	0.0007	0.04
Yb	0.0011	0.02	0.0009	0.21	0.0009	0.01
Lu	0.0000	0	0.0000	0.03	0.0000	0.01
V	2.6297	5.99	3.4292	7.73	3.3035	1.29
Nb	0.0195	3.05	0.0259	0.14	0.0131	2.51
Hf	0.0027	0.02	0.0020	0.2	0.0022	0.1
Ta	0.0012	2.93	0.0023	0.05	0.0008	2.18
Pb	0.0034	0.01	0.0019	0.29	0.0028	1.16
Th	0.0051	0.04	0.0024	0.05	0.0023	0.16
U	0.0004	0.02	0.0002	0.02	0.0002	0.05

Appendix F continued.

	abs(c-r) gas 003	error as % of core	abs(c-r) gas 004	error as % of core	abs(c-r) gas 005a	error as % of core	abs(c-r) gas 005c	error as % of core
SiO <sub>2</sub>	0.23	0.0731	0.98	0.0734	1.03	0.0710	0.49	0.0711
TiO <sub>2</sub>	0.07	0.0000	0.02	0.0000	0.03	0.0000	0.03	0.0000
Al <sub>2</sub> O <sub>3</sub>	0.08	0.0028	0.27	0.0027	1.03	0.0026	0.76	0.0027
Fe <sub>2</sub> O <sub>3</sub>	0.74	0.0001	0.37	0.0001	0.03	0.0002	0.47	0.0001
MnO	0.01	0.0000	0	0.0000	0.01	0.0000	0	0.0000
MgO	0.09	0.0009	0.33	0.0009	0.32	0.0011	0.2	0.0010
CaO	0.8	0.0002	1.16	0.0002	0.31	0.0002	0.14	0.0002
Na <sub>2</sub> O	0.34	0.0003	0.35	0.0004	0.09	0.0003	0.13	0.0003
K <sub>2</sub> O	0.09	0.0000	0.14	0.0000	0.22	0.0000	0.32	0.0000
P <sub>2</sub> O <sub>5</sub>	0.01	0.0000	0.01	0.0000	0.01	0.0000	0.01	0.0000
total	0.02	0.0758	0.07	0.0756	0.72	0.0755	0.67	0.0751
Rb	5	0.2112	9	0.2176	14.5	0.3232	10.4	0.3456
Sr	35.3	3.5309	43.3	3.4176	11.5	4.8739	4.6	4.8518
Zr	1.4	0.5166	3.9	0.5570	5	0.7132	0.5	0.6763
Ba	165.92	15.0013	234.63	15.3928	127.08	18.5937	52.28	18.9119
La	1.27	0.0206	14.93	0.0316	0.27	0.0330	0.98	0.0330
Ce	2.49	0.0902	1.42	0.0899	1.72	0.1608	2.47	0.1627
Pr	0.49	0.0034	3.4	0.0046	0.18	0.0052	0.38	0.0052
Nd	1.77	0.0481	13.38	0.0654	1.15	0.0737	1.62	0.0725
Sm	0.41	0.0030	2.35	0.0040	0.37	0.0041	0.23	0.0040
Eu	0.03	0.0003	0.54	0.0004	0.01	0.0004	0.03	0.0004
Gd	0.42	0.0023	1.91	0.0033	0.63	0.0029	0.16	0.0028
Tb	0.07	0.0000	0.22	0.0001	0.09	0.0001	0	0.0001
Y	2.47	0.0197	0.75	0.0323	5.47	0.0212	2.41	0.0193
Dy	0.24	0.0015	0.52	0.0023	0.64	0.0018	0.19	0.0017
Ho	0.04	0.0001	0.02	0.0001	0.13	0.0001	0.04	0.0001
Er	0.25	0.0008	0.18	0.0011	0.31	0.0008	0.19	0.0007
Yb	0.21	0.0010	0.1	0.0014	0.24	0.0010	0.26	0.0010
Lu	0.03	0.0000	0	0.0000	0.06	0.0000	0.02	0.0000
V	19.63	2.8986	8.4	2.7532	2.15	2.3659	7.12	2.2225
Nb	3.1	0.0216	2.74	0.0214	1.38	0.0255	1.95	0.0264
Hf	0.29	0.0025	0.02	0.0029	0.01	0.0032	0.09	0.0032
Ta	2.68	0.0015	2.62	0.0015	1.55	0.0010	1.94	0.0012
Pb	0.25	0.0036	0.46	0.0035	0.33	0.0042	0.15	0.0044
Th	0.08	0.0028	0.09	0.0028	0.17	0.0035	0.06	0.0039
U	0.04	0.0003	0.12	0.0003	0.02	0.0003	0.06	0.0003

Appendix F continued.

## REFERENCES

## REFERENCES

- Aiuppa A., Allard, P., D'Alessandro, W.D., Michel, A., Parello, F., Treuil, M., and Valenza, M. (2000) Mobility and fluxes of major, minor and trace metals during basalt weathering and groundwater transport at Mt. Etna volcano (Sicily). *Geochimica et Cosmochimica Acta* 64(11), 1827-1841.
- Aubert D., Stille, P., and Probst, A. (2001) REE fractionation during granite weathering and removal by waters and suspended loads: Sr and Nd isotopic evidence. *Geochimica et Cosmochimica Acta* 65(3), 387-406.
- Banfield J., and Eggleton, R. (1989) Apatite replacement and rare earth mobilization, fractionation, and fixation during weathering. *Clays and Clay Minerals* 37(2), 113-127.
- Bateman, R.M. and Catt, J.A. (1985) Modification of heavy mineral assemblages in English coversands by acid pedochemical weathering. *Catena* 12, 1-21.
- Berner, R.A., Sjöberg, E.L., Velbel, M.A., and Krom, M.D. (1980) Dissolution of pyroxenes and amphiboles during weathering. *Science* 207 (4436), 1205-1206.
- Blum A. E., and Stillings, L.L. (1995) Feldspar dissolution kinetics. In *Chemical weathering rates of silicate minerals*, Vol. 31 (ed. A.F. White and S.L. Brantley), pp. 291-351. Mineralogical Society of America.
- Brantley S. L., and Chen, Y. (1995) Chemical weathering rates of pyroxenes and amphiboles. In *Chemical weathering rates of silicate minerals*, Vol. 31 (ed. A.F. White and S.L. Brantley), pp. 119-172. Mineralogical Society of America.
- Braun J. J., Viers, J., Dupre, B., Polve, M., Ndam, J., and Muller, J.P. (1998) Solid/liquid REE fractionation in the lateritic system of Goyoum, East Cameroon: the implication for the present day dynamics of the soil covers of the humid tropical regions. *Geochimica et Cosmochimica Acta* 62(2), 273-299.
- Brindley G. W., and Brown, G. (1980) Crystal Structures of Clay Minerals and their X-ray Identification. In *Mineralogical Society Monograph*, Vol. No. 5. Mineralogical Society.
- Cameron B. I. (1998) Melt generation and magma evolution in southeastern Guatemala. Dissertation, Northern Illinois University, 400 p.
- Carr M. J., Feigenson, M.D., and Bennett, E.A. (1990) Incompatible element and isotopic evidence for tectonic control of source mixing and melt extraction along the Central American Arc. *Contributions to Mineralogy and Petrology* 105, 369-380.



Colman S. M. (1982) Chemical weathering rates of basalts and andesites: Evidence from weathering rinds. USGS Professional Paper 1246.

Condie K. C., Dengate, J., and Cullers, R.L. (1995) Behavior of rare earth elements in a paleoweathering profile on granodiorite in the Front Range, Colorado, USA. *Geochimica et Cosmochimica Acta* 59, 279-294.

Consolmagno G. J., and Britt, D.T. (1998) The density and porosity of meteorites from the Vatican collection. *Meteoritics and Planetary Science* 33, 1231-1241.

Cotten J., Le Dez, A., Bau, M., Caroff, M., Maury, R.C., Dulski, P., Fourcade, S., Bohn, M., and Brousse, R. (1995) Origin of anomalous rare-earth element and yttrium enrichments in subaerially exposed basalts: Evidence from French Polynesia. *Chemical Geology* 119, 115-138.

Criss J. W. (1980) Fundamental parameters calculations on a laboratory microcomputer. *Advances in X-ray Analysis* 23, 93-97.

Crocket J. H. (2000) PGE in fresh basalt, hydrothermal alteration products, and volcanic incrustations of Kilauea volcano, Hawaii. *Geochimica et Cosmochimica Acta* 64(10), 1791-1807.

Crozaz G., and Wadhwa, M. (2001) The terrestrial alteration of Saharan Shergottites Dar al Gani 476 and 489: A case study of weathering in a hot desert environment. *Geochimica et Cosmochimica Acta* 65(6), 971-978.

Delvigne, J.E. (1998) Atlas of micromorphology of mineral alteration and weathering. Mineralogical Association of Canada, Ontario, 494 p.

Drever J. I. (1973) The preparation of oriented clay mineral specimens for X-ray diffraction analysis by a filter-membrane peel technique. *American Mineralogist* 58, 553-554.

Duddy I. R. (1980) Redistribution and fractionation of rare-earth and other elements in a weathering profile. *Chemical Geology* 30, 363-381.

Duffield W. A., Heiken, G.H., Wohletz, K.H., Maassen, L.W., Dengo, G., McKee, E.H., and Castaneda, O. (1992) Geology and geothermal potential of the Tecuamburro volcano area, Guatemala. *Geothermics* 21(4), 425-446.

Eggleton R. A., Foudoulis, C., and Varkevisser, D. (1987) Weathering of basalt: Changes in rock chemistry and mineralogy. *Clays and Clay Minerals* 35(3), 161-169.

Feigenson M. D., and Carr, M.J. (1993) The source of Central American lavas:

- inferences from geochemical inverse modeling. *Contributions to Mineralogy and Petrology* 113, 226-235.
- Fodor R. V., Bauer, G.R., Jacobs, R.S., and Bornhorst, T.J. (1987) Kahoolawe Island, Hawaii: Tholeiitic, alkalic, and unusual hydrothermal(?) "enrichment" characteristics. *Journal of Volcanology and Geothermal Research* 31, 171-176.
- Fodor R. V., Jacobs, R.S., and Bauer, G.R. (1994) Hollandite in Hawaiian basalt: a relocation site for weathering-mobilized elements. *Mineralogical Magazine* 58, 589-596.
- Gardner L. R. (1980) Mobilization of Al and Ti during weathering - isovolumetric geochemical evidence. *Chemical Geology* 30, 151-165.
- Gavshin V. M., Shcherbov, B.L., Bobrov, V.A., Solotchina, E.P., Sukhorukov, F.V., and Mel'gunov, M.S. (1997) Behavior of trace elements in the process of formation of a weathering profile on granites. *Russian Geology and Geophysics* 38(7), 1264-1276.
- Hanor J. S. (2000) Barite-celestite geochemistry and environments of formation. In *Sulfate Minerals*, Vol. 40 (ed. C. N. Alpers, J.L. Jambor, and D.K. Nordstrom), pp. 193-275. Mineralogical Society of America.
- Harlavan Y., and Erel, Y. (2002) The release of Pb and REE from granitoids by the dissolution of accessory phases. *Geochimica et Cosmochimica Acta* 66(5), 837-848.
- Hill I. G., Worden, R.H., and Meighan, I.G. (2000) Yttrium: The immobility-mobility transition during basaltic weathering. *Geology* 28(10), 923-926.
- Imai, N., Terashima, S., Itoh, S., and Ando, A. (1995) 1994 compilation of analytical data for minor and trace elements in seventeen GSI geochemical reference samples, "Igneous Rock Series." *Geostandards Newsletter* 19(2), 135-213.
- Janik C. J., Goff, F., Fahlquist, L., Adams, A.I., Roldán-M., A., Chipera, S.J., Trujillo, P.E., and Counce, D. (1992) Hydrogeochemical exploration of geothermal prospects in the Tecuamburro volcano region, Guatemala. *Geothermics* 21(4), 447-481.
- Jeong G. Y. (1998) Formation of vermicular kaolinite from halloysite aggregates in the weathering of plagioclase. *Clays and Clay Minerals* 46(3), 270-279.
- Koppers, A. and Nielsen, R (2002) Geochemical Earth Reference Model (GERM) Kd's database, at URL <http://earthref.org/databases/KDD/rockmineral.htm>, accessed July 9, 2002.
- Kurtz A. C., Derry, L.A., Chadwick, O.A., and Alfano, M. (2000) Refractory element mobility in volcanic soils. *Geology* 28(8), 683-686.
- Kuschel E., and Smith, I.E.M. (1992) Rare-earth mobility in young arc-type volcanic

- rocks from northern New Zealand. *Geochimica et Cosmochimica Acta* 56(11), 3951-3955.
- Ludden J. N., and Thompson, G. (1979) An evaluation of the behavior of the rare earth elements during weathering of sea-floor basalt. *Earth and Planetary Science Letters* 43, 85-92.
- Marsh J. S. (1991) REE fractionation and Ce anomalies in weathered Karoo dolerite. *Chemical Geology* 90, 189-194.
- Mitchell, T.D., Hulme, M., and New, M. (2002) Climate data for political areas. *Center for Climate Change, Area 34*:109-112.
- Mittlefehldt D. W., and Lindstrom, M.M. (1991) Generation of abnormal trace element abundances in Antarctic eucrites by weathering processes. *Geochimica et Cosmochimica Acta* 55, 77-87.
- Nagy K. L. (1995) Dissolution and precipitation kinetics of sheet silicates. In *Chemical weathering rates of silicate minerals*, Vol. 31 (ed. A.F. White and S.L. Brantley), pp. 173-233. Mineralogical Society of America.
- Nesbitt H. W. (1979) Mobility and fractionation of rare earth elements during weathering of a granodiorite. *Nature* 279, 206-210.
- Nesbitt H. W., and Markovics, G. (1997) Weathering of granodioritic crust, long-term storage of elements in weathering profiles, and petrogenesis of siliciclastic sediments. *Geochimica et Cosmochimica Acta* 61(8), 1653-1670.
- Othman D. B., White, W.M., and Patchett, J. (1989) The geochemistry of marine sediments, island arc magma genesis, and crust-mantle recycling. *Earth and Planetary Science Letters* 94, 1-21.
- Parker A. (1970) An index of weathering for silicate rocks. *Geological Magazine* 107, 501-504.
- Patino L. C., Carr, M.J., and Feigenson, M.D. (2000) Local and regional variations in Central American arc lavas controlled by variations in subducted sediment input. *Contributions to Mineralogy and Petrology* 138, 265-283.
- Patino L. C., Velbel, M.A., Price, J.R., and Wade, J.A. (in review) Trace element mobility during spheroidal weathering and corestone formation of basalts and andesites in Hawaii and Guatemala. *Chemical Geology*.
- Pearce J. A., and Peate, D.W. (1995) Tectonic implications of the composition of volcanic arc magmas. *Annual Review of Earth and Planetary Sciences* 23, 251-285.

Price R. C., Gray, C.M., Wilson, R.E., Frey, F.A., and Taylor, S.R. (1991) The effects of weathering on rare-earth element, Y and Ba abundances in Tertiary basalts from southeastern Australia. *Chemical Geology* 93, 245-265.

Rasmussen B. (1996) Early-diagenetic REE-phosphate minerals (florencite, gorceixite, crandallite, and xenotime) in marine sandstones: a major sink for oceanic phosphorous. *American Journal of Science* 296, 601-632.

Robertson I. D. M., and Eggleton, R.A. (1991) Weathering of granitic muscovite to kaolinite and halloysite and of plagioclase-derived kaolinite to halloysite. *Clays and Clay Minerals* 39(2), 113-126.

Sun S., and McDonough, W.F. (1989) Chemical and isotopic systematics of oceanic basalts: implications for mantle composition and processes. In *Magmatism in the Ocean Basins* (ed. A.D. Saunders and M.J. Norry), pp. 313-345. GSA Special Publications.

Taunton A. E., Welch, S.A., and Banfield, J.F. (2000) Microbial controls on phosphate and lanthanide distributions during granite weathering and soil formation. *Chemical Geology* 169, 371-382.

Tazaki K., Fyfe, W.S., and Dissanayake, C.B. (1987) Weathering of apatite under extreme conditions of leaching. *Chemical Geology* 60, 151-162.

Velbel M. A. (1980) Dissolution of pyroxenes and amphiboles during weathering. *Science* 207(4436), 1205-1206.

----- (1983) A dissolution-reprecipitation mechanism for the pseudomorphous replacement of plagioclase feldspar by clay minerals during weathering. In *Sciences Geologique, Memoires*, Vol. 71 (ed. D. Nahon and Y. Noack).

----- (1986) Influence of surface area, surface characteristics, and solution composition on feldspar weathering rates. In *ACS Symposium Series*, Vol. 323 (ed. J.A. Davis and K.F. Hayes). American Chemical Society.

----- (1993) Formation of protective surface layers during silicate-mineral weathering under well-leached, oxidizing conditions. *American Mineralogist* 78, 405-414.

Walker J. A., Carr, M.J., Patino, L.C., Johnson, C.M., Feigenson, M.D., and Ward, R.L. (1995) Abrupt change in magma generation processes across the Central American arc in southeastern Guatemala: flux-dominated melting near the base of the wedge to decompression melting near the top of the wedge. *Contributions to Mineralogy and Petrology* 120, 378-390.

Walter A.-V., Nahon, D., Flicoteaux, R., Girard, J.P., and Melfi, A. (1995) Behaviour of

major and trace elements and fractionation of REE under tropical weathering of a typical apatite-rich carbonatite from Brazil. *Earth and Planetary Science Letters* 136, 591-602.

White W. M., and Patchett, J. (1984) Hf-Nd-Sr isotopes and incompatible element abundances in island arcs: implications for magma origins and crust-mantle evolution. *Earth and Planetary Science Letters* 67, 167-185.

White A. F., Bullen, T.D., Schulz, M.S., Blum, A.E., Huntington, T.G., and Peters, N.E. (2001) Differential rates of feldspar weathering in granitic regoliths. *Geochimica et Cosmochimica Acta* 65(6), 847-869.

Woodhead J. D. (1989) Geochemistry of the Mariana arc (western Pacific): source composition and processes. *Chemical Geology* 76, 1-24.

MICHIGAN STATE UNIVERSITY LIBRARIES



3 1293 02372 0745